

UNIVERSITY OF CRETE
Department of Materials Science and Technology

*Investigation of Polymer Nanostructures in
Multiconstituent Hybrid Systems*

by

Eleni Pavlopoulou

A dissertation
submitted to the University of Crete
in fulfillment of
the requirements for the degree of
Doctor of Philosophy
In Materials Science and Technology

Heraklion 2009

*Στους γονείς μου, Σωτήρη και Θεοδώρα
στις αδερφές μου, Δέσποινα και Ιωάννα
και στον παππού μου, Ευθύμη*

Abstract

The fabrication of nanostructures and the investigation of their properties constitute a research area that has attracted the interest of the scientific community, because such nanohybrids are candidates for a number of novel applications. The study and understanding of the behavior of these new materials is very important in that it allows the optimization of their properties. In order to be able to understand and consequently control those characteristics, several material combinations are tested and multiconstituent systems are fabricated. As an example, soft materials with desirable mechanical properties, such as polymers, are appropriately mixed with inorganic moieties. Such mixtures may exhibit good electronic, optical or magnetic properties and generally the components are selected in such a way, that the hybrid materials have the desirable properties that are a unique combination of the properties of the parent materials.

In this research, three types of nanohybrid materials are investigated with small-angle X-ray scattering with respect to their structural properties: A) Block copolymers blended with a selective homopolymer at a low concentration; micelles with radii of approximately 10 nm are formed within the polymeric matrix and their characteristics are controlled by the copolymer macromolecular architecture and composition, the copolymer concentration and processing temperature, as well as by the homopolymer characteristics. B) Metal nanoparticles incorporated within pH-responsive polymeric matrices; suitably chosen micelles and microgels, with radii of 15 nm and 110 nm, respectively, are used as nanoreactors for the synthesis of Pt nanoparticles and the nanohybrids are characterized during all the synthetic steps and for various synthetic routes. C) Polymer – layered silicates nanocomposites; inorganic clay platelets are mixed with a semi-crystalline polymer, which intercalates within the galleries, and the effect of the clay presence on the crystallization kinetics and final properties are investigated.

Through the study of these multiconstituent systems, the ability of polymers to form or participate in the formation of a plethora of nanostructures is

demonstrated. Each one of the resulting nanohybrids is an attractive system for high-impact technological applications due to the ability to control and tailor the structure and sizes of the final products.

Περίληψη

Η δημιουργία νανοδομών έχει προσελκύσει το ενδιαφέρον της επιστημονικής κοινότητας, μιάς και τέτοια νανοϋβριδικά υλικά είναι υποψήφια για χρήση σε πολλές καινοτόμες εφαρμογές. Η μελέτη και κατανόηση της συμπεριφοράς των νεών αυτών υλικών είναι πολύ σημαντική, αφού επιτρέπει τη βελτιστοποίηση των ιδιοτήτων τους. Πολλά υλικά συνδυάζονται και συστήματα πολλαπλών συστατικών δημιουργούνται με απώτερο σκοπό την κατανόηση και τον έλεγχο των χαρακτηριστικών τους. Για παράδειγμα, χαλαρά υλικά με συγκεκριμένες μηχανικές ιδιότητες, όπως είναι τα πολυμερή, αναμειγνύονται με κατάλληλα ανόργανα στοιχεία και τα μείγματά τους παρουσιάζουν καλές ηλεκτρονικές, οπτικές, μαγνητικές, κ.α. ιδιότητες. Σε κάθε περίπτωση τα επιμέρους συστατικά επιλέγονται έτσι ώστε τα παραγόμενα υβρίδια να συγκεντρώνουν τις επιθυμητές ιδιότητες, οι οποίες είναι συνήθως συνδυασμός των ιδιοτήτων των αρχικών υλικών.

Στα πλαίσια της διατριβής αυτής, οι δομικές ιδιότητες τριών ειδών νανοϋβριδικών υλικών εξετάστηκαν με την τεχνική της σκέδασης ακτίνων X σε μικρές γωνίες: Α) Συσταδικά συμπολυμερή αναμείχθηκαν με ομοπολυμερές που είναι εκλεκτικός διαλύτης για τη μια συστάδα σε χαμηλές συγκεντρώσεις και μικκύλια με ακτίνα περίπου 10 nm σχηματίστηκαν μέσα στην πολυμερική μήτρα. Μελετήθηκαν τα χαρακτηριστικά τους σαν συνάρτηση της μακρομοριακής αρχιτεκτονικής και της σύστασης του συμπολυμερούς, της συγκέντρωσης του συμπολυμερούς και της θερμοκρασίας, καθώς επίσης των χαρακτηριστικών της μήτρας. Β) Μεταλλικά νανοσωματίδια ενσωματώθηκαν σε πολυμερικές μήτρες ευαίσθητες στο pH του διαλύματος. Κατάλληλα επιλεγμένα μικκύλια και μικροπηκτώματα (microgels), με ακτίνες 15 nm και 110 nm αντίστοιχα, χρησιμοποιήθηκαν ως νανο-αντιδραστήρες για τη σύνθεση νανοσωματιδίων πλατίνας και τα νανοϋβρίδια χαρακτηρίστηκαν σε κάθε στάδιο της σύνθεσης, ενώ παράλληλα διάφορες συνθετικές μέθοδοι ακολούθησαν. Γ) Τέλος παρασκευάστηκαν νανοςύνθετα υλικά πολυμερούς – φυλλόμορφων πυριτιδίων. Ο ανόργανος πηλός αναμείχθηκε με ημικρυσταλλικό πολυμερές που παρεμβάλλεται στις γαλαρίες του φυλλόμορφου πηλού και

μελετήθηκε η επίδραση της παρουσίας του πηλού στην κινητική της κρυστάλλωσης και τις τελικές ιδιότητες των νανοσύνθετων υλικών.

Η μέλετη των παραπάνω συστημάτων πολλαπλών συστατικών ανέδειξε την ικανότητα των πολυμερών να σχηματίζουν ή να συμμετέχουν στη δημιουργία πολλών νανοδομών. Καθένα από τα παραγόμενα νανοϋβρίδια είναι ένα ελκυστικό σύστημα για τεχνολογικές εφαρμογές υψηλού ενδιαφέροντος, χάρη στην ικανότητα ελέγχου και τροποποίησης της δομής των τελικών προϊόντων.

Acknowledgements / Ευχαριστίες

Reaching the end of this effort, there are quite a few people that have contributed and I would like to thank herein.

First of all, I would like to express my gratitude to my advisor, Prof. S. H. Anastasiadis for his trust and support throughout the last five years. I really appreciate the fact that he gave me all the freedom I wanted and needed in my research and encouraged me to take initiatives, which eventually made me self-confident from a scientific point of view. Working with him was always a constructive experience.

I feel indebted to all the chemists that synthesized and provided us with the polystyrene-polyisoprene copolymers and the polyisoprene homopolymers that were utilized in this work, Prof. N. Hadjichristidis and his co-workers, Dr. H. Iatrou, Dr. S. Pispas and M. Moshakou, as well as Dr. J. W. Mays, K. Hong and Dr. A. Avgeropoulos. Vassilis Katsamanis and Kostas Christodoulakis are acknowledged for the preparation of the nanoparticle-containing samples, as well as Prof. M. Vamvakaki, την οποία θα ήθελα να ευχαριστήσω όχι μόνο για την άψογη συνεργασία που είχαμε στα πλαίσια αυτού του project, αλλά και για την στήριξή της, όποτε και όπως χρειαζόταν.

I am really grateful to Dr. Wim Bras and Dr. Giuseppe Portale from the Dutch-Belgian Beamline at ESRF in Grenoble for all their help concerning the SAXS measurements that were conducted there, my training during my first visit in Grenoble, the allocation of beamtime, the technical support during experiments and all the useful discussions regarding data treatment and analysis. I would like to thank Giuseppe in particular for being the best collaborator I had up to now and for all the things I learned from him.

I owe a big thanks to all my fellow-students and friends that we were working side-by-side at IESL for the very nice environment that was always apparent in the lab. Με έμφαση στη Σαπφώ, το Μανώλη και το Νίκο, χωρίς όμως να ξεχνώ το Φάνη, τον Παναγιώτη, την Αντιγόνη, το Μάνο, τη Χριστίνα, τον Κώστα... Dr. Benoit Loppinet was also a very important person for me in the lab and I would like to thank him for all the discussions we had and all those he taught me about scattering and SAXS.

Τέλος, θα ήθελα να ευχαριστήσω όλους τους φίλους μου στο Ηράκλειο, και όχι μόνο, που με στήριξαν εκτός εργαστηρίου τα 5 τελευταία χρόνια. Η Δέσποινα, ο Οδυσσέας και η Ειρήνη, η Δήμητρα, οι Σοφίες είναι μερικοί από αυτούς. Και φυσικά την οικογένειά μου, τους γονείς μου και τις αδερφές μου, που αν και μακριά, ήταν πάντα οι σημαντικότεροι άνθρωποι στη ζωή μου. Γι'αυτό και τους αφιερώνω την εργασία αυτή, καθώς και στον παππού μου Ευθύμη Παπαϊωάννου που έφυγε στις 2 Μαρτίου.

Contents

Abstract	i
Περίληψη	iii
Acknowledgements / Ευχαριστίες	v
Contents	vii
1 Preface and Thesis Layout.....	1
2 Micellization in Block Copolymer / Homopolymer Blends	7
2.1 Introduction.....	7
2.2 Experimental Section	12
2.2.1 Materials.....	12
2.2.2 Sample Preparation	15
2.2.3 Small Angle X-ray Scattering.....	16
2.2.4 Data Analysis.....	18
2.3 The Effect of Macromolecular Architecture on the Micellization of Block Copolymers.....	21
2.3.1 Introduction	21
2.3.2 Micellization of I ₂ S Graft Copolymers	23
2.3.3 Micellization of S _n I _n Miktoarm Star Copolymers	33
2.3.4 Theoretical Considerations on the Micellization of A _n B _n Stars	40
2.3.5 Concluding Remarks.....	48
2.4 Concentration and Temperature Effects on the Micellization of Linear IS Copolymers	50
2.4.1 Introduction	50
2.4.2 Results and Discussion.....	53
2.4.3 Concluding Remarks.....	65
2.5 The Role of the Homopolymer Molecular Weight in the Micellization of Linear IS Copolymers.....	66
2.5.1 Introduction	66

2.5.2	Theoretical Models.....	69
2.5.3	Results and Discussion.....	74
2.5.4	Concluding Remarks.....	84
2.6	References and Notes	85
3	Impregnation of pH-Responsive Polymeric Matrices with Metal Nanoparticles	91
3.1	Introduction.....	91
3.2	Experimental Section	95
3.2.1	Materials.....	95
3.2.2	Sample Preparation	95
3.2.3	Metal Incorporation.....	96
3.2.4	Small Angle X-ray Scattering.....	97
3.3	Micelles Impregnated with Pt Nanoparticles.....	98
3.3.1	pH-Induced Micellization	98
3.3.2	Metallation of the Micelles using Method A.....	99
3.3.3	Metallation of the Micelles using Method B.....	103
3.3.4	Concluding Remarks.....	106
3.4	Microgel Particles Impregnated with Pt Nanoparticles.....	107
3.4.1	pH-Responsive Character of the Microgel Particles	107
3.4.2	Metallation of the Microgel Particles using Method A	109
3.4.3	Metallation of the Microgel Particles using Method B	115
3.4.4	Concluding Remarks.....	118
3.5	References and Notes	120
4	Crystallization Kinetics in Poly(ethylene oxide) / Layered Silicates Nanocomposites	123
4.1	Introduction.....	123
4.2	Experimental Section	127
4.2.1	Materials.....	127
4.2.2	Sample Preparation	128

4.2.3	Time-Resolved Small Angle X-ray Scattering.....	128
4.3	Results and Discussion	130
4.4	Concluding Remarks.....	138
4.5	References and Notes	139
5	Conclusions.....	141
	Suggestions for Future Work.....	146
	Appendix	149
	Small Angle X-ray Scattering.....	149

1 Preface and Thesis Layout

In recent years nanotechnology has evolved to the most competitive and more rapidly emerging area of modern science. Nanotechnology deals with the fabrication and exploitation of materials with structural features in the nanometer scale. Apart from the purely scientific interest in studying the physics that dictate the behavior of matter at nanoscale, nanotechnology bears new products with highly desirable properties, which have potentially numerous applications and, hence, are of special interest to industry. Soft matter inevitably constitutes a large subfield of nanotechnology, since the length-scales of the material involved and their superstructures, i.e., polymers, colloids, surfactants, etc., are in the nanometer range. Additionally, the plethora of nanostructures that result from the self-assembly of soft matter boost the interest of the research community, since these nanostructures comply with the industrial demand for low-cost and easily formulated products.

Self-assembly is a powerful synthetic approach to the fabrication of nanostructures with feature sizes smaller than achievable with state of the art lithography and with complexity approaching that of biological systems. The ability of soft matter systems to self-assemble on a hierarchy of length-scales is spectacular: molecules arrange themselves in supramolecular assemblies and these assemblies in turn pack in structures that may be highly ordered, even though the units that are being packed are non-crystalline and of dimensions considerably bigger than atomic scales. The most common examples of these self-assembled phases are found in solutions of amphiphilic molecules.

Polymers display the tendency to self-assemble, as well, if they are composed of two or more chemically different blocks covalently linked together. However, the large size of polymer molecules has important consequences for the thermodynamics of mixing. Even when the chemical units making up a pair of polymers are relatively similar, and the unfavorable energies of interaction between them small, the entropy of mixing is usually not large enough to promote mixing and the polymers will phase separate. If the two polymers are covalently

linked together forming block copolymers of various architectures, this constraint prevents them from phase separating on a macroscopic scale and the result is microphase separation, an ordered arrangement of domains of the two polymer types on mesoscopic length scales. The formation of micelles, which are thermodynamically stable aggregates of microscopic sizes, formed when an amphiphilic copolymer is added to a medium that is selective for one of the blocks, is actually a microphase separation phenomenon and constitutes one of the more simple nanostructures observed. Micellar systems are encountered not only in solutions in selective solvents, similarly to the case of small-molecule surfactants, but also in dispersions of copolymers within polymeric matrices; the behavior of the latter systems affects greatly the utilization of block copolymers in cases where their segregation to surfaces and interfaces is of special interest.

More complex nanostructures are formed in multiconstituent hybrid systems, such as innovative nanocomposite materials, based on optimized dispersion of zero-, one- and two dimensional inorganic nanoparticles within polymeric matrices. The development of such hybrids has attracted great attention lately. The inorganics can be nanoparticles, with all three dimensions in the nanoscale, one-dimensional carbon nanotubes and nanowires, with two dimensions in the nanometer range, and nanoclays or other moieties having one dimension in the nanoscale. There has already been significant progress in the synthesis, assembly and fabrication of nano-materials and their modification in order to affect their dispersion ability targeting potential applications in a wide variety of technologies. Ceramic nanoparticles, metal nanocrystals, semiconducting/magnetic materials, nanotubes based on carbon or equally on other inorganic materials and metallic or semiconducting nanowires are only a few of the nano-materials that have been developed. Moreover, mineral clays either belonging to the family of layered silicates or exhibiting elongated fibrous or hollow structures, extracted by mining and subsequent purification, have been utilized extensively.

All these nano-materials can be used as nanofillers for a range of polymers depending on the targeted application. In general, two different approaches have been utilized for their incorporation within polymeric nanostructures. One uses

preformed nanoparticles and takes advantage of their cooperative self-organization within the domains of e.g. ordered block copolymers. Addition of inorganic materials in a polymeric matrix is a very common approach to optimize properties, since it is expected that certain problems frequently encountered due to the large size (\sim a few microns) of the inorganic additives (like reduction of transparency or reduced toughness) would be overcome if the inorganic exists as a fine dispersion within the polymeric matrix. In these cases the final properties of the hybrid are determined mainly by the existence of many interfaces.

The second approach involves the in situ synthesis of the nanoparticles within the soft matter nanostructures. Functional polymeric materials, i.e. block copolymers, dendrimers and polymer microgels have attracted particular attention as nanoscopic reaction vessels for growing inorganic nanocrystals, whereas reverse micelles formed by anionic surfactants in organic media have been utilized as well. The use of (co)polymers allows potential control of the characteristics and properties of the nanoparticles by manipulating the polymer molecular structure, size and composition, whereas it permits utilization of both organic and aqueous dispersing media.

The decisive role of multiconstituent hybrid systems in contemporary research activity is adequately discussed above. Frequently the desirable properties of these nanocomposite materials are structure dependent and, therefore, the ability to characterize and tailor it, is of special interest. In this thesis three types of multiconstituent hybrid materials are investigated with respect to their structural properties:

The formation of block copolymer micelles in a homopolymer matrix that is selective for one of the copolymer's block is examined in **Chapter 2** with emphasis on the effects of macromolecular architecture and composition, copolymer concentration in the mixture, temperature and matrix homopolymer molecular weight. A series of miktoarm (polystyrene)_n(polyisoprene)_n, I_nS_n, star block copolymers, a series of graft (polyisoprene)₂(polystyrene), I₂S, graft copolymers as well as a (polystyrene)₂(polyisoprene), S₂I, graft are utilized to investigate the effect of macromolecular architecture on the micelle characteristics formed by the copolymers in a low molecular weight polyisoprene matrix. The

micellar characteristics are studied with small angle X-ray scattering (SAXS) as a function of the the number of arms, n , and of the copolymer composition, f_{ps} , for the miktoarm and the graft copolymers, respectively. Linear diblock copolymers, IS, with similar macromolecular characteristics (molecular weights and compositions) are examined as well and compared to their corresponding miktoarms. Additionally, a simple thermodynamic model is developed based on the methodology proposed by Leibler in order to describe theoretically the micellization of A_nB_n copolymers in a B homopolymer matrix; a quantitative agreement was obtained with the experimental data. Next, the characteristics of block copolymer/homopolymer blends were investigated as a function of concentration in the proximity of the critical micellization concentration (CMC) and as a function of temperature in the proximity of the critical micellization temperature (CMT). A symmetric linear IS diblock copolymer is utilized and a wide range of concentrations and temperatures were investigated. In the last section of this chapter, the homopolymer molecular weight is utilized as a control parameter for the tailoring of the micellar structure; the linear IS and the graft I₂S copolymers are blended with polyisoprene homopolymer of various molecular weights and the micellar characteristics are derived for the various matrices as a function of copolymer composition. The results are compared to the theoretical predictions of two models: that of Leibler and its extension for grafts, which assumes that the micellar corona is formed solely by the corona-forming blocks of the copolymers (dry corona) and the generalized model presented by Mayes-Olvera de la Cruz, which takes into account the penetration of homopolymer within the corona (wet corona). The latter was modified in the present work in order to describe the graft copolymer micelles.

A different perspective of the functionality of micelles is presented in **Chapter 3**. Two different classes of pH-responsive polymeric nanostructures have been utilized as nanoreactors for the growth of colloidal metal particles. The first class consists of the micellar cores of double hydrophilic block copolymers, whereas in the second case pH-sensitive microgels are used. The micelles are formed by double hydrophilic diblock copolymers PHEGMA-*b*-PDEA synthesized by group transfer polymerization. The hydrophobic PDEA block is

pH-responsive: at low pH it can be protonated and it becomes hydrophilic, leading to molecular solubility, whereas at higher pH micelles are formed with the hydrophobic PDEA blocks immobilized within the micellar cores. The PDEA microgel particles, synthesized by emulsion polymerization, exhibit reversible swelling properties in water as a function of the solution pH: at low pH, the microgel particles are swollen, while an increase of the pH leads to hydrophobic latex particles. Metal nanoparticles were formed within both the polymeric matrices by the incorporation of the appropriate metal precursor followed by metal reduction. Two synthetic routes have been utilized and are compared herein; in the first method the K_2PtCl_6 precursor was added to the PHEGMA-*b*-PDEA unimer dispersion or the hydrophilic swollen microgel particles at low pH followed by metal reduction and the pH was raised by the addition of base, while in the second H_2PtCl_6 was added to the micellar solution or the hydrophobic latex particles at high pH and then the metal salt was reduced in situ using $NaBH_4$. The structure of the hybrid systems was investigated by SAXS during the three steps of the metal nanoparticle synthesis: the original micelle and microgel dispersions in water, the metal-loaded polymer matrices and the metal nanoparticle-containing hybrids after reduction.

Finally, **Chapter 4** deals with another class of multiconstituent hybrids. An inorganic layered silicate material, natural montmorillonite, is mixed with a semi-crystalline polymer, PEO, and the effect of the clay presence on the crystallization kinetics and final properties is investigated in nanocomposites with clay concentration up to 10%; the data are compared to those for pure PEO. The crystallization kinetics was recorded by Time Resolved SAXS measurements. The samples were annealed above the melting temperature and then quenched at different isothermal crystallization temperatures, a few degrees above the non-isothermal crystallization temperature. Sequential SAXS patterns were acquired, following the isothermal crystallization. The data collected during a time resolved SAXS measurement enable the investigation of the lamellar formation and growth in the presence of the inorganic component.

It is noted that an introduction is provided at the beginning of each chapter, in order to familiarize the reader with the aim and the necessity of the

described research and provide the necessary scientific background. At the end of the thesis an overview of the salient points discussed throughout the text is given, as well as a paragraph devoted to suggestions on future work that could arise from the subjects treated herein.

2 Micellization in Block Copolymer / Homopolymer Blends

2.1 Introduction

It has been common practice to utilize suitably chosen block or graft copolymers added to immiscible polymer blends as compatibilizers for controlling the morphology (phase structure) and the interfacial adhesion between the phases in order to obtain an optimized product.^{1, 2} This is due to their interfacial activity, i.e., to their tendency to preferentially segregate to the interface between the two homopolymer phases;³⁻¹¹ this reduces the interfacial tension between the phase-separated homopolymers,¹²⁻¹⁸ aids droplet breakup and prevents coalescence,^{16, 19-22} increases the interfacial width between the phases^{10, 11, 23} and enhances interfacial adhesion.²⁴⁻²⁶

For a block or graft copolymer to be effective as an emulsifier, it is, thus, important that it is localized to the polymer-polymer interface,³⁻¹¹ with each block preferentially extending into its respective homopolymer phase.^{10, 11, 27-30} The efficiency of interfacial partitioning is predicted to depend on the molecular weights of the copolymer blocks relative to those of the homopolymers,^{9, 27, 31-33} on the macromolecular architecture/topology and composition of the copolymers,³⁴⁻⁴⁸ as well as on the interaction parameter balance between the homopolymers and the copolymer blocks.^{49, 50}

However, a critical issue that may severely influence the efficient utilization of a copolymeric additive as an emulsifier is the possible formation of copolymeric micelles within the homopolymer phases when the additive is mixed with one of the components.⁵⁰ The micelles will compete with the interfacial region for copolymer chains; the amount of copolymer at the interface or in micelles would depend on the relative reduction of the free energy with much of the pre-made copolymer often residing in micelles for high molecular weight additives. The effect of the existence of micelles on the interfacial partitioning of diblock copolymers at the polymer/polymer interface has received some attention

in the literature.^{9, 31-33, 51-55} A second issue relates to the possible trapping²⁸ of copolymer chains at the interface, which can lead to partial equilibrium situations.

Over the last few years the effects of the block copolymer molecular weight, composition and macromolecular architecture on the interfacial tension between two immiscible homopolymers has been studied by our group. When a series of compositionally symmetric diblock copolymer additives of different molecular weights (MW) was utilized, the maximum reduction of the interfacial tension, $\Delta\gamma = \gamma_0 - \gamma$, showed a non-monotonic dependence on the copolymer MW at constant copolymer concentration in the plateau region (at saturation): $\Delta\gamma$ increased by increasing the additive MW for low MWs, whereas it decreased by further increasing the copolymer MW.⁵³ This was understood within a simple model that considered the possibility of micelle formation as the additive MW increased leading to a three state equilibrium among copolymer chains adsorbed at the interface, chains homogeneously mixed with the bulk homopolymers and copolymer chains at micelles within the bulk phases. More recently, the effect of the macromolecular architecture and composition (f) of block copolymer additives on the interfacial tension between two immiscible homopolymers was studied utilizing A_2B and B_2A graft copolymers with constant MW and varying composition.⁵³ $\Delta\gamma$ at interfacial saturation was a non-monotonic function of the copolymer composition f exhibiting a minimum versus f , whereas it was lower than that for a symmetric diblock with the same total MW. The dependence on f was understood as a competition between the decreased affinity of the copolymer within the homopolymer phase when the size of the “other” constituent increases, which increases the driving force of the copolymer towards the interface, and the possibility of micellar formation. These ideas were supported by preliminary small-angle X-ray scattering measurements, which indicated the formation or absence of micelles. Moreover, $\Delta\gamma$ at saturation depended on the side of the interface the A_2B copolymer was added. This pointed to a local equilibrium that can only be attained in such systems: the copolymer reaching the interface from one homopolymer phase does not diffuse to the other phase. Even more, it was considered that the non-symmetric copolymer architecture could lead to

differences in the micellar formation when the copolymer is added to the different sides of the interface. Similar observations were made for non-symmetric copolymer segment lengths^{16, 17} or interactions.⁵⁶ It is, thus, essential to understand the micellization behavior of copolymers of varying molecular weights, composition and macromolecular architectures within homopolymer matrices.

The micellization of linear diblock copolymers added to a homopolymer matrix, which acts as a selective macromolecular solvent for the one of the blocks has been examined, both theoretically^{27, 57-60} and experimentally.⁶¹⁻⁷² Selb et al.⁶¹ studied dilute mixtures of polystyrene-block-polybutadiene (PS-*b*-PB) in a polybutadiene (PB) matrix using small angle neutron scattering (SANS) and found that the core radius increases with the MW of the polystyrene (PS) block, decreases with increasing the MW of the PB block, while it increases with increasing the MW of the PB homopolymer matrix. Rigby and Roe^{62, 63} studied the micellization characteristics of PS-*b*-PB in PB by small angle X-ray scattering (SAXS). They investigated the effect of temperature and copolymer concentration on the micellar structure and concluded that the radius of the core increases slightly with copolymer concentration, while it increases rapidly as the temperature increases due to the swelling of the core with homopolymer. Moreover, they studied the effect of copolymer composition (for constant total MW) on the micelle characteristics and the critical micelle concentration (CMC); the CMC decreased with decreasing temperature and as the fraction of PS in the copolymer increased, while the degree of swelling of the core by PB increased steadily with increasing temperature. Kinning, et al.⁶⁴⁻⁶⁶ studied the micelle formation of PS-*b*-PB (of varying MW and composition) in PS homopolymers by SAXS and transmission electron microscopy (TEM), which was enabled by the PS matrix, and they observed transitions in micelle geometry from spherical to cylindrical to lamellar structures depending on the MW's of the homopolymer and copolymer. The SAXS data for spherical micelles were modeled with the scattering predicted for polydisperse spheres interacting with each other (at higher concentrations) according to the Percus-Yevick hard sphere fluid approximation. Thus, they fully characterized the micelles by calculating structural parameters such as the core

radius (and its polydispersity), the corona thickness, the homopolymer concentration in the corona and in the core and the concentration of free (non-aggregated) copolymer chains. Also a transition from liquid-like order to an ordered lattice arrangement of spherical micelles was observed for high copolymer concentrations. More recently, SANS was utilized⁶⁷⁻⁶⁹ to investigate the micelle formation of PS-*b*-PB in PB where deuterium labeling allowed measurements in core or shell contrast. The study revealed that the concentration of the free copolymer chains was increasing even beyond the CMC whereas the corona showed almost constant density in contrast to block copolymer micelles in selective solvents. Torkelson and co-workers⁷⁰⁻⁷² utilized fluorescence measurements to study the CMC in copolymer/homopolymer blends. Labeled polystyrene-block-polyisoprene diblocks were originally used within polyisoprene matrices⁷⁰ whereas the intrinsic fluorescence of the styrene repeat units was recently utilized^{71, 72} to investigate the CMC in polystyrene-block-poly(methyl methacrylate) diblock and gradient copolymers mixed with non-fluorescent poly(methyl methacrylate) homopolymer. The estimated CMC depended strongly on the MWs of the core forming block of the copolymer and of the homopolymer whereas gradient copolymers exhibited significant higher CMCs than block copolymers of similar overall MW and composition; the latter was in agreement with theoretical predictions.⁴⁸

Leibler, Orland and Wheeler⁵⁷ were the first to propose a thermodynamic model for the formation of spherical micelles in block copolymer / homopolymer blends. They considered the total free energy of the system allowing for a fraction of the copolymer chains to remain free and for the penetration of homopolymer chains within the micellar corona, and predicted that the average number of free chains and the micellar characteristics are determined by a delicate balance between the internal energy of the micelles and the entropy of mixing of micelles, free copolymer chains and the homopolymer matrix. Whitmore and Noolandi²⁷ extended the theory of Leibler to take into account the localization of the copolymer joints to the interfacial region of the micelle, the possible penetration of homopolymer into the micellar core and the copolymer composition, and they derived the dependence of the micelle characteristics on those of the copolymer

and the homopolymer. Similar corrections have been applied by Roe,⁵⁸ who compared the theoretical predictions to the experimental results of Rigby and Roe^{62, 63} and found a good semi-quantitative agreement. The possibility of the formation of cylindrical micelles was examined by Mayes and Olvera de la Cruz,⁵⁹ who derived the free energy expressions for spherical and cylindrical micelles and discussed the conditions that favor the cylindrical over the spherical geometry. Finally, Monte Carlo simulations and self-consistent field theory were utilized recently to calculate the CMC and the size distribution and shape characteristics of diblock copolymer micelles formed within a homopolymer matrix.⁶⁰

In this chapter the micellization of block copolymers in a selective homopolymer matrix is investigated both experimentally, by Small Angle X-ray Scattering, SAXS, and theoretically, whenever this was feasible. The first section is dedicated to the study of the effect of the copolymers macromolecular architecture on the micellar characteristics; two systems are examined, a series of graft copolymers of various compositions and a series of miktoarm star copolymers with a varying functionality. In the second section the properties of the micelles and their environment are investigated with respect to the copolymers concentration and temperature. Finally, the third section deals with the penetration of the homopolymer chains within the corona of the micelles and the influence of the homopolymer molecular weight on the micellar structure. A special introduction is provided in the beginning of each section to establish the necessity of studying the respective subject and present the corresponding literature.

2.2 Experimental Section

2.2.1 Materials

A series of (polystyrene)_n(polyisoprene)_n, (PS)_n(PI)_n or S_nI_n, miktoarm star copolymers were synthesized by anionic polymerization using a high-vacuum technique in glass reactors provided with break-seals for the addition of reagents and constrictions for removal of products. The living polystyrene and polyisoprene blocks were synthesized first using sec-BuLi initiator. The chlorosilane chemistry approach was utilized to link the living PSLi and PILi blocks using specifically synthesized chlorosilane coupling agents. Details on the synthesis and characterization on these systems have been described earlier.¹⁶ These copolymers have *n* identical arms of polyisoprene blocks and *n* identical arms of polystyrene blocks connected at one central junction point. In that view, a polystyrene-block-polyisoprene, PS-*b*-PI or SI, diblock copolymer can be viewed as a special case of S_nI_n star block copolymers where *n* is equal to 1. The molecular characteristics of the samples obtained by membrane osmometry, size exclusion chromatography (SEC), low-angle laser light scattering and ¹H-NMR spectroscopy are shown in Table 2-1. Prof. N Hadjichristidis, Dr. H. Iatrou, and M. Moshakou are acknowledged for the synthesis and kind donation of the S_nI_n copolymers.

Table 2-1

Molecular Characteristics of the (Polyisoprene)_n(Polystyrene)_n Miktoarm Star Block Copolymers

Name	Structure	M_n^{b-PS} ^a	M_n^{b-PI} ^a	M_n^{star} ^a	M_w^{star} ^b	$\frac{M_w}{M_n}$ ^c	w_{PS} ^d	PS arms per junction
SI	PS-PI	19000	15000	36200	36300	1.05	0.55	1.0
S ₂ I ₂	(PS) ₂ (PI) ₂	19000	15000	64000	66000	1.04	0.56	2.1
S ₄ I ₄	(PS) ₄ (PI) ₄	19000	15000	121000	127500	1.04	0.54	3.6
S ₆ I ₆	(PS) ₆ (PI) ₆	19000	15000	181300	182600	1.05	0.56	5.7
S ₁₆ I ₁₆	(PS) ₁₆ (PI) ₁₆	19000	15000	e	533000	1.07	0.59	15.9

- a: number average molecular weight by membrane osmometry in toluene at 35°C;
- b: weight average molecular weight by LALLS in THF at 25°C;
- c: polydispersity index by size exclusion chromatography in THF at 25°C (UV detector);
- d: weight fraction by $^1\text{H-NMR}$;
- e: the molecular weight was too high to be measured by membrane osmometry.

A series of (polyisoprene) $_2$ (polystyrene), I $_2$ S, 3-miktoarm star copolymers (simple grafts) were synthesized by anionic polymerization using high-vacuum techniques in glass reactors provided with break-seals for the addition of reagents and constrictions for removal of products; the controlled chlorosilane chemistry approach was utilized. Details on the synthesis and characterization of these systems have been described earlier.⁷³⁻⁸⁰ The monomers (styrene, isoprene), the solvent (benzene) and the linking agent (methyltrichlorosilane) were purified to the standards required for high-vacuum techniques, following well-known procedures.^{74, 75, 80, 81} Living polystyrenyllithium (PSLi) and polyisoprenyllithium (PILi) precursors were synthesized in benzene using sec-butyllithium initiator. A ~3% w/v solution of PSLi in benzene was allowed to react with a large excess (SiCl/Li = 100) of methyltrichlorosilane (CH $_3$ SiCl $_3$) to produce PS-Si(CH $_3$)Cl $_2$, followed by the removal of the unreacted CH $_3$ SiCl $_3$ and benzene on the vacuum line. Next, an excess of PILi in benzene was added to a benzene solution of the macromolecular di-functional linking agent, PS-Si(CH $_3$)Cl $_2$, to obtain the CH $_3$ Si(PS)(PI) $_2$ 3-miktoarm star copolymers I $_2$ S. The excess PILi was deactivated with degassed methanol. The same procedure was utilized for the synthesis of the (polystyrene) $_2$ (polyisoprene), S $_2$ I, 3-miktoarm star copolymer where the first step involved the incorporation of polyisoprene arm (adding PILi) and the second that of the two polystyrene arms (adding excess of PSLi). The desired I $_2$ S or S $_2$ I graft was isolated from the reaction mixture by solvent/nonsolvent fractionation. The fractionated final products were rigorously characterized by size exclusion chromatography (SEC) with both RI and UV detectors, membrane osmometry, low-angle laser light scattering and $^1\text{H-NMR}$ in order to provide the molecular characteristics of the materials. The microstructure of the dienic sequences was analyzed by $^1\text{H-}$ and $^{13}\text{C-NMR}$ spectroscopy to be ca. 90% 1,4 and ca. 10% 3,4.

The author is grateful to Prof. N. Hadjichristidis, Dr. S. Pispas and Dr J. W. Mayes for the synthesis and kind donation of the I₂S and S₂I graft copolymers.

Three linear polyisoprene-block-polystyrene diblock copolymers, IS, were synthesized under high vacuum in a glass-sealed apparatus at room temperature using benzene as the solvent and *sec*-BuLi as the initiator with styrene being polymerized first. Dr. J. W. Mays and K. Hong are acknowledged for the synthesis and kind donation of these polymers.

The molecular characteristics of the IS, I₂S and S₂I copolymers are given in Table 2-2. All samples have approximately the same overall molecular weight (~100000g/mol) and varying compositions. Note that in all IS and I₂S copolymers the polystyrene sequence is perdeuterated (D8-styrene).

Table 2-2
Molecular Characteristics of the (Polyisoprene)₂(Polystyrene), (Polyisoprene)(Polystyrene) 2
Graft Copolymers and the Polyisoprene-b-Polystyrene Linear Copolymers

Species	M_w	$\frac{M_w}{M_n}$	w_{PS}^a	N^b	f_{PS}^c
I ₂ S-1	106000	1.04	0.91	1191	0.90
I ₂ S-2	90800	1.04	0.84	1031	0.82
I ₂ S-3	87400	1.04	0.67	1017	0.64
I ₂ S-4	92000	1.04	0.49	1098	0.46
I ₂ S-5	89800	1.04	0.35	1093	0.32
I ₂ S-7	91300	1.06	0.10	1149	0.09
S ₂ I-4	93000	1.06	0.48	1112	0.47
IS-3	116300	1.02	0.68	1354	0.65
IS-4	113700	1.05	0.52	1351	0.49
IS-5	99500	1.03	0.32	1213	0.29

a: polystyrene weight fraction by SEC-UV

b: number of copolymer segments based on average segmental volume

c: polyisoprene volume fraction

Polyisoprene homopolymers, PI, of 2000, 4000, 10000 and 20000 gr/mol molecular weight were anionically synthesized under Argon atmosphere and served as the matrices for the micelle formation. Dr. S. Pispas, Dr. A. Avgeropoulos, Dr J. W. Mays and K. Hong are acknowledged for the synthesis of the homopolymers and the kind donation. The characteristics of the PI homopolymers are shown in Table 2-3.

Table 2-3
Molecular Characteristics of the PI homopolymers used in the present study

Species	M_w	$\frac{M_w}{M_n}$	N^a
PI-1	2000	1.07	30
PI-2	4000	1.06	59
PI-3	10080	1.08	147
PI-4	20330	1.05	294

a: number of segments

2.2.2 Sample Preparation

The blends were prepared by dissolution of the copolymer in HPLC grade tetrahydrofuran (THF), a common good solvent for both polymers. Weighted amounts of the PI homopolymer matrix were then added to the solutions, so as to obtain the appropriate concentration of the copolymers in the homopolymer matrix (from 0.01 to 2wt%), and the mixtures were stirred for 24 hours. The remaining THF was removed by slow evaporation under vacuum. This sample preparation method was utilized to provide samples of well-dispersed copolymers into the viscous PI matrix. The samples were then placed inside appropriate glass capillary tubes of 2 mm diameter.

A note should be made regarding the possible influence of micellization kinetics that is considered to be very slow. The micelles are formed during solvent evaporation at a total polymer concentration where the effective interaction parameter in the solution, $\chi\phi_p$, becomes high enough, where ϕ_p is the total

polymer volume fraction in the solution and χ the interaction parameter. In a parallel investigation,⁸² the formation of micelles as a function of ϕ_p has been studied for copolymers of different molecular characteristics and architectures and for various copolymer concentrations. For example, for the 0.5 wt% S₂I₂/PI system, that is studied in the present work as well, micelles are formed when the total polymer concentration in the solution exceeds ~ 53 wt%. Therefore, in the range of copolymer concentrations investigated herein, the micelles are formed at not very high polymer concentrations. Under these conditions, the common solvent is present both within the core of the micelles and within the corona and the matrix. Thus, it would plasticize the polystyrene-rich core. Actually, if one uses the Fox-Flory formula, $1/T_g = w_1/T_{g_1} + (1-w_1)/T_{g_2}$, utilizing as T_{g_1} the glass transition of polystyrene ($T_{g_1}=398\text{K}$) and as T_{g_2} the melting temperature of THF ($T_{g_2}=165\text{K}$), one can estimate that only solutions with concentrations more than 75 wt% polymer will have a glass transition of 20°C or higher. Therefore, for the total polymer concentrations where micelles are formed in the present systems, it appears that the cores are still in the liquid state at 20°C and, thus, the micelles are formed close to equilibrium. Moreover, for the investigation of the effect of temperature on the micellization, measurements were performed at temperatures from 20 to 140°C for the present diblocks, where no changes in the aggregation number were observed except when the micelles reached the critical micellar dissolution temperature.

2.2.3 Small Angle X-ray Scattering

Most SAXS experiments were performed on the Dutch-Belgian Beamline (DUBBLE) at the European Synchrotron Radiation Facility (ESRF) station BM26B^{83, 84} in Grenoble, France. SAXS data were recorded on a two-dimensional position sensitive detector⁸⁵ using several combinations of energy of the X-ray beam and sample-to-detector distance in order to probe the optimum scattering vector range for each series of measurements. For instance, a wavelength of 1.55 Å and two different sample-to-detector distances, 3 m and 7.5 m, were used for

the measurements carried out for the investigation of the macromolecular architecture effect, which allowed a wide scattering vector range to be covered, $0.04 < q < 2 \text{ nm}^{-1}$; the magnitude of the scattering vector is $q = (4\pi/\lambda)\sin\theta$ with 2θ the scattering angle. The author is indebted to Dr. W. Bras and Dr. G. Portale for allocating beamtime and supporting the experiments.

The S_nI_n miktoarm copolymers were also studied at the Synchrotron Radiation Source (SRS) at Daresbury Laboratory, Warrington, UK, on station 16.1. A gas-filled area detector was used to collect data and a wavelength of 1.41 \AA was utilized. The sample-to-detector distance was 1.5 m and the scattering vector range explored was $0.2 < q < 2.5 \text{ nm}^{-1}$. Details concerning the station and the data collection electronics have been provided elsewhere.⁸⁶ Prof. A. Saiani is acknowledged for providing beamtime and the first guidance to SAXS measurements and Dr. A. J. Gleeson for his technical support during the experiment.

In both cases the two-dimensional images were radially averaged around the center of the primary beam, in order to obtain the isotropic SAXS intensity profiles. The scattering patterns from a specimen of wet collagen (rat tail tendon) and silver behenate were used for calibration of the q scale of the scattering curves. The data have been normalized to the intensity of the incident beam (in order to correct for primary beam intensity decay) and corrected for absorption, background scattering and copolymer concentration. Two ionization chambers placed before and after the sample, were utilized for the monitoring of the incident and the transmitted beams. Lupolen[®] and Eltex[®] were used as reference samples for the intensity calibration in absolute units (cm^{-1}). The scattering intensity from pure PI was subtracted from the total scattering intensity to account for the background correction due to the contribution of density fluctuations. All measurements were conducted at 25°C .

2.2.4 Data Analysis

For a mono-disperse collection of particles the scattering intensity can be written as

$$I(q) = N_p V^2 (\Delta\rho)^2 P(q) S(q) = \Phi V (\Delta\rho)^2 P(q) S(q) \quad (2.2.1)$$

where N_p is the number density of particles, V is the volume of the scattering particles, Φ is the volume fraction of particles, $\Delta\rho$ is the difference in the scattering length densities between the scattering particles and the matrix, $P(q)$ is the particle form factor and $S(q)$ is the structure factor which describes the spatial arrangement of the scattering particles. For dilute systems, like the ones in the present work, one can assume $S(q) = 1$.

The micelles in the present systems consist of a core formed mainly by the PS block of the copolymers and a surrounding corona formed by the PI blocks, either swollen or not, by the PI chains of the matrix. Thus, the electron density contrast is only between the PS core and the surrounding PI, independent if the PI is part of the matrix or of the copolymer. For all data presented we found that the assumption of spherical micelles was sufficient to analyze the data. The form factor for a homogeneous sphere of radius R was used:

$$P(q) = \frac{9(\sin qR - qR \cos qR)^2}{(qR)^6} \quad (2.2.2)$$

Inevitably, there is some distribution in the size of the micelles as well as a finite interface region between the core and the corona. The polydispersity in the micellar core radius can be accounted for by writing

$$I(q, r) = N_p (\Delta\rho)^2 \int_0^\infty (V(r))^2 P(q, r) f(r) dr \quad (2.2.3)$$

where $f(r)$ is the Gaussian distribution around the average core radius R

$$f(r) = \frac{1}{\sqrt{2\pi}\sigma} \exp\left(-\frac{(r-R)^2}{2\sigma^2}\right) \quad (2.2.4)$$

with σ the standard deviation of the distribution.

The calculated intensity was fitted to the experimental data by adjusting the two parameters R and σ and a scaling factor related to the product $N_p(\Delta\rho)^2$. The fitting was accomplished using a nonlinear least squares fitting procedure. The

error or uncertainty associated with the determination of each of the fitting parameters can be determined by an iterative fitting procedure. This consists of the variation of one parameter while keeping the others fixed and determining the necessary deviation to cause a notable divergence of the predicted scattering from the experimental data.

The scattered intensity can also be used to evaluate the invariant Q , which describes the mean square electron density fluctuations within the sample. The invariant was defined by Porod as

$$Q = \int_0^{\infty} I(q)q^2 dq \quad (2.2.5)$$

For an ideal two-phase system having sharp boundaries and constant densities within the phases, Q is equal to

$$Q = 2\pi^2\Phi(1-\Phi)(\Delta\rho)^2 \quad (2.2.6)$$

where Φ and $1-\Phi$ are the volume fractions of the two phases. The forward scattering intensity is given by

$$I_0 = \Phi V(\Delta\rho)^2 \quad (2.2.7)$$

Thus, the particle volume fraction Φ and the scattering volume V can be calculated for a given x-ray contrast, providing a second, independent way for the determination of the radius R .

The volume fraction ϕ of the total styrene units in the blend can be written as the sum of the styrene participating in micelles, ϕ_{mic} , and that dispersed in the matrix. Although there is no evidence on the form of the dispersed styrene units (i.e. free unimers, big aggregates, etc) it is initially speculated that the non-forming-micelles styrene is dissolved in the blend as unimers with volume fraction ϕ_{uni} and, thus,

$$\phi = \phi_{\text{mic}} + \phi_{\text{uni}} \quad (2.2.8)$$

Since the polystyrene fraction ϕ is known, ϕ_{uni} can be estimated, under the assumption that the cores of the micelles consist of pure polystyrene, which implies that ϕ_{mic} is equal to the particles volume fraction Φ . Due to the strong unfavorable interactions between PS and PI, it is anticipated that for the present systems the volume fraction of PS within the core should be very close to one.

This is consistent with the theoretical predictions by Leibler et al.⁵⁷ and Whitmore and Noolandi²⁷ and the experimental observations by Kinning et al.,⁶⁵ according to which the penetration of homopolymer within the core is negligible. Only Roe,⁶² based on SAXS data, estimates the degree of swelling of the core with homopolymer to be high, assuming that $\phi_{\text{uni}} \approx \phi_{\text{CMC}}$ and considering ϕ_{uni} to be negligible with respect to ϕ_{mic} ($\phi_{\text{uni}} \ll \phi_{\text{mic}}$). It is noted that the penetration of homopolymer in the core was checked theoretically by drawing the phase diagram of a polyisoprene homopolymer chain inside a polystyrene matrix, with molecular characteristics similar to the experimental ones. According to the phase diagram less than 5% swelling of the core with polyisoprene chains is allowed and thus the core can be safely considered to be formed only by polystyrene. Within this context, one can now calculate the volume V of the micellar core, the core volume fraction in the blends Φ , and the unimer volume fraction ϕ_{uni} . In the following discussion the volume fractions $\Phi = \phi_{\text{mic}}$ and ϕ_{uni} will be referring to the volume fractions of the copolymer chains participating in micelles and the free copolymer chains, respectively, keeping the same notation.

Finally, the aggregation number, e.g., the number of copolymer molecules participating in a micelle, can be calculated using the equation

$$Q_m = \frac{M_{\text{core}}}{M_{b\text{-PS}}} \quad (2.2.9)$$

where M_{core} is the mass of the core and $M_{b\text{-PS}}$ is the mass of each polystyrene block in the copolymer. For the S₂I graft and the S_nI_n miktoarm copolymers the number of PS arms in a copolymer molecule should be accounted as well. In order to calculate M_{core} we use the scattering volume V and the mass density of polystyrene above T_g .⁸⁷ Since $\Phi = N_p V$, the number density N_p of micelles in the solutions can be estimated as well.

2.3 The Effect of Macromolecular Architecture on the Micellization of Block Copolymers

2.3.1 Introduction

The importance of understanding the micellization behavior of copolymers of varying molecular weights, composition and macromolecular architectures within homopolymer matrices has been discussed above and the extended study of the micellization of linear diblock copolymers added to a homopolymer matrix, which acts as a selective macromolecular solvent for the one of the blocks, has been reviewed.

So far we have not found studies on the influence of the macromolecular architecture on the micellization in copolymer/homopolymer mixtures in the literature. However, there have been quite a few reports on the micellization of non-linear copolymers within low molecular weight selective solvents.^{73, 80, 88-92} Three-miktoarm (polystyrene)(polyisoprene)₂, PS(PI)₂, and (polystyrene)₂(polyisoprene), (PS)₂PI, star copolymers of similar molecular weights and compositions were studied⁸⁰ in *n*-decane, which is a selective solvent for the PI block, and the behavior was compared to that of the respective diblocks. Four-miktoarm star copolymers (polystyrene)(polyisoprene)₃, PS(PI)₃, of various molecular weight and compositions were investigated⁸⁸ in solvents selective for each polymer block. Moreover, twelve miktoarm star copolymers (polystyrene)₆/[poly(2-vinyl pyridine)]₆, (PS)₆(P2VP)₆ were studied⁸⁹ in toluene, which is a selective solvent for PS, as well as a sixteen miktoarm star copolymer (polyisoprene)₈(polystyrene)₈, (PS)₈(PI)₈, in *n*-decane.⁹⁰ Star block copolymers of the type (polyisoprene-*b*-polystyrene)₈, (PS-*b*-PI)₈, with PI inner blocks were studied in two solvents selective for PS.⁹¹ The micellar behavior for copolymers of even more complicated macromolecular architecture has been investigated as well. Examples include the behavior of model super-H-shaped block copolymers, (PI)₃(PS)(PI)₃, that were investigated in *n*-decane by SANS, light scattering and viscometry,⁹² as well as model graft copolymers of the H-type, (PS)₂(PI)(PS)₂, and

of the π -type, (PS,PI)PI(PI,PS), in solvents selective for the PI backbones or the PS branches, respectively.⁹³ Wherever possible, the results were compared with those obtained from the respective linear diblock copolymers with block lengths equal to the lengths of the corresponding arms, in order to isolate the effect of the architecture. It was found that the macromolecular architecture can influence noticeably the micellar shape, size and structure, depending on the relative crowding of arms in the core and the corona. A recent review article summarizes the micellization of block copolymers within low molecular weight selective solvents.⁹⁴

In this section the influence of the macromolecular architecture in the micellization characteristics of block copolymer / homopolymer blends is examined. A series of Y-shaped (polyisoprene)₂(polystyrene), I₂S, copolymers and a series of linear polyisoprene-polystyrene, IS, copolymers are added in a low molecular weight polyisoprene homopolymer matrix and the micellar characteristics are explored by SAXS, as a function of the polystyrene volume fraction in the copolymer, f_{PS} . All copolymers have the same overall molecular weight, while the copolymer concentration in the blends was kept constant at 2wt%. The results concerning the graft copolymers are compared to those obtained for the respective linear copolymer and for a (polystyrene)₂(polyisoprene) (S₂L) graft copolymer which is mirror-like to one of the I₂S grafts.

Thereinafter a series of $2n$ -miktoarm (polystyrene)_n(polyisoprene)_n star copolymers is added to a low molecular weight polyisoprene homopolymer matrix and the investigation of the micellar properties is carried out as a function of the functionality of the stars, n , where $n = 1, 2, 4, 6$ and 16 , and the copolymer concentration, which was varied from 0.05wt% to 2wt%. The results are compared with those obtained for the respective linear diblock copolymer and to theoretical predictions within a simple model that was developed herein, which follows the methodology of Leibler^{31, 32} and Semenov⁵² for diblock copolymers and its extensions for other geometries^{9, 53} or more complicated architectures.^{36, 37,}

2.3.2 Micellization of I₂S Graft Copolymers

The scattering profiles acquired for the 2wt% blends of the I₂S graft copolymers within the polyisoprene matrix for the various polystyrene compositions f_{PS} are presented in Figure 2.3.2.1a. The profile corresponding to the graft copolymer I₂S-7 with the lower polystyrene volume fraction is featureless, signifying that there are no micelles formed in that blend. The increasing intensity at the low wavevectors can be attributed to an increase in the electron density contrast due to the polystyrene blocks that are dispersed within the polyisoprene matrix. It is noted that, for the I₂S-7 copolymer, even a blend containing 4 wt% copolymer did not exhibit scattering features that would indicate the existence of micelles; thus, the CMC of the I₂S-7 is apparently higher than 4 wt%.

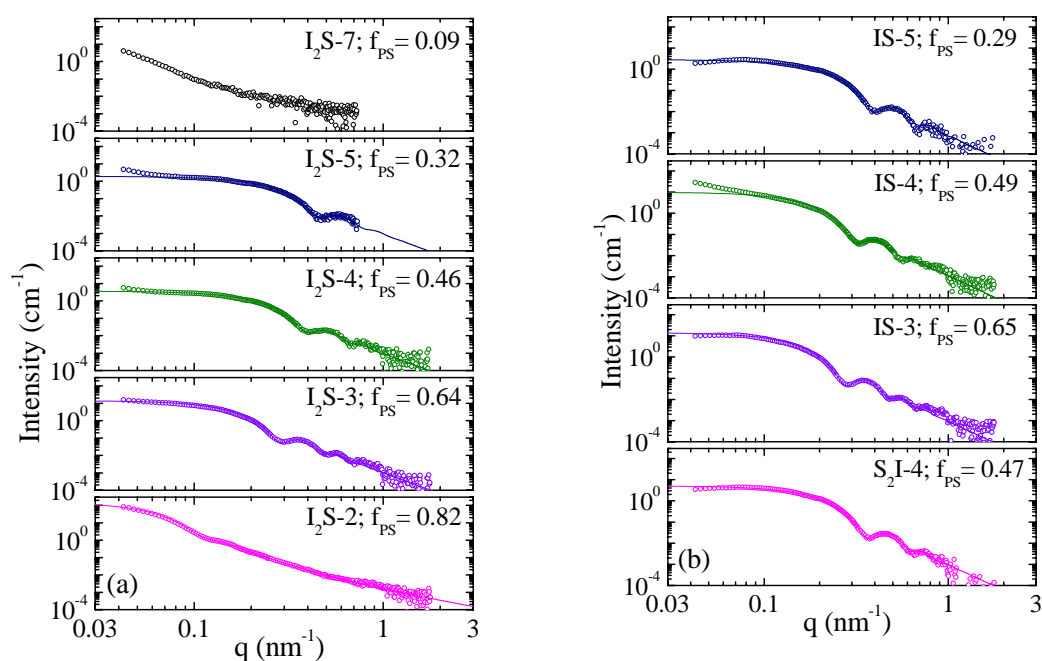


Figure 2.3.2.1: Small angle X-ray scattering intensity profiles for the 2wt% blends of the various I₂S graft copolymers (a) and the linear IS diblocks (b) in a low molecular weight polyisoprene homopolymer matrix at room temperature. The corresponding best fits are designated by solid lines.

When the polystyrene content of the copolymer increases, micellization takes place and the scattered intensity exhibits the characteristic features of the form factor of spherical scatterers, namely a plateau in the low q regime and

oscillations with well pronounced minima, the position of which agrees with the condition fulfilled by the minima corresponding to the form factor of a homogeneous sphere ($qR = 4.493, 7.725, \dots$). As the composition f_{ps} increases from 0.32 to 0.64, the position of the first minimum shifts towards lower q values, implying that the radius of the micellar core, R_c , increases. The plateau region of the sample with $f_{ps} = 0.82$ is not evident in the accessible q range; however, two weak minima appear, at even lower wavevectors with respect to the previous copolymers, and the curve can still be fitted very well with the form factor of a homogeneous sphere. Finally, the scattering profile of the blend containing the graft copolymer with the highest polystyrene volume fraction ($f_{ps} = 0.90$) is rather complex and does not correspond to the scattering from spherical particles. This sample does not form micelles but tends to phase separate and it will be discussed separately at the end of this section.

Figure 2.3.2.1b presents the scattering profiles that correspond to blends of PI with 2 wt% of three linear IS diblock copolymers as well as with the S₂I graft copolymer, which is the mirror image of I₂S-4. All of them possess the characteristic features of the form factor of a homogeneous sphere with at least two well observed minima. Similarly to the graft copolymer case, the position of the first minimum shifts to lower wavevectors as the polystyrene volume fraction of the copolymers increases. It is noted that a careful examination of the plateau region of the scattering profiles corresponding to the linear diblock copolymer blends reveals the existence of a very broad and weak peak that can be attributed to interparticle interference scattering. These peaks are too weak and broad and the attempt to apply a structure factor function in order to fit the data results in big error. Moreover, the experimental curves can be very well fitted with the form factor of a homogeneous sphere, and thus the ignoring of these weak peaks does not influence the final results.

The fitting results for the micellar core radius are presented in Figure 2.3.2.2a as a function of the polystyrene composition f_{ps} . Since the overall molecular weight of all the copolymers under study is almost the same, the results for all the different macromolecular architectures can be included in a single plot.

The error bars refer to the polydispersity in the radius as calculated from the form factor analysis, which, for most of the cases, is around 10% of the radius.

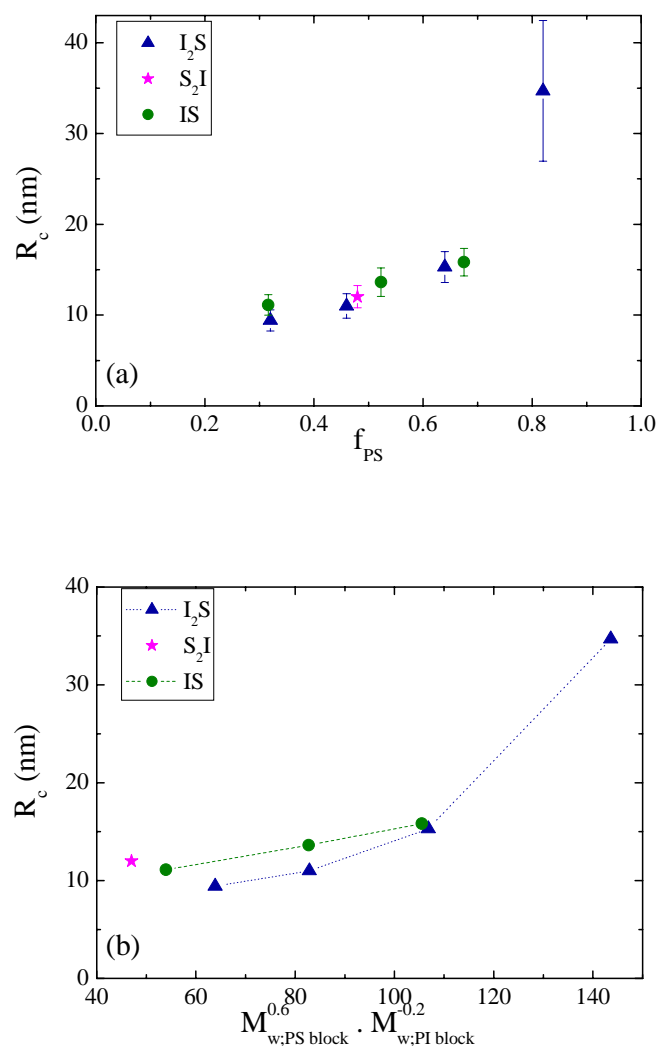


Figure 2.3.2.2: (a) The radius R_c of the micellar core of the 2wt% blends of the various linear copolymers (spheres), the I_2S grafts (triangles) and the S_2I graft (star) in polyisoprene matrix at room temperature, as derived from the form factor fit. The error bars correspond to the fitted polydispersity. (b) The dependence of the core radius on the copolymers characteristics, which reveals the influence of the grafted block on the micellization.

For both the linear and the graft copolymer micelles, the core radius increases with increasing f_{PS} , in agreement with previous studies,^{61, 65} reporting that the radius of the micellar core depends strongly on the molecular weight of the core-forming block. Although the values of the radii for the respective copolymers are very close, the core size of the graft copolymer micelles increases

more rapidly than that in the linear case, signifying that the polystyrene blocks tend to be more stretched. The increased stretching could result either from the grafting of the polyisoprene corona-forming block with a second arm of equal length or from the significant decrease in the length of the polyisoprene block at the half of its original value

The dependence of the core radius on the molecular weight of both the core- and the corona-forming blocks has been reported in the literature^{61, 65} and the empirical scaling laws $R_c \propto M_{w,core_block}^{0.6}$ and $R_c \propto M_{w,corona_block}^{-0.2}$ are provided.⁶⁵ In order to examine the origin of the different stretching of the core chains for the two macromolecular architectures, we plot the radius as a function of the product of the two scaling laws (Figure 2.3.2.2b). For the linear copolymer micelles the radii follow a linear relation, signifying that, for constant homopolymer molecular weight, the micellar size depends solely on the lengths of the two blocks in the aforementioned way. On the contrary, the graft copolymer micelles display a non-linear behavior, implying that the increase in the molecular weight of polystyrene and the decrease in that of the polyisoprene block are not enough to account for the behavior of the graft copolymer micelles. This should be related to the fact that in the I₂S systems, there are two smaller polyisoprene blocks per junction point instead of a longer one. Apparently, this influences the micelle characteristics even more for high core-block content. However, there is another possibility that cannot be overlooked: it refers to whether the micellar structures formed by the I₂S-2 copolymer with high core-forming block and small corona-forming one are not spherical. The SAXS data, however, although less clear than those for the blends with lower f_{PS} , indicate more like a spherical geometry.

The aggregation number Q_m can provide complementary information on the micellar structure. As shown in Figure 2.3.2.3, the aggregation numbers of the micelles formed by the graft copolymers increase rapidly with increasing volume fraction of the core-forming polystyrene block in contrast to the case of the linear diblock copolymer micelles, where Q_m shows a very weak dependence on copolymer. This finding is consistent with the increased core radius of the graft

copolymer micelles and, thus, the increased stretching discussed previously. Another possible explanation for the different behavior of the aggregation number could be related to the penetration of homopolymer chains within the core, which would decrease the number of copolymer chains needed to form a micelle while keeping unaltered the core radius for low values of the polystyrene block molecular weight. An estimation based on a calculated phase diagram, however, does not allow for the incorporation of significant number of the matrix polyisoprene chains within the core, and, thus, this possibility should be excluded. Moreover, the ratio of the volume of the scatterers (core) to the volume estimated by the form factor analysis can provide an indication about the polystyrene volume fraction within the core. For the present micelles, this ratio is found to have a constant value, independent of both the molecular and the architectural characteristics, reinforcing the validity of the results. Thus, the behavior of the aggregation number can be only attributed to the packing due to the different stretching of the polystyrene chains inside the micellar core.

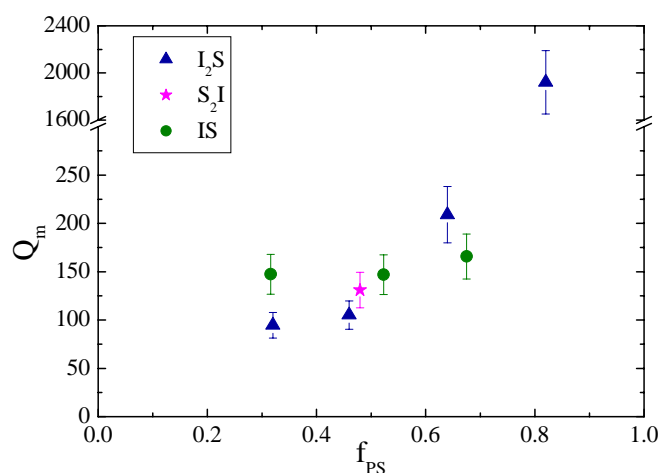


Figure 2.3.2.3: The aggregation number Q_m of the micelles, calculated from the analysis of the forward scattering, for the 2wt% blends of the various linear copolymers (spheres), the I₂S grafts (triangles) and the S₂I graft (star) in polyisoprene matrix at room temperature.

The volume fraction of the copolymer chains participating in micelles formation, ϕ_{mic} , and the free unimers in the blends, ϕ_{uni} , have been estimated for

the 2 wt% blends of the various linear and graft copolymers within the polyisoprene matrix. For most samples ϕ_{mic} is more or less constant, independent of the molecular characteristics, and almost equal to 60% of the total copolymer volume fraction. Consequently, the number density of micelles in the blends decreases as the copolymers composition f_{PS} increases, in order to compensate for the increase in the radius. Only for the graft copolymer with $f_{\text{PS}} = 0.82$, ϕ_{mic} decreases to 30% of the total copolymer volume fraction. One possible explanation for this low value can be that there is an incipient macrophase separation in that system due to the high molecular weight of the polystyrene block, which is not evident in the x-ray scattering profile. It should be noted, however, that the samples of this blend are not opaque in contrast to the appearance of the blends with $f_{\text{PS}} = 0.90$ to be discussed in relation to Figure 2.3.2.4 below.

Table 2-4

The Molecular Characteristics and the Small Angle X-ray Scattering Results for the I₂S, S₂I and IS Copolymers. The overall molecular weights and compositions are the same for all samples

Species	$M_{w, \text{PS block}}$	$M_{w, \text{PI block}}$	R_c (nm)	Q_m	$Q_m \times (\text{PS arms})$	ϕ_{mic}/ϕ
I ₂ S-4	45,080	23,460	11.0	105	105	0.54
S ₂ I-4	22,320	48,360	12.0	131	262	0.62
IS-4	59,120	54,580	13.6	147	147	0.74

In order to quantitatively probe and understand the influence of the macromolecular architecture on the micelle characteristics, one can compare the results for the I₂S-4 and S₂I-4 graft copolymers and the linear IS-4 diblock. These are copolymers that nearly have almost the same total molecular weight and composition ($f_{\text{PS}} \approx 0.5$) but differ in the number of isoprene versus the number of styrene arms (note that the molecular weight of IS-4 is slightly higher). The molecular characteristics of the copolymers are presented in Table 2-4 along with the experimental results concerning the radius of the core, the aggregation number and the ratio of copolymer chains participating in micelle formation with respect

to the total amount of copolymers in the blend, ϕ_{mic}/ϕ . Although the molecular weight of the core-forming block changes by a factor of two between S₂I-4 and the other two copolymers, the influence on the core radius is not that pronounced; in fact, the core radius increases in the order I₂S-4 < S₂I-4 < IS-4. One may have expected that the S₂I-4 graft would form much smaller micelles due to the half molecular weight of its polystyrene block with respect to the other copolymers, but apparently the existence of the second polystyrene block, which is incorporated within the micellar core, can influence the micellar characteristics. If one examines the behavior of the aggregation number, one sees that it increases in the order I₂S-4 < S₂I-4 < IS-4, similarly to the behavior of the core radius. One should note that the number of polystyrene blocks forming the core of the S₂I-4 graft copolymer micelles is almost three times that of the I₂S-4 copolymer since there are two styrene arms per S₂I molecule. This means that the low molecular weight of the polystyrene block is counterbalanced by the increased number of chains forming the core, which result in micelles of similar size. This finding may imply that the size of the core is not only driven by the length of the core-forming block but mostly by a critical volume necessary for the formation of stable micelles. The same trends for the core radius and the aggregation number have been also reported for the micellization of the same copolymers in a selective solvent.⁸⁰ Moreover, in another section a series of symmetric I_nS_n star block copolymers possessing *n* polystyrene and *n* polyisoprene blocks is examined and it was found that the radii of the core were independent of *n* whereas the aggregation number showed a *n*⁻¹ dependence. In the present systems, the dependencies are not that simple probably because the copolymers are not architecturally symmetric and the molecular weight and the number of the polystyrene and polyisoprene blocks influence the behavior in a still not understandable way.

In the same Table the fraction of copolymer chains participating in micellization, ϕ_{mic}/ϕ , is provided. Once more, this fraction increases in the order I₂S-4 < S₂I-4 < IS-4, demonstrating the stronger matrix polyisoprene –

polystyrene segregation of the linear diblock that has a larger polystyrene block, followed by the two-polystyrene armed graft copolymer.

Finally, the phase behavior of the 2 wt% blend of the graft copolymer with $f_{ps} = 0.90$, which does not form spherical micelles, demonstrates another example of the influence of the macromolecular characteristics and architecture on the micellization process. As already mentioned, the scattering profile of this blend is rather complex and does not correspond to the form factor of spherical scatterers. However, some clear features are present that could allow a rough estimate of the structural characteristics. Since the objective of the present report is the study of the micellar characteristics no other complementary technique, like TEM, has been applied in order to fully characterize this sample and the structural investigation was limited to the results derived from the scattering data.

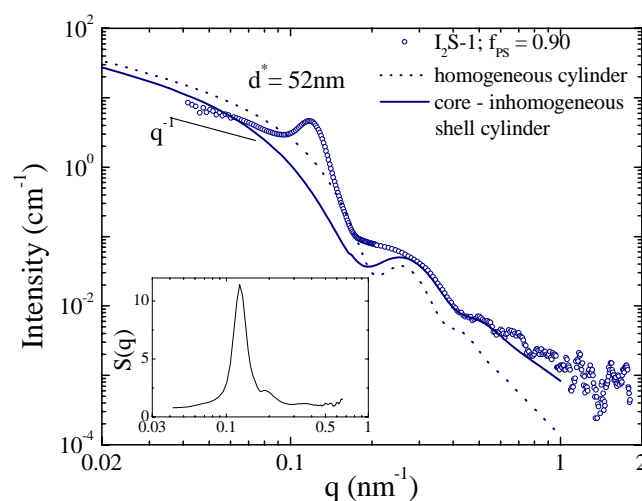


Figure 2.3.2.4: The scattering profile for the 2wt% blend of the I₂S-1 graft copolymer in the polyisoprene matrix. The simulated scattering curves for homogeneous cylinders with $R = 19.8$ nm (dot line) and core-shell cylinders with inhomogeneous shell and radii $R_c = 22$ nm and $R_s = 30$ nm (solid line) are included as well.

As we can see in Figure 2.3.2.4, a broad peak is observed around 0.12 nm^{-1} which is attributed to interparticle interference scattering. This corresponds to a characteristic mean distance between the scatterers of approximately 52 nm. No higher order peaks are evident, so no other estimate on the lattice characteristics is possible. Moreover, a q^{-1} dependence that is characteristic of the scattering from

rod-like particles is apparent in the low q range and a clear minimum appears around 0.4 nm^{-1} , possibly followed by higher order minima. Thus, we can safely derive that there is an interacting system of elongated particles with a spacing of around 52 nm. In order to have an estimate on the characteristics of the particles, various form factors that describe elongated particles were attempted to simulate the experimental curve (apart from the interference peak). The simulated curve that corresponds to the scattering from homogeneous cylinders of 19.8 nm radius is presented in Fig. 2.3.2.4: the q^{-1} dependence and the minimum at 0.4 nm^{-1} are both reproduced but yet the intensity does not comply well with the experimental values, which predisposes for a core-shell structure. Indeed, the agreement is getting better when the form factor is simulated for core – homogenous shell cylinders, but the best conformity is obtained when simulating the form factor of core – inhomogeneous shell cylinders.⁹⁵ An algebraic density profile has been used for the shell, which is considered to be valid for the description of systems with grafted polymer chains⁹⁵ like the one under study, since the soluble block of the copolymer forms a polymer brush that surrounds the insoluble core. The simulated curve that best describes the form factor contribution to the experimental data is included in Fig. 2.3.2.4 and corresponds to cylindrical particles with a inner radius of 22 nm and an outer radius of 30 nm. Using this form factor, the structure factor can be calculated, which is shown in the inset of Fig. 2.3.2.4; it exhibits a relatively strong peak with a full width at half maximum that would correspond to a coherence length of 161 nm or three times the characteristic distance of 52 nm.

An interesting finding is that the electron density of the core is lower than that of the shell, signifying that the polyisoprene block resides in the core while the polystyrene blocks form the shell, unlike what has been observed for the other systems. This can only happen if a macrophase separation had occurred with copolymer-rich domains and homopolymer-rich regions; indeed this sample was not transparent within the SAXS glass tubes as the other specimens were. In this case, the copolymer in the copolymer rich domains can form a morphology similar to that in its bulk with the minority component (polyisoprene in this case) forming the inside of the cylinders which are dispersed in a weakly ordered

fashion within the polystyrene matrix. This morphology is in agreement with that of the same copolymer, both in the pure state⁷³ and blended with small amounts of low molecular weight polyisoprene.⁷⁷ It was found that the pure copolymer forms hexagonally packed polyisoprene cylinders in a polystyrene matrix with a lattice spacing of 31nm,⁷³ while bilayered sheets and closed vesicles are observed after blending.⁷⁷ Using simple geometry and applying the space filling condition for the pure copolymer case, one could derive the radius of the polyisoprene cylinders as $R_{PI} = 6.2\text{nm}$ and the distance between the cylinders as $d_{PS} = 23\text{nm}$. One would expect that the same core radius should apply in the present system; however, the larger radius derived implies that homopolymer polyisoprene exists within the cylinder core. Additionally, assuming hexagonal packing of the cylinders and considering that the distance between them is equal to that calculated for the pure copolymer, d_{PS} , the radius of the PI core is estimated to be around 18 nm, which is very close to the experimentally estimated value.

Thus, it is concluded that copolymer-rich domains, which exhibit a cylindrical morphology with cylinders formed by the polyisoprene block swollen with polyisoprene homopolymer in a matrix of the polystyrene-block, are present within the homopolymer matrix. This is due to the very high molecular weight of the polystyrene arm and the very low molecular weight of the polyisoprene ones that lead to the immiscibility of the copolymer with the homopolymer driving the macrophase separation. In the other limit of the very low molecular weight of the polystyrene arm and the large molecular weight of the polyisoprene ones (I₂S-8) the copolymer was completely miscible with the PI homopolymer and no micelles were observed even at concentration of 4 wt%. In the intermediate range of composition (and, thus, of molecular weights) the unfavorable interactions have lead to the formation of the copolymer micelles within the PI matrix.

2.3.3 Micellization of S_nI_n Miktoarm Star Copolymers

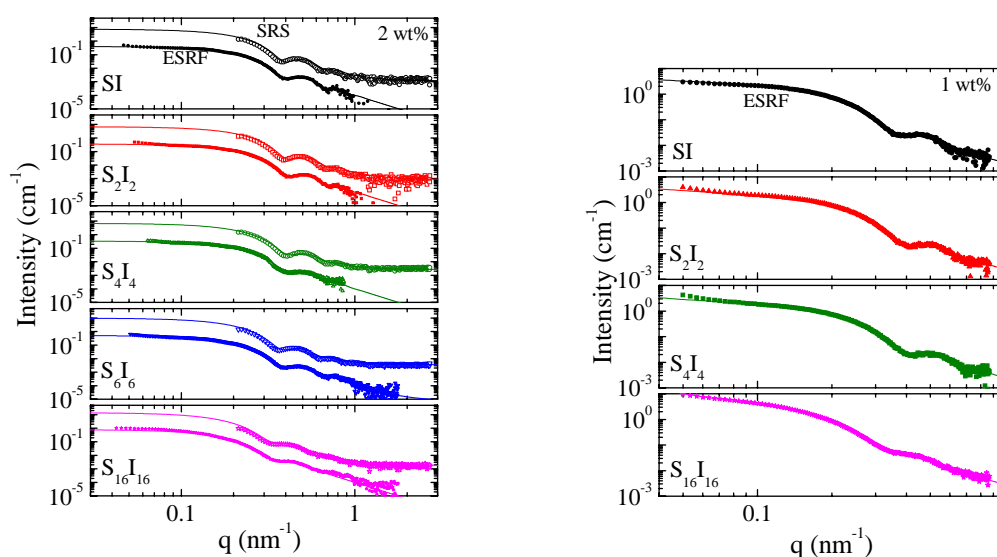


Figure 2.3.3.1: Small angle X-ray scattering intensity data for the 2 wt% and 1 wt% blends of the various S_nI_n miktoarm copolymers (n values are shown in the legend) within a PI homopolymer matrix at room temperature as a function of the scattering vector q . For the 2wt%, data are shown measured at SRS (upper curves) and ESRF (lower curves), where the lower curves have been shifted down by a decade for clarity. The scattering curves obtained from the analysis of the ESRF profiles are shown on top of the ESRF data and shifted vertically to be compared to the SRS data that they describe very well, too.

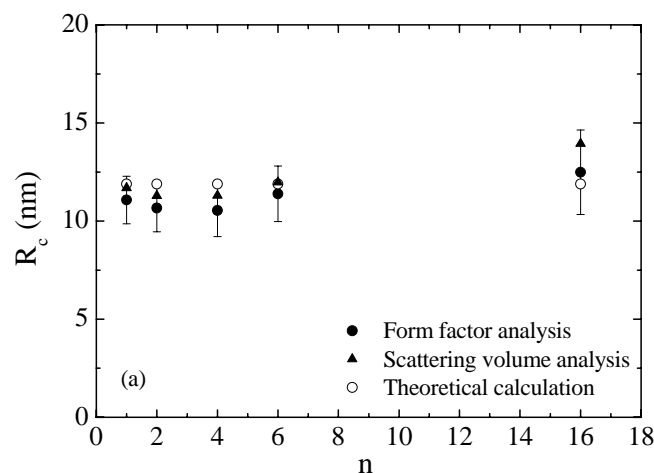
Figure 2.3.3.1 shows the scattering intensity for the 2 wt% and the 1 wt% blends of the various S_nI_n miktoarm copolymers in the PI homopolymer matrix as a function of the scattering vector q . The 2wt% samples were measured both at SRS – Daresbury (upper curves) and at ESRF (lower curves); note that the ESRF data have been shifted down by one decade for clarity. The characteristic oscillations corresponding to spherical scatterers are observed for both concentrations and the position of at least two well-observed minima (for the 2wt%) agree with the condition fulfilled by the minima corresponding to the form factor of a sphere. The availability of scattering data at very low wavevectors, q , in the ESRF measurements confirms the existence of spherical micelles. Indeed, the scattered intensity at the low q -range is q -independent, validating the spherical

shape of the micelles. The data from the two independent measurements are in excellent agreement, verifying the stability of the equilibrium micelles.

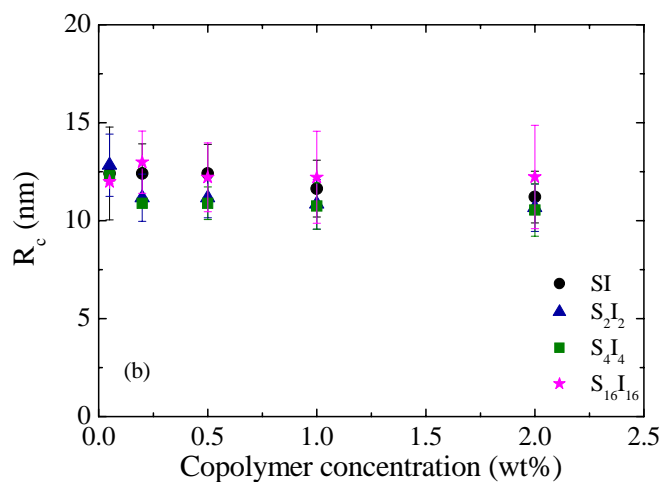
The positions of the minima in the scattering curves are determined by the radii of the scatterers; the data for all copolymers exhibit similar minima, implying that the size of the micellar core is almost constant in all cases. The sharpness of the minima is reduced when the number of arms increases indicating increasing polydispersity in the core radii. It is noted that a rule of thumb is that if a single minimum is observed then the polydispersity is $\Delta R/R \approx 0.1$, for two minima $\Delta R/R < 0.1$, while for three $\Delta R/R \approx 0.02$. These observations are confirmed by the quantitative data analysis. The calculated scattering curves obtained by the three-parameter minimization procedure, described in the experimental part, are included in Fig. 2.3.3.1 as well. The fitting curves presented here correspond to the ESRF profiles and are shifted vertically in order to prove the consistency between the two measurements and establish the validity of the fitting results. A constant parameter y_0 , independent of q , is additionally required to fit the constant background in the high q range of the SRS measurements. This parameter is considered to be of minor importance, since the value of y_0 is negligible with respect to I_0 and does not affect the best fit values of the parameters related to the micelle characteristics. In principle, this parameter should include all the background-like corrections that were not taken into account by the subtraction of the scattering of the pure polyisoprene (for example, the density fluctuations of polystyrene).

Figure 2.3.3.2a shows the radii of the polystyrene cores of the micelles formed by the various S_nI_n miktoarm copolymers within the PI matrix as a function of the functionality n . The solid spheres correspond to the values obtained directly by fitting the scattering curves to the form factor of spherical scatterers, while the values designated by solid triangles were obtained from the volume of the scatterers, V . Despite the fact that the polydispersity introduces an error to the calculation of the scattering volume, resulting in somehow higher values, the two independent ways provide essentially the same results within the error bars (mainly due to the polydispersity). It is evident that the micelles that are formed for all copolymers have a more or less constant core radius of ~ 11 nm,

similar to that observed for the respective linear diblock copolymer ($n=1$), independent of the number of arms n and, therefore, of the copolymer architecture. Thus, it is the M_w of the individual polystyrene and polyisoprene arms that determines the size of the core.



(a)

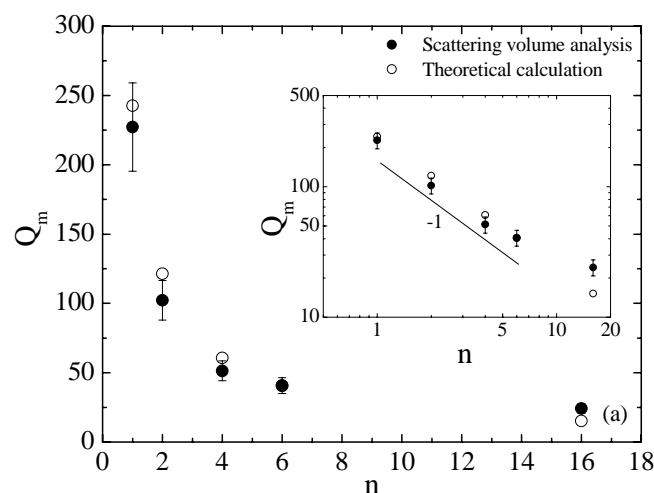


(b)

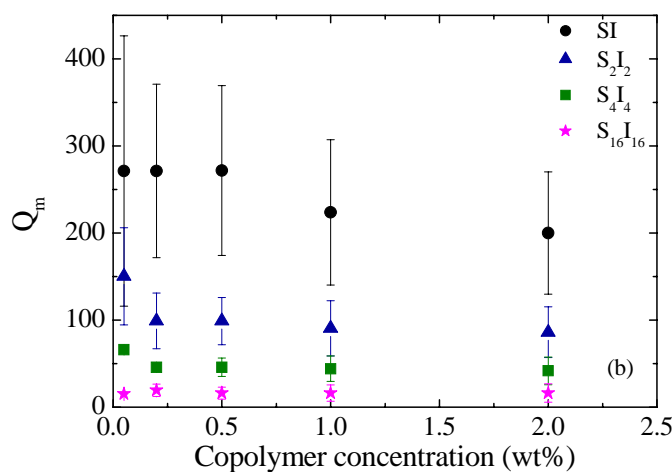
Figure 2.3.3.2: (a) Radii R_c of the micelle cores formed by the S_nI_n miktoarm star copolymers in a PI homopolymer at room temperature (2 wt% blends) as a function of the functionality n ; the radii are calculated from the form factor analysis of the scattering data (filled spheres) and from the estimated scattering volumes V (filled triangles). The error bars correspond to the best fit polydispersity values. The hollow spheres correspond to the core radii values obtained from the theoretical model described in the text. (b) Radii R_c of the micelle cores formed by the S_nI_n miktoarm star copolymers in a PI homopolymer at room temperature as a function of copolymer concentration for various star functionalities n . The radii are calculated from the form factor analysis of the scattering data.

Figure 2.3.3.2b shows the core radius of the micelles as a function of the concentration of the block copolymer within the homopolymer matrix. For all values of the functionality n of the S_nI_n copolymers, the micellar radius is independent of concentration signifying stable copolymer micelles for this range of concentrations. The polydispersity in the core radius, which is denoted in the graphs by the error bars, is approximately 1.2 nm for all the samples, that is about 10% of the radius, although it seems to be slightly higher for the $n = 16$ copolymer $S_{16}I_{16}$, probably due to the small number of chains aggregated to form a single micelle (to be discussed in relation to Fig. 2.3.3.3 below). This is a reasonable value, since it originates from two independent factors, the diffuse interface between the core and the corona, due to the polymeric nature of the components, and the size distribution of the micellar cores.⁶⁰ Moreover, the data do not suggest a systematic influence of the functionality on the observed polydispersities, suggesting, once more, that the structure of the micelles does not depend on the copolymer architecture.

Figure 2.3.3.3a shows the aggregation number, Q_m , i.e., the number of copolymer chains per micelle, as a function of the functionality of the star copolymers n . Q_m decreases rapidly with increasing number of arms exhibiting a n^{-1} dependence as seen in the log-log representation shown in the inset of Fig. 2.3.3.3a. This result can be anticipated based on the data of Fig. 2.3.3.2a, which showed that the radius and, thus, the volume of the core was constant independent of the functionality n . Assuming that the density of the core is constant and equal to that of pure polystyrene, the total number of arms that form the core should, then, be constant as well. This total number of arms in a micelle is the product of $n \times Q_m$; thus, Q_m should follow the observed n^{-1} dependence. Therefore, the dependence of Q_m on n is due to an apparent need for constant micelle mass. Figure 3b shows the copolymer concentration dependence of the aggregation number Q_m for the various star functionalities n . Similarly to the core radius of Fig. 2.3.3.2b, the aggregation number is more-or-less independent of the concentration whereas it shows the n^{-1} dependence (similar to that in the inset of Fig. 2.3.3.3a) for all concentrations.



(a)



(b)

Figure 2.3.3.3: (a) The micellar aggregation number Q_m calculated from the X-ray scattering patterns for the 2wt% blends of the various S_nI_n miktoarm star copolymers within a PI homopolymer matrix at room temperature (filled spheres). The open spheres correspond to the aggregation number values obtained from the theoretical model described in the text. In the inset, the corresponding log-log representation is shown, indicating that the aggregation number follows a n^{-1} power law. (b) The micelle aggregation number Q_m , calculated from the X-ray patterns of the various S_nI_n miktoarm star copolymers within a PI homopolymer matrix at room temperature, as a function of copolymer concentration for various star functionalities.

Figure 2.3.3.4 shows the fractions ϕ_{mic} and ϕ_{uni} of copolymer chains that reside within the micelles or remain as homogeneously mixed unimers, respectively, for the 2wt% and the 0.5wt% blends of the various S_nI_n miktoarm copolymers within the PI matrix. For all samples the volume fraction of

copolymer chains forming micelles is practically constant and almost half of the total fraction of copolymer added to the blends. Consequently, the number density N_p of micelles is constant as well and it is calculated to be equal to 7×10^{-7} micelles/nm³ (or 7×10^{14} micelles/cm³) for the 2wt% blend and 1.6×10^{-7} micelles/nm³ for the 0.5wt% blend.

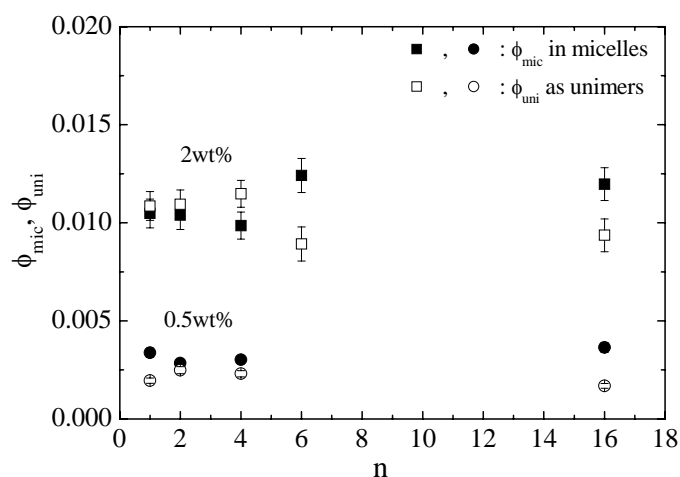


Figure 2.3.3.4: The volume fraction of copolymer chains participating in micelles (filled squares) and unimers (open squares) for the 2 wt% and 0.5 wt% blends of the various S_nI_n miktoarm star copolymers in polyisoprene homopolymer matrix at room temperature.

The large volume fraction of unimers observed in the samples seems inconsistent with the existing perception on the micellization of block copolymers,^{27, 55, 57} which estimates that the volume fraction of free (non-aggregated) chains should be equal to that corresponding to the critical micellization concentration (CMC), in accordance with the theories concerning the self-assembly of surfactant molecules.⁹⁶ It is noted that the 0.5-2wt% concentration range is not close to the CMC;⁹⁷ the previous finding is not because of such proximity. It appears that this finding is consistently observed in block copolymer / homopolymer mixtures; Kinning et al.,⁶⁵ Major et al.,⁷⁰ and Gohr et al.⁶⁹ had observed that, for blends containing lower molecular weight homopolymers or copolymers the amount of non-aggregated (free) copolymer increased beyond the CMC as the copolymer concentration increased. Gohr, et al.⁶⁹ reported experimental results where, far above the CMC, the volume fraction

of the free chains is comparable to that of the chains participating in micelles, noting that, in block copolymer/homopolymer melts, the CMC is less well-defined than in surfactant solutions in agreement with Monte Carlo simulations.⁶⁰ Thus, the volume fractions of unimers observed in our systems, although apparently large, are in very good agreement with earlier investigations. It should be noted that relaxing the assumption that the core consists of pure polystyrene does not affect qualitatively the presented results. For small fractions of PI penetrating into the core (less than 10%), the volume fraction of copolymer chains forming micelles increases slightly. The PI fraction within the core should reach up to 30% in order for ϕ_{uni} to become negligible with respect to ϕ_{mic} .

2.3.4 Theoretical Considerations on the Micellization of A_nB_n Stars

The chemical potential of a copolymer chain within a micelle and, thus, the characteristics of the formed micelles can be calculated following the methodology that Leibler⁵⁷ presented for the case of diblock copolymers and for long homopolymer chains that do not penetrate within the corona of the micelles. Leibler⁵⁷ considered spherical diblock copolymer micelles whereas the procedure was extended by Shull, et al.⁹ for cylindrical and lamellar diblock copolymer micelles and by Lyatskaya, et al.^{36, 37} for spherical micelles of simple AB_2 grafts within a B homopolymer. Semenov⁵² developed an analytical mean-field theory for the equilibrium of block copolymers in a homopolymer layer between an interface with another homopolymer and the free surface. In recent papers, Retsos et al.⁵³ adopted the methodology of Leibler and presented the complete calculations for either AB diblocks or AB_2 graft copolymers (added to an A or a B homopolymer) and for all three geometries (spherical, cylindrical, lamellar). Here, the approach is extended for the case of A_nB_n miktoarm star copolymers within a B homopolymer matrix. The theoretical calculations will, then, be compared to the experimental data presented above.

Spherical Micelles. When an A_nB_n miktoarm copolymer is added to a B homopolymer, the micelles are formed with a core made up of the ($n Q_m$) A-blocks of the Q_m aggregating copolymer molecules and a corona consisting of the respective ($n Q_m$) B-blocks. Assuming incompressibility, the radius of the core R_A is, thus,

$$R_A = \left(\frac{3}{4\pi} \right)^{1/3} \left(Q_m f_A n N b^3 \right)^{1/3} \quad (2.3.1)$$

where Q_m is the aggregation number, f_A is the volume fraction of the A arms, N is the number of segments of the respective A-B diblock and b is the statistical segment length. It is assumed that both types of links have the same segmental volume $v = b^3$. The free energy of the micelle is represented by a sum of three contributions:

$$F_{mic} = A\gamma_0 + F_{core} + F_{corona} \quad (2.3.2)$$

where $A = 4\pi R_A^2$ is the interfacial area and $\gamma_0 = k_B T b^{-2} (\chi/6)^{1/2}$ is the A/B interfacial tension assumed independent of the number of segments of the two blocks for a highly incompatible situation.^{98, 99} $k_B T$ is the thermal energy and χ is the Flory-Huggins interaction parameter.

The core free energy is associated with the non-uniform stretching of the A blocks arising from constraining the copolymer A-B junction to a narrow interface; for the A-B diblock copolymer case, it has been calculated self-consistently by Semenov.¹⁰⁰ For an $A_n B_n$ miktoarm copolymer, one has to take into account the existence of the n A-blocks per copolymer chain within the core, not only as a multiplication factor but also in modifying the stretching of the trajectory. Thus,

$$F_{core} / k_B T = n^{5/3} \left(\frac{3}{4} \right)^{5/3} \left(\frac{\pi^{4/3}}{20} \right) Q_m^{5/3} (f_A N)^{-1/3} \quad (2.3.3)$$

The free energy of the corona is calculated assuming that all the free ends of the B blocks reach the radius R of the whole micelle and that there is no penetration of the homopolymer chains into the corona, but taking into account the non-uniform deformation of the B blocks due to the spherical geometry. The existence of the n B-blocks in the corona results in the modification of the stretching of the classical trajectory $r(k)$ of the segment number k as $dr(k)/dk = nQ_m b^3 / 4\pi r^2$. Therefore,⁵⁷

$$F_{corona} / k_B T = n \frac{3}{2b^2} Q_m \int_{R_A}^R dr \frac{dr(k)}{dk} = n \frac{3}{2b^2} Q_m \int_{R_A}^R dr \frac{nQ_m b^3}{4\pi r^2} \quad (2.3.4)$$

Assuming incompressibility, the micellar radius R is

$$R = \left(\frac{3}{4\pi} \right)^{1/3} (Q_m n N b^3)^{1/3} \quad (2.3.5)$$

and, thus,

$$F_{corona} / k_B T = \frac{n^{5/3}}{2} \left(\frac{3}{4\pi} \right)^{2/3} Q_m^{5/3} N^{-1/3} (f_A^{-1/3} - 1) \quad (2.3.6)$$

The equilibrium value of Q_m is obtained by minimizing the free energy per chain F_{mic}/Q_m with respect to Q_m , $\partial(F_{mic}/Q_m)/\partial Q_m = 0$, whereas the chemical potential is determined by

$$\mu_{mic} = F_{mic}/Q_m \Big|_{Q=Q_{m_{min}}} \quad (2.3.7)$$

where $Q_{m_{min}}$ is the value at the minimum of F_{mic}/Q_m . Therefore,

$$Q_{m_{min}} = \frac{1}{n} \left(\frac{3}{2} \right)^{1/2} \left(\frac{4\pi}{3} \right) \chi^{1/2} N f_A^{2/3} \left(1.74 f_A^{-1/3} - 1 \right)^{-1} \quad (2.3.8)$$

whereas the chemical potential for a $A_n B_n$ miktoarm copolymer chain in a spherical micelle within homopolymer B is

$$\mu_{mic}^{sph} / k_B T = n \left(\frac{3}{2} \right)^{4/3} f_A^{4/9} (\chi N)^{1/3} \left(1.74 f_A^{-1/3} - 1 \right)^{1/3} \quad (2.3.9)$$

Comparing eqs. 2.3.8 and 2.3.9 with the respective ones calculated for the A-B diblock copolymer case,^{9, 36, 37, 52, 53} one can determine that

$$Q_{m_{min}}^{sph}(A_n B_n) = \frac{1}{n} Q_{m_{min}}^{sph}(AB) \quad \text{and} \quad \mu_{mic}^{sph}(A_n B_n) = n \mu_{mic}^{sph}(AB) \quad (2.3.10a)$$

It is noted that the expression for $\mu_{mic}^{sph}(AB)$ is identical to eq. A-8 of Shull et al.⁹ and consistent with eq. 21 of Lyatskaya et al.^{36, 37} and eq. 36 of Semenov.⁵²

For a series of samples like the ones of the present investigation, where f_A , N and χ are kept constant, Q_m depends only on the number of arms n , and, more precisely, it is predicted to follow a n^{-1} power law. Substituting eq. 2.3.8 into eq. 2.3.1 and eq. 2.3.6, the core and the micelle radius can be calculated:

$$R_A^{sph}(A_n B_n) = \left(\frac{3}{2} \right)^{1/6} b (\chi f_A N)^{1/6} (f_A N)^{1/2} f_A^{-1/9} \left(1.74 f_A^{-1/3} - 1 \right)^{-1/3} = R_A^{sph}(AB) \quad (2.3.10b)$$

$$R^{sph}(A_n B_n) = \left(\frac{3}{2} \right)^{1/6} b (\chi N)^{1/6} N^{1/2} f_A^{2/9} \left(1.74 f_A^{-1/3} - 1 \right)^{-1/3} = R^{sph}(AB) \quad (2.3.10c)$$

Both are independent of n and depend only on the characteristics of the respective A-B diblock. The simplicity of the results concerning the chemical potential and the aggregation number of the $A_n B_n$ copolymers with respect to the respective AB diblock copolymers originates from the indirect assumption that the junction point of the miktoarm does not contribute significantly to the free energy of the

micelle. The validity of this assumption is essentially verified by the comparison with the experimental data.

Cylindrical Micelles. In this case, the n A-arms make a core of radius

$$R_A = \left(Q_m f_A n N b^3 / (\pi L) \right)^{1/2} \quad (2.3.11)$$

where L is the length of the cylindrical micelle. The B-arms form the corona, which extends up to radius R

$$R = \left(Q_m n N b^3 / (\pi L) \right)^{1/2} \quad (2.3.12)$$

The free energy of the micelle is represented by eq. 2.3.2, where the interfacial area is now $A = 2\pi R_A L$. For the calculation of the core free energy one has to take into account the existence of the n A-blocks not only as a multiplication factor but also in modifying the stretching of the trajectory. Thus, the equation⁵³ proposed by Shull et al.⁹ and Semenov¹⁰⁰ is modified to

$$F_{\text{core}} / k_B T = n \frac{0.616 Q_m R_A^2}{f_A N b^2} \quad (2.3.13)$$

Regarding the calculation of the corona free energy, the stretching of the classical trajectory is now calculated as

$$dr(k) / dk = n Q_m b^3 / (2\pi L r) \quad (2.3.14)$$

and, therefore,

$$F_{\text{corona}} / k_B T = -n^2 \frac{3}{8\pi} Q_m^2 b L^{-1} \ln f_A \quad (2.3.15)$$

The equilibrium value of Q_m is obtained by minimizing F_{mic}/Q_m with respect to Q_m , as

$$Q_{m_{\text{min}}} = \frac{1}{n} 3.326 (\chi f_A N)^{1/3} (L/b) (1.64 - \ln f_A)^{-2/3} \quad (2.3.16)$$

The chemical potential for a $A_n B_n$ miktoarm copolymer chain in a cylindrical micelle within homopolymer B is

$$\mu_{\text{mic}}^{\text{cyl}} / k_B T = n 1.19 (\chi f_A N)^{1/3} (1.64 - \ln f_A)^{1/3} \quad (2.3.17)$$

Similarly to the case of spherical micelles, comparing eqs. 2.3.16 and 2.3.17 with the respective ones calculated for the A-B diblock copolymer case,^{9, 53} one finds that

$$Q_{m_{\min}}^{cyl}(A_n B_n) = \frac{1}{n} Q_{m_{\min}}^{cyl}(AB) \quad \text{and} \quad \mu_{mic}^{cyl}(A_n B_n) = n \mu_{mic}^{cyl}(AB) \quad (2.3.18a)$$

$$R_A^{cyl}(A_n B_n) = 1.03b(\chi f_A N)^{1/6} (f_A N)^{1/2} (1.64 - \ln f_A)^{-1/3} = R_A^{cyl}(AB) \quad (2.3.18b)$$

$$R^{cyl}(A_n B_n) = 1.03b(\chi N)^{1/6} N^{1/2} f_A^{1/6} (1.64 - \ln f_A)^{-1/3} = R^{cyl}(AB) \quad (2.3.18c)$$

Lamellar Micelles. In this case, the dimension of the core made by the n A-blocks is

$$R_A = n Q_m f_A N b^3 / A \quad (2.3.19)$$

where A is the interfacial area and R_A is half the thickness of the inner lamellae. The n B-blocks form the corona, which extends up to distance

$$R = n Q_m N b^3 / A \quad (2.3.20)$$

from the center of the inner lamellae.

For the calculation of the core free energy again one has to take into account the existence of the n A-blocks not only as a multiplication factor but also in modifying the stretching of the trajectory. Thus,

$$F_{\text{core}} / k_B T = n \frac{1.234 Q_m R_A^2}{f_A N b^2} \quad (2.3.21)$$

For the calculation of the corona free energy, the stretching of the classical trajectory is now

$$dr(k) / dk = n Q_m b^3 / A \quad (2.3.22)$$

Therefore,

$$F_{\text{corona}} / k_B T = n^3 \frac{3}{2A^2} Q_m^3 N b^4 (1 - f_A) \quad (2.3.23)$$

The equilibrium value of Q_m is obtained by minimizing F_{mic}/Q_m with respect to Q_m as

$$Q_{m_{\min}} = \frac{1}{n} 0.9155 A \chi^{1/6} N^{-1/3} b^{-2} (5.64 - f_A)^{-1/3} \quad (2.3.24)$$

whereas the chemical potential for an $A_n B_n$ miktoarm copolymer chain in a lamellar micelle within homopolymer B is

$$\mu_{mic}^{lam} / k_B T = n 0.669 (\chi N)^{1/3} (5.64 - f_A)^{1/3} \quad (2.3.25)$$

Again, comparing eqs. 2.3.24 and 2.3.25 with the respective calculated for the A-B diblock copolymer case,^{9, 53} one can observe that

$$Q_{m_{\min}}^{lam}(A_n B_n) = \frac{1}{n} Q_{m_{\min}}^{lam}(AB) \quad \text{and} \quad \mu_{mic}^{lam}(A_n B_n) = n \mu_{mic}^{lam}(AB) \quad (2.3.26a)$$

$$R_A^{lam}(A_n B_n) = 0.9155b (f_A \chi N)^{1/6} (f_A N)^{1/2} f_A^{1/3} (5.64 - f_A)^{-1/3} = R_A^{lam}(AB) \quad (2.3.26b)$$

$$R^{lam}(A_n B_n) = 0.9155b (\chi N)^{1/6} N^{1/2} (5.64 - f_A)^{-1/3} = R^{lam}(AB) \quad (2.3.26c)$$

Unimer chains freely distributed in the bulk. The free energy density of a homogeneous mixture of an $A_n B_n$ copolymer with a B homopolymer with P_B number of segments is derived following Semenov⁵²

$$\frac{F_{\text{bulk}}}{k_B T} = \frac{\phi}{nN} \ln\left(\frac{\phi}{e}\right) + \frac{1-\phi}{P_B} \ln\left(\frac{1-\phi}{e}\right) + \chi \phi f_A (1 - f_A \phi) \quad (2.3.27)$$

Thus, the chemical potential of a miktoarm copolymer chain homogeneously distributed in the bulk B homopolymer, $\mu_{\text{bulk}} = nN[(1-\phi)\partial F_{\text{bulk}}/\partial\phi + F_{\text{bulk}}]$, is

$$\frac{\mu_{\text{bulk}}}{k_B T} = \ln\phi - \phi - (1-\phi)\frac{nN}{P_B} + \chi f_A nN(1 - 2f_A\phi + f_A\phi^2) \quad (2.3.28)$$

where ϕ is the copolymer volume fraction in the homopolymer phase.

For the cases when micelles are present, the equilibrium is established between copolymer chains homogeneously distributed within the homopolymer phase and copolymer chains participating in micelle formation. The thermodynamic equilibrium is determined by the equation

$$\mu_{\text{mic}} = \mu_{\text{bulk}}(\phi_{\text{uni}}) \quad (2.3.29)$$

which, in principle, determines the volume fraction ϕ_{uni} of copolymers remaining as unimers homogeneously distributed in the bulk A or B phases after micellization. Actually, this equation directly implies that the concentration of the copolymer chains that are freely distributed within the homopolymer matrix is constant and equal to that at the critical micelle concentration (CMC). As mentioned earlier this is the existing perception in theories discussing the micellization of block copolymers,^{27, 55, 57, 60} but disagrees with the experimental data.

Comparison between Theory and Experiment. The analytical form of the equations derived from this simple thermodynamic model allows the direct calculation of four crucial parameters, which fully characterize the S_nI_n star copolymer micellization process. These are the core radius $R_c \equiv R_A$, the total micellar radius R , the aggregation number Q_m and the unimer concentration ϕ_{uni} . This makes possible the prediction of the micellar characteristics and allows a quantitative comparison with the experimental data.

It was already mentioned that for a series of copolymers like the ones of the present study, where f_A , N and χ are kept constant, the presented theoretical approach results in Q_m that depends only on the number of arms n , actually following a n^{-1} power law, while the radii of the core and of the whole micelle are independent of n and depend only on the length of the A arm of the respective A-B diblock copolymer. In the present case, $f_A = f_{ps} \approx 0.45$ (average volume fraction), $N = 404$, $b = b_{average} = 5.48 \text{ \AA}$ and $\chi = 0.064$ at 25°C .¹⁰¹ By substituting these values in eqs. 2.3.8 and 2.3.10, one gets $Q_m = 242/n$, $R = 15.5 \text{ nm}$ and $R_c = 11.9 \text{ nm}$, which should be compared to the experimental values $Q_m = 224/n$ and $R_c = 11 \text{ nm}$. It is noted that Dynamic Light Scattering in 2wt% blends of S_2I_2 in the PI matrix resulted⁸² in hydrodynamic radii of 16 nm, which is in agreement with the estimation of $R = 15.5 \text{ nm}$. The theoretical results for R_c and Q_m are shown in Figures 2.3.3.2a and 2.3.3.3a, respectively, in comparison to the corresponding experimental results. The agreement between the theoretical and the experimental values is exceptionally good taking into account that no adjustable parameters are used for the comparison.

Surprisingly, a very simple model like this, which is based only on the assumption that there is no homopolymer penetration in the corona of the micelle, succeeds to describe very well the micelle characteristics and their dependence on the macromolecular architecture for this particular series of specimens and their molecular weights. Judging from the fact that the experimental micelle radius is slightly smaller than the theoretical one, we can conclude that this assumption is fairly valid, since possible swelling of the corona

with homopolymer chains would result in larger experimental values. Moreover, the consistency between the dependence of the experimental micellar characteristics on the number of arms n and the predicted trends imply that the junction point does not contribute significantly to the free energy of the micelle, as it was silently assumed within the model.

2.3.5 Concluding Remarks

The macromolecular architecture effect on the micellization and the micellar characteristics of graft Y-shaped copolymers and miktoarm stars added in a low molecular weight polyisoprene matrix has been studied via Small Angle X-ray Scattering and the results have been compared to those obtained for the linear copolymers with the same overall molecular weight and respective compositions.

As far as the I₂S graft copolymers are concerned, for low volume fraction of the polystyrene block, the copolymer is miscible in the polyisoprene homopolymer matrix, whereas micelles are formed as f_{PS} increases ($0.32 \leq f_{PS} \leq 0.82$) and macrophase separation takes place for $f_{PS} = 0.90$, resulting in copolymer-rich weakly ordered domains formed within the polyisoprene matrix.

For both the linear and the graft copolymer micelles the core radius increases with increasing f_{PS} , but this increase is more pronounced for the graft copolymers signifying that the polystyrene blocks in the core are more stretched due to the existence of two polyisoprene arms connected at the same junction point to the polystyrene block; this apparently alters the grafting density at the core-corona interface and favors the curvature. Moreover, the higher stretching allows the better packing of the chains within the core and, thus, higher aggregation numbers are obtained for the graft copolymer micelles. The influence of the macromolecular architecture is demonstrated even more when the micellization of the S₂I graft copolymer is quantitatively compared to its I₂S mirror image. The core radius and the aggregation number increase in the order I₂S < S₂I < IS (for compositionally symmetric copolymers) and the number of polystyrene blocks participating in the core of the S₂I graft copolymers is almost three times that of the I₂S sample, implying that the low molecular weight of the polystyrene block is counterbalanced by the increased number of chains forming the core.

On the other hand, spherical micelles are formed for all the examined values of the functionality n of the S_nI_n stars and the core size is proved to be constant, independent of the number of arms. The aggregation number follows a n^{-1} power law dependence, which is consistent with the constant micelle size.

Although the copolymer concentration in the present measurements are far above the critical micellization concentration, it is found that almost a half of the added copolymer chains exist in the form of unimers homogeneously distributed within the homopolymer matrix and the other half participates in micelles. Moreover, the volume fraction of micelles is independent of n . Thus, the micellar shape, size and structure for the various miktoarm copolymers are proved to be identical to that calculated for the respective linear diblock copolymers, indicating that the micellization does not depend on the macromolecular architecture for the present series of S_nI_n copolymers.

A simple thermodynamic model was developed based on the analysis by Leibler⁵⁷ and Semenov⁵² for diblock copolymers and its extensions for other geometries^{9, 53} or more complicated architectures^{36, 37, 53} in order to predict the micelle characteristics. Despite the assumptions introduced and the simplicity of the model, the calculation succeeds in predicting quite precisely the values of the radii of the core and of the aggregation number and their dependence on the functionality n . According to the analytical expressions that were derived, the A_nB_n miktoarm star copolymers of all n values form micelles of equal size to those formed by the corresponding linear A-B diblock copolymers, depending only on the length of the respective A-B diblocks. The aggregation number and the chemical potential of the A_nB_n copolymers are related to those for the linear diblock case through an n^{-1} and n power law, respectively, indicating that the junction point of the star copolymers, and consequently the polymeric architecture, does not influence the micellization.

2.4 Concentration and Temperature Effects on the Micellization of Linear IS Copolymers

2.4.1 Introduction

It was already mentioned in the Introduction that suitably chosen copolymers are used as compatibilizers in homopolymer blends. However, the micelles that are formed for low copolymer concentrations compete with the interfacial region for copolymer chains. Since the copolymer chains that contribute to micellization do not affect the interfacial activity of the blend,^{53, 102} their efficiency as interfacial agents is decreased and their utility in industrial applications is debatable. Therefore, an important question associated with the micelle formation of block copolymers in homopolymer blends arises, concerning the degree to which additional copolymer chains contribute to the formation of new micelles or to free chains, dissolved as unimers in the homopolymer matrix, above the Critical Micellization Concentration (CMC) and below the Critical Micellization Temperature (CMT). This issue is directly addressing to the overall discussion on the micellization process itself, the way that micelles are formed or dissolved and the changes on the characteristics of the micelles and the micellar blends as the copolymer concentration and the temperature increase, which has been partially overlooked and only superficially studied up to now, despite its scientific significance.

In the last 20 years the micellization of block copolymers in a homopolymer matrix has been thoroughly investigated both theoretically^{27, 57, 59, 60} and experimentally^{61-65, 69} and a theoretical framework that relates the micellar features to the macromolecular characteristics of the copolymer blocks and the matrix material have been derived. The results that are mainly discussed concern the core radius,^{63, 65} the shell thickness,⁶⁹ the aggregation number, the fraction of homopolymer in the core⁶² or the corona,⁶⁵ and the two micellization thresholds, the CMC and the CMT.^{62, 70-72} However, only a few sporadic reports that refer to

the concentration or temperature effect on the micellization process appear in the literature.

From a theoretical point of view, Leibler et al.⁵⁷ studied the dependence of the fraction of copolymers that form micelles on the overall copolymer volume fraction and mentioned that not all added chains form new micelles above an effective CMC, rendering the micellization a non-true phase transition. They estimated that this effect is particularly visible for relatively small incompatibility values χN , while for highly incompatible systems above CMC the volume fraction of free unimers is predicted to be almost stable and equal to the CMC value, just like what happens in the micellization of surfactant molecules. Similar results have been derived by Whitmore and Noolandi,²⁷ who have also calculated the temperature variation of the volume fractions of micelles and unimers in the blends.

Kinning et al.⁶⁵ are the first to report on the existence of free chains in the micellar blends from experimental data. Assuming that the amount of free copolymer chains equals the CMC, they calculated the theoretically predicted invariant and compared it to the experimental SAXS invariant. The deviation between the two was attributed to the existence of extra free chains in the blends and they estimated that the amount of unaggregated copolymer increases beyond the CMC as the copolymer concentration is increased. In a second paper⁶⁶ the same authors compared their results with the theoretical predictions of Leibler et al.⁵⁷ and the extension to their theory by Roe,⁵⁸ and concluded that the theory underestimates the amount of free copolymer dissolved in the homopolymer matrix above CMC. This discrepancy was attributed to a too high value of the interaction energy density used in the calculations, or to small inaccuracies in the model. Similar observations are reported by Major et al.,⁷⁰ who used steady-state fluorescence energy-transfer to study the microphase separation in labeled copolymer / homopolymer blends and they reached the conclusion that above an effective CMC additional block copolymer partitions itself between micelles and the homogeneous matrix phase, although they claim that the effect is small at copolymer concentrations exceeding 1wt%. Finally, Gohr et al.⁶⁹ incorporated a single chain scattering term in the fitting procedure of their small angle neutron

scattering data in order to take into account the effect of the free chain scattering. A nonlinear increase in the unimers concentration was found, which was finally assumed to end in a plateau value, and the authors restricted themselves to the conclusion that in a block copolymer / homopolymer melt the CMC is less well-defined than in a low molecular weight selective solvent.

In this study we aim in a thorough qualitative and quantitative investigation of the micellization process in the blend of a symmetric linear diblock copolymer and a low molecular weight homopolymer matrix. By increasing the copolymer concentration the formation of micelles in the blends is followed using SAXS and the micellar characteristics are derived, as well as the volume fraction of the copolymer chains participating in micelles. Moreover, the dissolution of micelles is examined, as the temperature is increased to reach CMT, since the ability of temperature to trigger the formation or dissolution of block copolymers micelles finds a number of technological applications. Throughout this section, the system under investigation is considered to be a prototype for the study of the micellization process and our study is focused on the way that the relative number of micelles changes upon addition of copolymer chains or upon the increase of the temperature, signifying the formation or dissolution of micelles respectively.

2.4.2 Results and Discussion

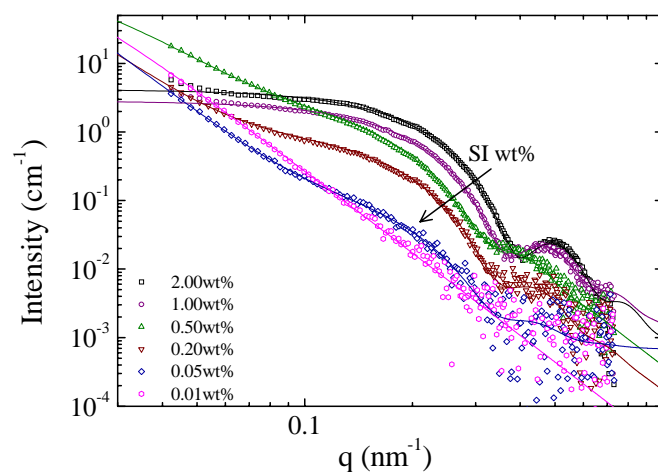


Figure 2.4.1: Small angle X-ray scattering intensity profiles for the various copolymer concentrations of the blends of the symmetric SI copolymer in the PI homopolymer matrix, measured at room temperature. The best fits to the scattering data are designated by solid lines and they were obtained considering the existence of spherical particles and inhomogeneities in the blends.

Figure 2.4.1 shows the SAXS intensity profiles acquired for the various concentrations of the SI in PI blends at room temperature. As expected, the total scattering intensity decreases with decreasing copolymer concentration, while the characteristic features of the scattering by homogeneous spheres are present in almost all patterns. A clear minimum is observed for the higher concentrations under study, namely from 2wt% up to 0.2wt%, which is much less apparent in the data for the 0.05wt% blend and completely vanishes for 0.01wt%, signifying that no micelles are present in the latter blend; the 0.01 wt% blend is, therefore, below CMC. In all cases, the minimum lies in the range $0.3 - 0.4 \text{ nm}^{-1}$ and a slight shift towards lower q values is observed with decreasing concentration, implying that the particle size increases. Despite the absence of higher order minima due to the rather limited q range explored in this experiment, earlier measurements on the 2wt% blend have shown that spherical micelles are formed in the 2 wt% blend.¹⁰³ The formation of spherical micelles is also evident by the intensity plateau in the

low wavevector range, which is well-observed for the specimens with high copolymer concentration.

However, a q -dependent upturn appears at low wavevectors in expense of the plateau when the copolymer concentration is decreased and a gradual transition from the q -independent plateau to a q^4 intensity dependence is observed, which becomes dominant in the scattering patterns of the 0.05wt% and 0.01wt% blends. The origin of this contribution to the scattering could be primarily attributed to aggregates that are present in the blends together with the micelles. Aggregates could result for example from the coalescence of micelles; however, the formation of such aggregates would be doubtful for low concentration blends. On the other hand, one could speculate that the q -dependent contribution to the scattered intensity is related to the scattering from the free copolymer chains that remain dissolved in the blends. In that case, the scattering profile acquired for the 0.01 wt% blend, which should be below CMC, would represent the form factor that arises from the conformation of the PS-block of the free unimers. If the PS blocks of the copolymers exist in the coil state, their scattered intensity should exhibit a q^2 dependence (at high q 's), as predicted by Debye,¹⁰⁴ which is not the case either. Alternatively, since the PS-blocks of the SI copolymers are embedded in the unfavorable PI matrix, it can be anticipated that they are in the collapsed state, i.e., in a form of monomolecular micelles. To our knowledge, there are no experimental data on the scattering from collapsed copolymer blocks; however, one can postulate that they would scatter like spheres of small radius. However, the scattering curves do not exhibit any features that would correspond to the form factor of monomolecular micelles. Their form factor scattering would be found at higher wavevectors than the range covered by our experiments, due to their small size with a plateau at low q 's. Moreover, one can anticipate that the scattered intensity from these monomolecular micelles would be much less intense than that of the polymolecular micelles, so it may be very difficult to observe it experimentally. Therefore, the present data as well as dynamic light scattering data⁸² even at conditions where micelles did not exist (when solvent was still present in copolymer/homopolymer/common solvent systems and micelles had not been

formed) did not show any sign of monomolecular micelles, although other works interpreted their findings by UV spectroscopy,⁷⁷ turbidity¹⁰⁵ or surface tension¹⁰⁶ with the presence of monomolecular micelles in copolymer solutions in selective solvents. Therefore an attempt to relate the upturn of the intensity to the scattering from the free unimers is considered to be rather unreliable. Another possible scenario is that the increasing intensity in the low q range originates from micro-voids embedded in the blends. Despite the fact that the viscous blends were inserted in the capillary tubes by centrifugation in order to prevent such effects, the presence of micro-air bubbles can not be excluded. The emergence of air-bubbles in the blends would result in a Porod-like contribution to the scattering, like that observed here. However, in this case we choose to apply a Debye-Bueche¹⁰⁷ function in order to fit the data, which is a common way to describe the scattering of inhomogeneous systems, such as porous materials, i.e.,

$$I(q) = \frac{8\pi\xi^3(\Delta\rho)^2}{(1 + \xi^2q^2)^2} \quad (2.4.1)$$

where ξ is a correlation length. Apparently a q^4 dependence can be obtained for the scattering intensity for $q\xi > 1$.

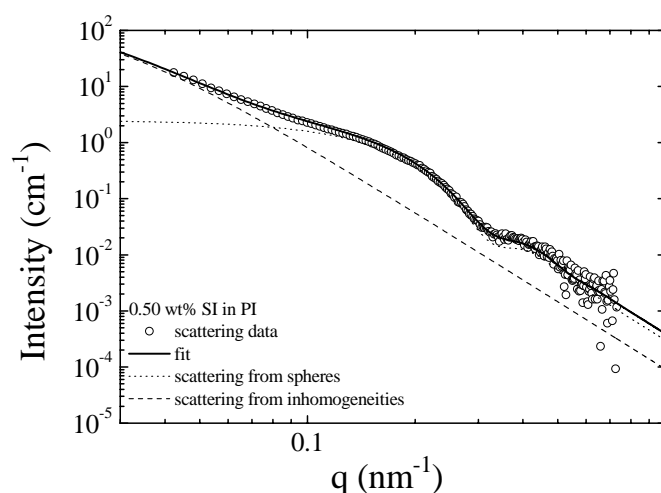


Figure 2.4.2: The scattering intensity profile acquired for the 0.50wt% blend of the SI copolymer within the PI matrix at room temperature. The best fit to the data (solid line) arises from the addition of two contributions; the scattering of the spherical micellar cores (dot line) and the scattering from inhomogeneities embedded in the blends (dash line).

Among the data presented in Figure 2.4.1, the assumption of spherical micelles is sufficient to analyze the curves corresponding only to 2 wt% and 1 wt%, due to the higher intensity scattered by the micelles with respect to the scattering due to the inhomogeneities. For the other curves, the total scattered intensity is assumed to arise from two contributions: the scattering from the spherical micellar cores and that from the inhomogeneities embedded in the blends. Figure 2.4.2 presents the results of the analysis for the 0.5wt% blend. The form factor of spheres fails to fit the whole curve and, thus, the Debye-Bueche function is added, resulting in the best fitting curve, which is in excellent agreement with the experimental data. The simulated contribution of the micellar cores to the total scattered intensity for the various concentrations is shown in Figure 2.4.3. The results presented below are derived solely from the analysis of these scattering curves, following the procedure described in section 2.2.4.

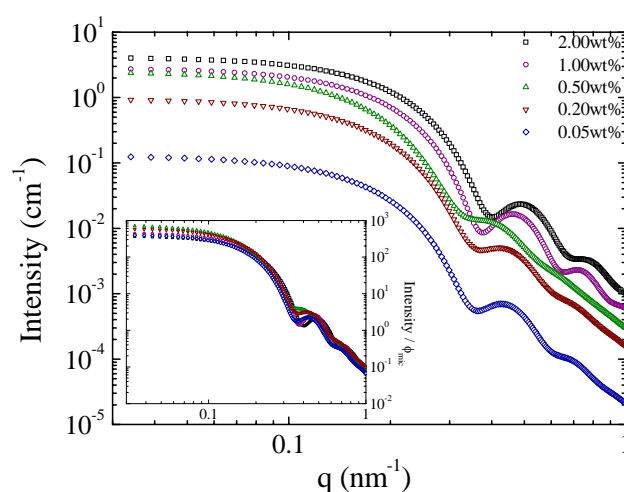


Figure 2.4.3: The simulated scattering intensity of the micellar cores, calculated for the various copolymer concentrations shown in Figure 2.4.1, according to the form factor analysis described in the text. The normalized profiles with respect to the calculated ϕ_{mic} are presented in the inset.

Figure 2.4.4a shows the radii of the polystyrene cores of the micelles formed by the SI copolymer within the PI matrix at room temperature as a function of the copolymer concentration. The slight increase of the radius as the concentration decreases below 0.5wt% is practically minor and, therefore, the radius is considered to be constant and equal to 12.5nm in the concentration

range explored. This finding is consistent with the theoretical predictions^{27, 57} according to which the core radius should be independent of the copolymer concentration and with the data presented by Gohr, et al.⁶⁹ However, Kinning et al.⁶⁵ reported that the core radius increased with increasing concentration up to 30wt% but they implied that this was probably an artifact of the sample preparation method, since the possible causes of this trend were all rejected in their discussion. The error bars in Figure 2.4.4a correspond to the polydispersity in the core radius, which is constant, as well, and about 10% of the radius. The increased error bars for the lowest concentration at which micelles are formed, i.e. at 0.05wt%, is probably due not to an increased polydispersity but to the fact that the minimum of the form factor is partially masked by the scattering from the inhomogeneities and, thus, the fitted polydispersity value is overestimated.

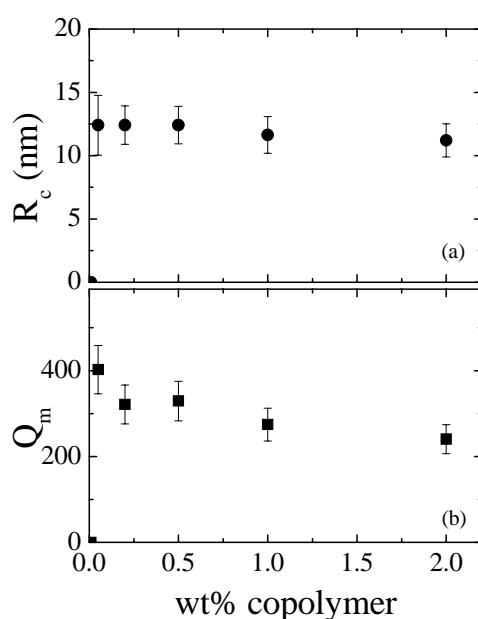


Figure 2.4.4: The copolymer concentration dependence of the micellar core radius, R_c , (a) and the aggregation number, Q_m , (b), at room temperature. The error bars of R_c correspond to the polydispersity values derived from fitting.

Despite the very weak dependence on the copolymer concentration observed in Figure 2.4.4b, the aggregation number, Q_m , is considered to be constant, around 300 chains per micelle, in agreement to what could be speculated from the constant radius. It is noted that the aggregation number values have been

derived from the volume of the scatterers, calculated from the forward scattering intensity, independently of the radius derived from the form factor. Thus, it can be safely derived that the micellar structure does not depend on the concentration.

In order to have a better insight in the effect of the copolymer concentration on the total scattered intensity (Figures 2.4.1 and 2.4.3), Figure 2.4.5 presents the forward scattering intensity from the core of the micelles as derived after the deconvolution of the two contributions. The forward scattering intensity increases continuously over the whole concentration range explored signifying that the micellar volume fraction and number density increase as well with increasing concentration, according to eq. 2.2.7. However the linear increase that is observed till 0.5wt% is followed by a weaker linear dependence, which implies that not all added copolymer chains contribute to the scattering from the micelles and, therefore, not all of them participate in new micelles. The origin and the quantity of the “missing” intensity (or “missing” micelles) that is apparent in the high concentrations will be discussed below.

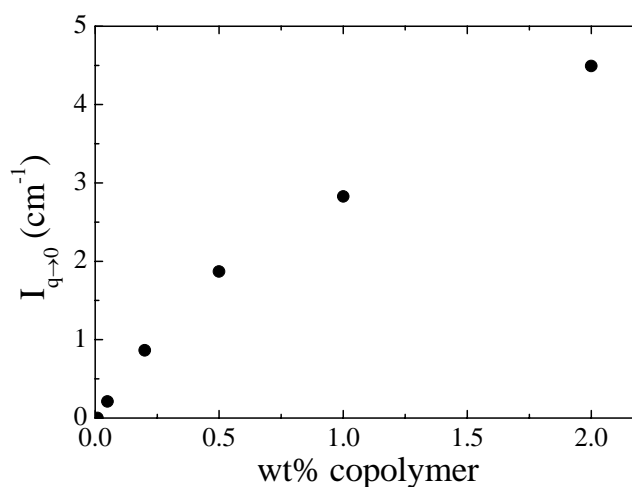


Figure 2.4.5: The variation of the forward scattering intensity arising from the core of the copolymer micelles with respect to the copolymer concentration in the blends.

According to Rigby and Roe,⁶² the linear increase of the forward scattering intensity with respect to the concentration can be utilize for the estimation of the CMC. However, the non-linear trend obtained in the present study complicates the calculations, since the CMC value will depend on the equation used to fit the

data. For instance, by applying a linear fit in the low concentration range the calculated CMC is 0.0018wt%, while a parabolic fit yields 0.0032% and a cubic 0.0088%. Experimentally, the blend with 0.01wt% is already below CMC and, so, it is preferable to claim that the CMC is located in the concentration range below 0.05-0.01wt%, than try to determine the CMC more precisely. The location of CMC in a range of concentrations is also reported by other researchers, both experimentally⁷⁰ and theoretically.⁵⁷

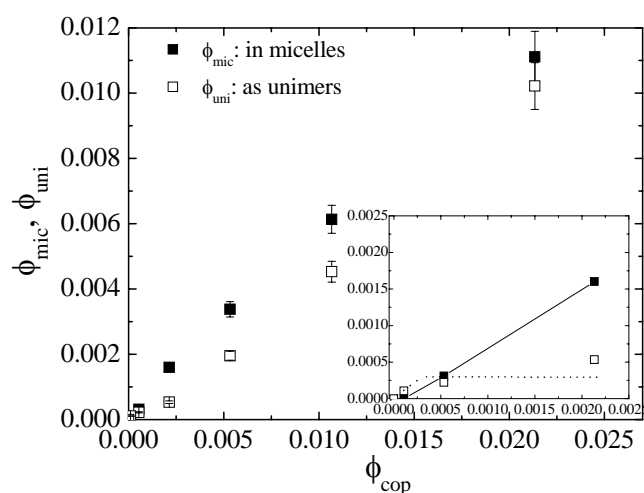


Figure 2.4.6: The volume fraction of copolymer chains participating in micelles formation, ϕ_{mic} , (filled squares) and unimers, ϕ_{uni} , (open squares) as a function of the overall copolymer volume fraction in the blends, ϕ_{cop} , at room temperature. The low ϕ_{cop} range is presented magnified in the inset for clarity.

Applying the methodology proposed in section 2.2.4, the volume fractions of copolymer chains participating in micelles, ϕ_{mic} , and of those dispersed in the matrix, ϕ_{uni} , have been calculated. The results are presented in Figure 2.4.6 as a function of the total copolymer volume fraction in the blends, ϕ , while the fraction of copolymer chains that form micelles, ϕ_{mic}/ϕ , is presented in Figure 2.4.7. Similarly to the forward scattering intensity, above CMC, ϕ_{mic} increases with increasing ϕ in a non-linear way. As shown in the inset, for very low ϕ values there is a finite ϕ_c above which ϕ_{mic} increases linearly with ϕ . This means that ϕ_c corresponds to an effective CMC and all chains that are added above this value

form new micelles. In the same concentration range ϕ_{uni} increases until ϕ_c , since below CMC all copolymer chains are dissolved in the matrix, and then it seems to stabilize around $\phi_{\text{uni}}=0.0003$, which is equivalent to approximately 0.03 wt%. This value is considered to be the CMC for the present system at room temperature. However, a further increase of ϕ above 0.0025 results in an abrupt increase in ϕ_{uni} , simultaneously with a reduced concentration dependence of ϕ_{mic} . It is noted that the validity of the ϕ_{mic} values derived was crosschecked; the simulated scattering curves of the micelles, shown in Figure 2.4.3, had been normalized with respect to the calculated ϕ_{mic} and are presented in the inset of the same plot in order to verify that they coincide very well with each other. The small variations that appear in the low q range are attributed to the minor variations in the radius of the particles, which affect the forward scattering intensity.

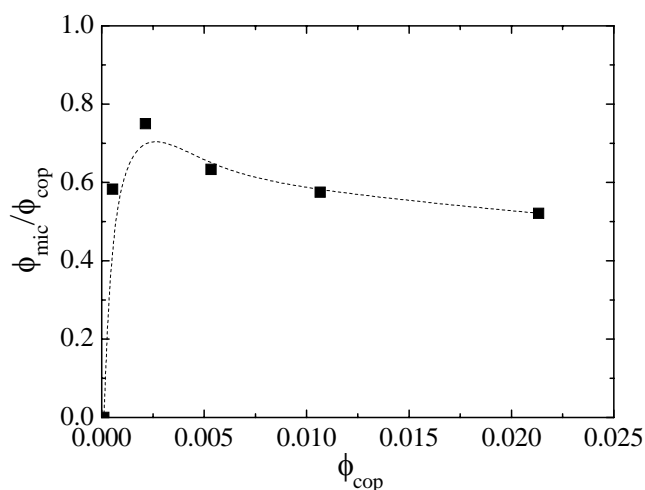


Figure 2.4.7: The fraction of copolymer chains forming micelles at room temperature as a function of the overall copolymer volume fraction in the blends. The dash line serves as guide to the eye.

The experimental findings concerning ϕ_{mic} and ϕ_{uni} in the low concentration range are in good agreement with the curves derived theoretically by Leibler et al.⁵⁷ and Whitmore and Noolandi²⁷ for highly incompatible systems. For relatively small incompatibility values χN they claim that not all added copolymer chains form micelles but some remain free, increasing the entropy of

the surrounding homogeneous mixture. However, the increased ϕ_{uni} derived in the present study for the high concentration region can not be attributed to a weak segregation between PS and PI or to a very high value of the interaction energy density that was used in the theoretical calculations, as it was assumed in an earlier report,⁶⁶ since the abrupt onset of the increase of the fraction of copolymer chains that form micelles, ϕ_{mic}/ϕ , presented in Figure 2.4.7 agrees very well with the respective curves calculated in the two theories^{27, 57} for high incompatibility values χN . Again, in the high concentration range ϕ_{mic}/ϕ deviates from the theoretical predictions and decreases after exhibiting a weak maximum around $\phi = 0.002$, until it reaches a plateau value close to $\phi_{\text{mic}}/\phi = 0.5$.

In order to study the dissolution of micelles, temperature dependent measurements have been carried out, starting from room temperature and increasing the temperature to 160°C. The samples were equilibrated at each temperature for at least 10min before the measurement. In order to verify that the samples had reached the equilibrium state and test the stability of the micelles, a different sample has been heated up to 120°C, it was left at this high temperature for 6 hours and then it was measured again. The scattering profiles acquired before and after the 6 hours interval were identical. The SAXS data acquired for the 0.2 wt% blend of the SI copolymer within the PI matrix are shown in Figure 2.4.8. The total scattered intensity remained almost unaffected for a wide range of temperatures and, thus, most of the curves are presented shifted vertically by the factor shown in the Figure for clarity. Between room temperature and 80°C the scattering curves are identical and, therefore, only the curves corresponding to 40°C and 80°C are included. A slight decrease of the scattered intensity is observed at 100°C, which become much more noticeable at 120°C. At this temperature the minimum of the first oscillation in the form factor is less apparent than before and it almost vanishes at 140°C. However, it was found that the data could still be fitted with a micellar form factor. However, they are completely dissolved at 160°C. The fitting of the SAXS data has been accomplished by assuming once more that the total scattering intensity arises from the sum of two contributions, the scattering from the core of the micelles and that

from the inhomogeneities embedded in the blends, as discussed earlier. The fitted curves are designated in Figure 2.4.8 by solid lines. For the curve that corresponds to 160°C the Debye-Bueche equation was sufficient to fit the data, confirming the lack of micelles in the blend.

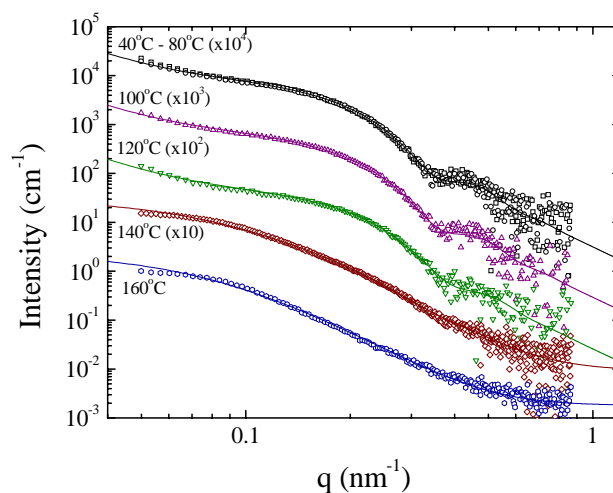


Figure 2.4.8: The SAXS intensity profiles of the 0.2wt% blends of the SI diblock copolymer in the PI matrix measured at various temperatures and the corresponding best fits (solid lines). The scattering curves have been vertically shifted for clarity, while those acquired in the temperature range between room temperature and 80°C are identical and, thus, only the curves that correspond to 40°C and 80°C are shown.

The fitting results concerning the core radius, R_c , and the aggregation number, Q_m , are presented in Figure 2.4.9. The error bars in the radius correspond to the polydispersity in the core radius. Both R_c and Q_m are constant almost until the dissolution temperature, implying that the temperature does not affect the micellar characteristics. This finding is contradictory to the results reported by Rigby and Roe⁶² according to which the radius increases with increasing temperature due to the swelling of the core with homopolymer. As also recognized by Kinning, et al.,⁶⁴ part of this discrepancy may be attributed to the very low molecular weights of the copolymers employed by Rigby and Roe.⁶² However, the quality of the data acquired in the present study renders the results obtained to be indisputable, and, additionally, the penetration of homopolymer in the core has been discarded both experimentally^{65, 66} and theoretically.^{27, 57}

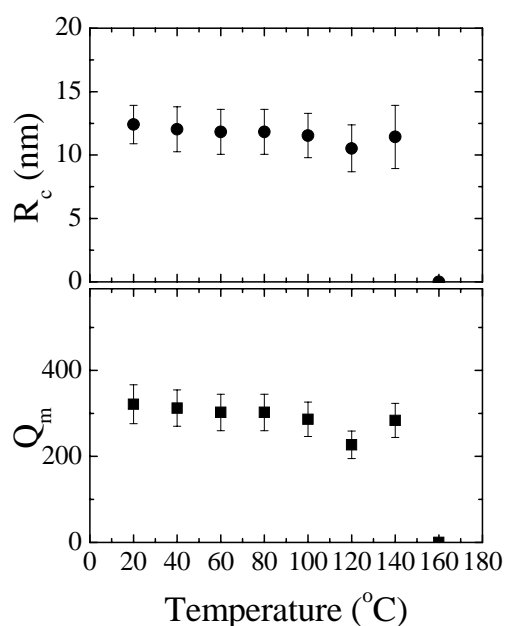


Figure 2.4.9: The temperature dependence of the core radius, R_c , and the aggregation number, Q_m , of the micelles formed in the 0.2wt% blend of the SI diblock copolymer in the PI matrix. The error bars of R_c correspond to the polydispersity values estimated from the form factor analysis fitting.

The volume fractions of the copolymers that form micelles, ϕ_{mic} , and those that are dispersed in the blends, ϕ_{uni} , have been calculated via the analysis of the intensity that is scattered from the micelles and the results obtained concerning the temperature effect on two samples with different copolymer concentration are shown in Figure 2.4.10. For both blends, ϕ_{mic} and ϕ_{uni} are constant for a wide range of temperatures and then ϕ_{mic} starts to gradually decrease, signifying the decrease of the number of micelles and the increase of the free unimers in the blend. Similar trends have been derived theoretically.^{27, 57, 66} The increase of ϕ_{uni} with increasing temperature is expected and is attributed to the dispersion of the free chains in the blend. These became available due to the dissolution of micelles since the incompatibility parameter, χN , decreases with temperature increase. The onset of the decrease of ϕ_{mic} depends on the copolymer concentration and it is found in a lower temperature for the low concentration blend, implying that the micelles dissolve more easily when the copolymer concentration is closer to the

CMC. Similarly, the CMT, which corresponds to the temperature at which $\phi_{\text{mic}} = 0$, is lower for the 0.2 wt% blend and is estimated to be around 150°C, while for the 0.5 wt% blend it exceeds 160°C; the extrapolation of the decreasing ϕ_{mic} yields a CMT value for the 0.5 wt% blend of about 180°C. It is interesting to note that the temperature interval for the dissolution of all the micelles is around 60°C for both concentrations, despite the fact that almost half micelles are present in the 0.2 wt% with respect to the 0.5 wt% blend, or that the fraction of copolymer chains participating in micelles, ϕ_{mic}/ϕ , is larger in the 0.2 wt% blend. Consequently, the dissolution of the micelles depends on the interaction parameter χ and is strongly controlled by the copolymer concentration in the blend as well.

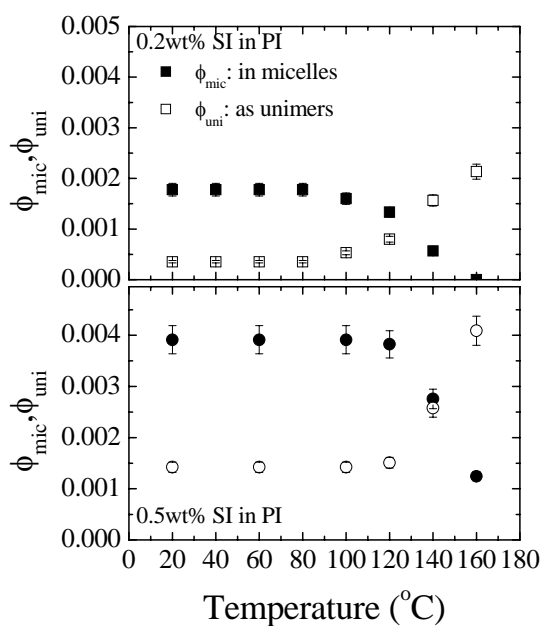


Figure 2.4.10: The variation of the volume fraction of copolymer chains participating in micelles, ϕ_{mic} , (filled symbols) and unimers, ϕ_{uni} , (open symbols) with temperature, for the 0.2wt% and 0.5wt% blends of the SI diblock copolymer in the PI matrix.

2.4.3 Concluding Remarks

The micellization characteristics of the blend of a symmetric diblock copolymer within a selective homopolymer matrix have been investigated with respect to the copolymer concentration and the temperature. The core radius and the aggregation number are found to be independent of the two variables, suggesting that only the macromolecular characteristics of the copolymer¹⁰³ and the matrix¹⁰⁸ control the structure of the micelles. Just above CMC, the volume fraction of micelles is increasing linearly with increasing concentration, while that of the copolymer chains that remain free in the blend is almost constant, in agreement with the theoretical predictions. However a further increase of the copolymer concentration results in an increase in ϕ_{uni} and a decrease in the rate of increase of ϕ_{mic} with ϕ implying that not all added copolymer chains participate in the formation of new micelles.

As far as the temperature effect is concerned, the dissolution of micelles is manifested by a gradual decrease of the volume fraction of micelles in the blend with increasing temperature up to CMT, in agreement with theoretical predictions. The onset of the decrease in ϕ_{mic} as well as the dissolution temperature depends strongly on the copolymer concentration in the blend where the micelles dissolve more easily when the concentration of the blend is closer to the CMC.

2.5 The Role of the Homopolymer Molecular Weight in the Micellization of Linear IS Copolymers

2.5.1 Introduction

In this section, the investigation on the micellization of block copolymers in homopolymer matrices is completed by studying the role of the homopolymer matrix. Although the experimental findings of Selb et al.⁶¹ and Kinning et al.⁶⁵ agree that the core radius increases with increasing the molecular weight, they both restrict themselves to a phenomenological description of the thermodynamic reasons that should govern the micellization; Selb et al.⁶¹ attribute this trend to the increased incompatibility between the matrix and the core-forming block, while Kinning et al.⁶⁵ imply that the homopolymer penetration in the corona determines the structure of the micelles due to entropic reasons. In a following paper⁶⁶ the same authors compare their results with the predictions of the theory of micelle formation by Leibler, Orland and Wheeler,⁵⁷ as modified by Roe⁵⁸ and conclude that the dependence of the core radius on the homopolymer molecular weight is seen to be larger than that predicted theoretically. The experimental core radii are smaller than expected, with the difference between the two decreasing with increasing the homopolymer molecular weight, probably due to the omission of the entropy of localizing the block copolymer segment joints to the interface between the micelle core and the corona.⁶⁶ In another paper Kinning et al.⁶⁴ show that transitions in micelles shape can occur by increasing the homopolymer molecular weight beyond a certain value, resulting in blends having nonspherical (cylindrical or lamellar) micelles. Finally, two works dedicated to the corona structure are presented by Gohr et al.,^{69, 109} that deal with the dynamics of the micelle for strong and negligible swelling of the corona by the matrix chains¹⁰⁹ and the density profile of the corona under strong swelling⁶⁹ respectively.

As already cited, Leibler, Orland and Wheeler⁵⁷ were the first to propose a thermodynamic model for the formation of spherical micelles in block copolymer / homopolymer blends. They considered the total free energy of the system

allowing a fraction of the copolymer chains to remain free and the homopolymer chains to penetrate within the micellar corona, and predicted that the average number of free chains and the micellar characteristics are determined by a delicate balance between the internal energy of the micelles and the entropy of mixing of micelles, free copolymer chains and the homopolymer matrix. A few years later, Leibler^{31, 32} presented a simplified methodology for the calculation of the chemical potential of a copolymer chain within a micelle for the case of long homopolymer chains that do not penetrate the corona of the micelles. Whitmore and Noolandi²⁷ extended the theory of Leibler, Orland and Wheeler to take into account the localization of the copolymer joints to the interfacial region of the micelle, the possible penetration of homopolymer into the micellar core and the copolymer composition, and they derived the dependence of the micelle characteristics on those of the copolymer and the homopolymer. Similar corrections have been applied by Roe,⁵⁸ who compared the theoretical predictions to the experimental results of Rigby and Roe^{62, 63} and found a good semi-quantitative agreement. The possibility of the formation of cylindrical micelles was examined by Mayes and Olvera de la Cruz,⁵⁹ who derived the free energy expressions for spherical and cylindrical micelles and discussed the conditions that favor the cylindrical over the spherical geometry. Finally, Monte Carlo simulations and self-consistent field theory were utilized recently to calculate the CMC and the size distribution and shape characteristics of diblock copolymer micelles formed within a homopolymer matrix.⁶⁰

Although most of the theories cited above provide analytical expressions for the free energy of the micellar blend, facilitating the comparison between experimental results and theoretical predictions, only the work of Kinning et al.⁶⁶ actually make use of them. In the present study, two theoretical models have been applied for the estimation of the micellar structure when diblock copolymers are added in a homopolymer matrix; the simplified by Leibler^{31, 32} that assumes that the homopolymer is excluded from the corona (Dry Corona model) and the generalized one⁵⁷ that allows the homopolymer to penetrate within the corona (Wet Corona model), as it was presented by Mayes and Olvera de la Cruz.⁵⁹ Thus, the comparison between the theoretical predictions and the experimental results

obtained from SAXS measurements for the polystyrene-b-polyisoprene micelles that are formed in polyisoprene matrices of various molecular weights enlightens the role of the homopolymer penetration in the corona and renders the homopolymer molecular weight a control parameter for the tailoring of the micellar characteristics. The effect of grafting the copolymer with a second corona-forming block (I_2S) is examined as well, always with respect to the corona structure and the micellar characteristics. In order to compare the experimental results with the theoretical ones, the Wet Corona model for linear copolymers has been extended to describe the micellization of AB_2 copolymers in a B homopolymer and is presented herein. For the case that the homopolymer does not penetrate within the corona of the graft copolymer micelles the extension of the model of Leibler^{31, 32} presented by Retsos et al.⁵³ has been applied. Finally, the transition from the micro-phase separated micellar phase to the macro-phase separation with increasing the homopolymer molecular weight is demonstrated for the case when graft copolymers with high polystyrene content are added in a high molecular weight matrix.

2.5.2 Theoretical Models

The Dry Corona model for the micellization of AB diblock copolymers or AB₂ graft copolymers within a B homopolymer

The free energy of a copolymer chain within a micelle can be calculated following the methodology that Leibler^{31, 32} presented for the case of linear AB diblock copolymers blended with long B homopolymer chains that do not penetrate within the corona of the micelles (Dry Corona). Briefly, Leibler^{31, 32} considered disperse spherical micelles of total radius R , with a core made of the A blocks and a corona made of the B blocks, with Q_m being the aggregation number. The free energy of the micelle is represented by a sum of three contributions:

$$F_{mic} = A\gamma_0 + F_{core} + F_{corona} \quad (2.5.1)$$

where $A = 4\pi R_A^2$ is the interfacial area and γ_0 is the A/B interfacial tension. The core free energy, F_{core} , is associated with the nonuniform stretching of the A block arising from constraining the copolymer A-B junction to a narrow interface and it was calculated self consistently by Semenov.¹⁰⁰ The free energy of the corona, F_{corona} , is calculated assuming that all the free ends of the B blocks reach the radius R and that there is no penetration of the homopolymer chains into the corona, taking into account the nonuniform deformation of the B blocks due to the spherical geometry. The core radius R_A and the total radius R are derived by assuming incompressibility of the core and the whole micelle respectively. The equilibrium value of Q_m is obtained by minimizing the free energy per copolymer chain, F_{mic}/Q_m , with respect to Q_m , $\partial(F_{mic}/Q_m)/\partial Q_m = 0$, which yields the analytical form⁵³

$$Q_{m_{min}} = (3/2)^{1/2} (4\pi/3) \chi^{1/2} N f_A^{2/3} \left(1.74 f_A^{-1/3} - 1\right)^{-1} \quad (2.5.2)$$

More recently, Retsos et al.⁵³ adopted the methodology of Leibler^{31, 32} and presented its extension to describe the micellization of AB₂ graft copolymers when added to a B homopolymer. In this case the micelles are formed with a core

made up of the tooth A blocks and a corona consisting of the two B blocks and, for this, the free energy terms for the core and the corona should be modified properly. The equilibrium value of Q_m is provided analytically:⁵³

$$Q_{m_{\min}} = 5.1302 \chi^{1/2} N f_A^{2/3} (4.74 f_A^{-1/3} - 4)^{-1} \quad (2.5.3)$$

Therefore, the core radius for both the AB and AB₂ copolymer micelles is derived from the incompressibility condition:

$$R_A = \left(\frac{3}{4\pi} Q_{m_{\min}} f_A N b^3 \right)^{1/3} \quad (2.5.4a)$$

and for the two cases of AB and AB₂ micelles within a B homopolymer are given by

$$R_{A,AB} = \left(\frac{3}{2} \right)^{1/6} N^{2/3} b \chi^{1/6} f_A^{5/6} (1.74 f_A^{-1/3} - 1)^{-1/3} \quad (2.5.4.b)$$

$$R_{A,AB_2} = 1.225^{1/3} N^{2/3} b \chi^{1/6} f_A^{5/6} (4.74 f_A^{-1/3} - 4)^{-1/3} \quad (2.5.4.c)$$

It is reminded that the extension of this methodology for the prediction of the micellar characteristics of A_nB_n miktoarm star copolymers has been derived by the author and is presented explicitly in Section 2.3.4.

In the equations above, χ is the Flory interaction parameter, N and f_A are the copolymer degree of polymerization and composition respectively, and b is the statistical segment length. Apparently, in the Dry Corona model, the micellar characteristics are predicted to be independent of the homopolymer degree of polymerization, N_h .

The Wet Corona model for the micellization of AB diblock copolymers within a B homopolymer

When the homopolymer chains are quite short compared to the corona forming B block, one has to take into account that only a fraction, η , of B monomers in the corona belongs to copolymer chains, while the rest $1-\eta$ belongs to the homopolymer chains that penetrate within the micellar corona,⁵⁷ similarly to what happens in a wet polymer brush. Thus, the free energy of mixing homopolymer chains and B blocks of copolymer chains inside the corona, F_m ,

should be incorporated in the free energy of micelles,⁵⁷ along with the interfacial energy, $A\gamma_0$, and the contribution of the deformation of the copolymer chains,¹¹⁰ F_d , which in the Dry Corona model is represented by the terms F_{core} and F_{corona} . The decrease in entropy due to the localization of the A-B joint of the copolymer at the A/B interface, F_j , should be also included in the free energy of a micelle^{27, 59} and, thus, eq. 1 is modified to⁵⁹

$$F_{\text{mic}} = A\gamma_0 + F_j + F_m + F_d \quad (2.5.5)$$

with F_j , F_m and F_d being⁵⁹

$$F_j = kTQ_m \ln\left(\frac{R^3 - R_A^3}{3R_A^2 b}\right) \quad (2.5.6)$$

$$F_m = \frac{4\pi}{3b^2} (R^3 - R_A^3) kT \left\{ \frac{\eta}{N_B} \ln \eta + \frac{(1-\eta)}{N_h} \ln(1-\eta) \right\} \quad (2.5.7)$$

$$F_d = kTQ_m \left\{ \frac{3}{2} \frac{R_B^2}{N(1-f_A)b^2} + \frac{\pi^2 N(1-f_A)b^2}{6R_B^2} + \frac{3}{2} \frac{R_A^2}{Nf_A b^2} + \frac{\pi^2 Nf_A b^2}{6R_A^2} - 6.29 \right\} \quad (2.5.8)$$

Assuming incompressibility, one can apply eq. 2.5.4 for the core radius and the equation^{57, 59}

$$4\pi(R^3 - R_A^3)\eta/3 = Q_m(1-f_A)Nb^3 \quad (2.5.9)$$

for the total micelle radius, respectively. For a detailed description of the Wet Corona model the reader is directed to the original papers by Leibler, Orland & Wheeler⁵⁷, Mayes & Olvera de la Cruz⁵⁹ and Whitmore & Noolandi.²⁷

In order to estimate the equilibrium values of Q_m and η , the methodology of Leibler^{31, 32} presented above is applied. The micellar free energy per copolymer chain, F_{mic}/Q_m , is minimized with respect to the two variable parameters, Q_m and η , by equating the partial derivatives $\partial(F_{\text{mic}}/Q_m)/\partial Q_m$ and $\partial(F_{\text{mic}}/Q_m)/\partial \eta$ to zero. The system of equations that is obtained can be solved only numerically and the values $Q_{m_{\text{min}}}$ and η_{min} that are obtained allow for the calculation of the radii R_A and R from eq. 2.5.4 and 2.5.9 respectively.

The Wet Corona model for the micellization of AB₂ graft copolymers within a B homopolymer

When an AB₂ graft copolymer is added to a B homopolymer, the existence of two B blocks per copolymer chain alters the free energy terms that are associated with the micellar corona. Suppose that Q_m copolymer chains participate in each micelle and that each chain comprises $N = N_A + 2(N_B/2)$ segments, with the composition being again $f_A = N_A/N$. The interfacial energy term is independent of the macromolecular architecture and will remain as it is; however, F_j , F_m and F_d should be modified.

The joint localization energy represents the change in free energy due to the confinement of the end segment of each corona forming B block to the A/B interface, which is regarded to be equivalent to squeezing the volume available for the localization of the end segment, from the corona volume to that of a finite shell around the interface. Since the number of B blocks in the corona is now $2Q_m$, the joint localization energy becomes

$$F_j = kT2Q_m \ln\left(\frac{R^3 - R_A^3}{3R_A^2b}\right) \quad (2.5.10)$$

The free energy of mixing, F_m , depends only on the volume fraction and the degree of polymerization of the components of the blend that forms the micellar corona. The volume fraction η is a variable parameter and, thus, one has to use the proper degree of polymerization. Thus, eq.7 now becomes

$$F_m = \frac{4\pi}{3b^2}(R^3 - R_A^3)kT\left\{\frac{\eta}{N_B/2}\ln\eta + \frac{(1-\eta)}{N_h}\ln(1-\eta)\right\} \quad (2.5.11)$$

Finally, the deformation energy term, F_d , consists of two terms for the elastic energy¹¹⁰ of the core chains and two for that of the corona chains. The terms that refer to the core will remain as in eq. 2.5.8, while the corona terms have to be modified in order to account for the existence of two B blocks each with half the number of the B segments. Consequently,

$$F_d = kT\left\{2Q_m \frac{3}{2} \frac{R_B^2}{(N_B/2)b^2} + 2Q_m \frac{\pi^2(N_B/2)b^2}{6R_B^2} + Q_m \frac{3}{2} \frac{R_A^2}{Nf_A b^2} + Q_m \frac{\pi^2 Nf_A b^2}{6R_A^2} - 6.29Q_m\right\} \quad (2.5.12)$$

The equilibrium values $Q_{m_{\min}}$ and η_{\min} are derived by minimizing the micellar free energy per copolymer chain, F_{mic} / Q_{mic} , as described previously.

2.5.3 Results and Discussion

The scattering intensity profiles acquired for the 2wt% blends of the symmetric linear copolymer IS-4 ($f_{\text{PS}} = 0.49$) in the various PI matrices are presented in Figure 2.5.1. The profiles that were recorded for the blends of the other linear copolymers exhibit similar shapes and, therefore, they are not shown. The characteristic features of the form factor of spherical particles are apparent in the profiles, namely a plateau in the low q range and oscillations with well pronounced minima, the position of which agrees with the condition fulfilled by the minima corresponding to the form factor of a homogeneous sphere. Thus, one can safely derive that spherical micelles are formed in all cases.^{103, 111}

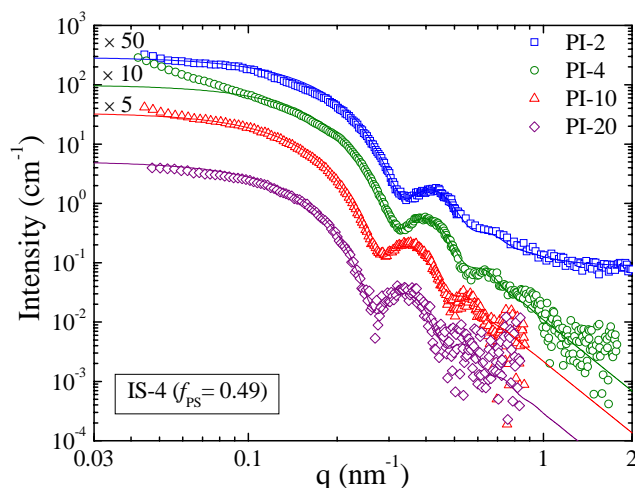


Figure 2.5.1: Small angle X-ray scattering intensity profiles of the 2wt% blends of the linear IS diblock copolymer with $f_{\text{PS}} = 0.49$ in the various PI matrices, acquired at room temperature. The corresponding best fitting curves are designated by solid lines while the profiles have been shifted vertically by the noted amounts for clarity.

The position of the first minimum shifts towards lower q values as the molecular weight of the homopolymer matrix is increased, implying that the core radius increased. This trend was further verified by the form factor analysis. The best fit curves are shown by solid lines in Fig. 2.5.1, while the fitting results concerning the core radius, R_c , are presented in Figure 2.5.2, as a function of the homopolymer degree of polymerization, N_h . The error bars correspond to the

polydispersity in the core radius, which is around 10%. For all three compositions under study, R_c increases with increasing N_h , in agreement with earlier observations.^{65, 66} However, the data apparently approach a kind of a plateau for high N_h ; although this is the first time that such a plateau is observed experimentally, the theoretical predictions of Mayes and Olvera de la Cruz⁵⁹ had implied that R_c would approach a constant value versus N_h when the homopolymer molecular weight becomes comparable to that of the corona forming block.

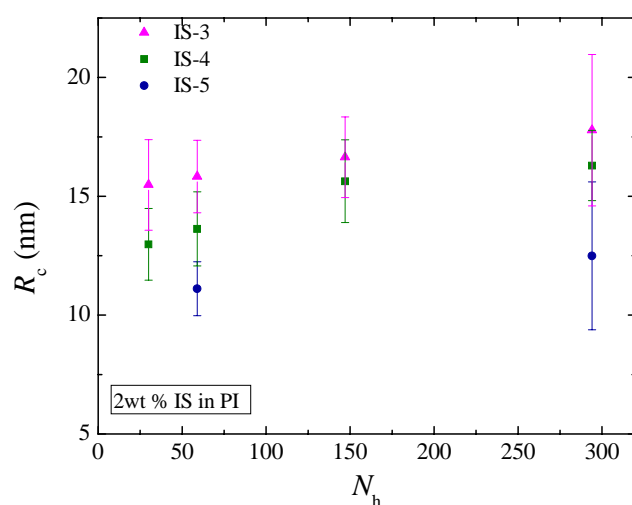


Figure 2.5.2: The core radii, R_c , of the micelles formed within the 2wt% blends of the various linear SI copolymers as a function of the degree of polymerization of the PI matrix, N_h . The error bars correspond to the polydispersity, as estimated from the form factor analysis.

When N_h increases, the entropy of mixing homopolymer chains and PI copolymer blocks in the corona decreases. The homopolymer chains are progressively expelled from the corona while the PI blocks become more compressed, similarly to the case of polymer brushes. However, adding more copolymers to the micelle would relax the PI block compression and would be favorable.⁵⁷ Thus, the aggregation number increases and, consequently, the core radius increases as well. When the homopolymer is completely expelled from the corona (dry corona), the free energy of mixing becomes zero and the micellar

characteristics do not depend on N_h resulting in the plateau that was observed experimentally.

The copolymer composition effect is shown in Fig. 2.5.2, as well. Although only two points are available for the $f_{PS} = 0.29$ sample, one can securely hint that increasing f_{PS} results in a lower rate of increase of R_c with N_h . This trend can be explained in the context of the wet brush behavior of the micellar corona. Since all IS copolymers have similar overall molecular weights, increasing f_{PS} is equivalent to decreasing the length of the PI block and, therefore, the mixing with the homopolymer chains becomes less favored. Therefore, the dry brush limit is approached at lower N_h bringing the plateau in R_c within the investigated range of N_h .

As described above, the behavior shown in Fig. 2.5.2 reflects the transition between the wet and the dry corona state. In order to verify this theoretically, the boundary between the two states, namely the dry brush limit that is defined for polymer brushes,¹¹² could be used and the divergence of each sample from that limit could be examined. However, the dry brush limit is derived only for planar brushes and, thus, it would be valid only in case the core radius was big enough to consider the corona as a planar brush. The author is not aware of any published work that reports the dry brush limit for spherical brushes¹¹³ and thus it was preferable to apply a different approach and compare the experimental results with the predictions of two theoretical models, the Dry Corona model that is valid when the micellar corona is formed solely by the copolymer blocks and the Wet Corona model that allows for the homopolymer to penetrate within the corona.

The theoretically predicted core radii (open symbols) are presented in Figure 2.5.3 along with the experimental values (solid symbols), as a function of the composition, for all the homopolymer matrices. The Dry Corona predictions (open stars) are independent of N_h and for this only one value is calculated for each sample. Although this model predicts well that R_c increases with increasing f_{PS} ,^{61, 65, 111} the model significantly overestimates the radii. However, the agreement is fairly good when the experimental results are compared to those of the Wet Corona model, which predicts much smaller micelles than the Dry Corona one, but still overestimates R_c with the deviations being larger for the IS copolymers

with the shorter PI blocks. This observation along with the excellent agreement obtained for the $f_{PS} = 0.29$ sample imply that the Wet Corona model is more effective the more wet the corona is. Moreover, Figure 2.5.3 shows that, as the homopolymer molecular weight increases, the experimental R_c and that predicted by the Wet Corona model increase in a similar way. A tendency to approach the Dry Corona limiting predictions is also evident and agrees with the suggestion presented earlier that the transition between the wet and the dry corona state is reflected in the present data.

Apparently, the penetration of homopolymer in the core can alter significantly the micellar characteristics and notably reduce R_c . It is noted that the increase in the radius is about 25% and 15% for the micelles formed by the copolymers with $f_{PS} = 0.49$ and $f_{PS} = 0.65$ respectively, which is an important change. The ability to change the micellar size, and therefore the aggregation number, is in principle highly desired and, in the present study, the efficiency of the homopolymer molecular weight to tailor the size of the micelles in a controlled way is demonstrated, along with the ability to apply the existing theories in order to successfully predict the micellar characteristics.

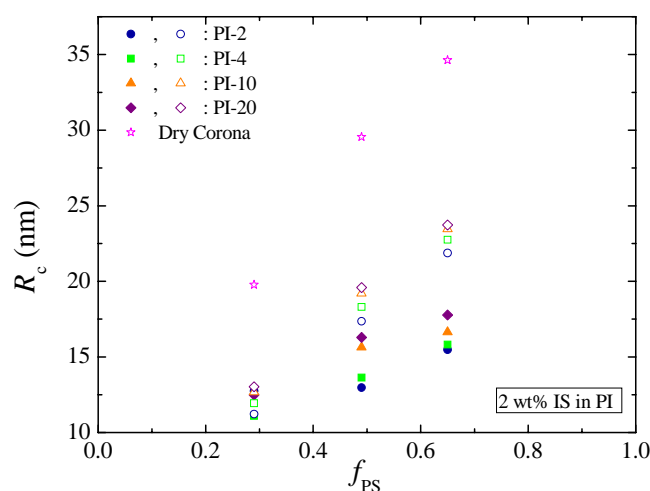
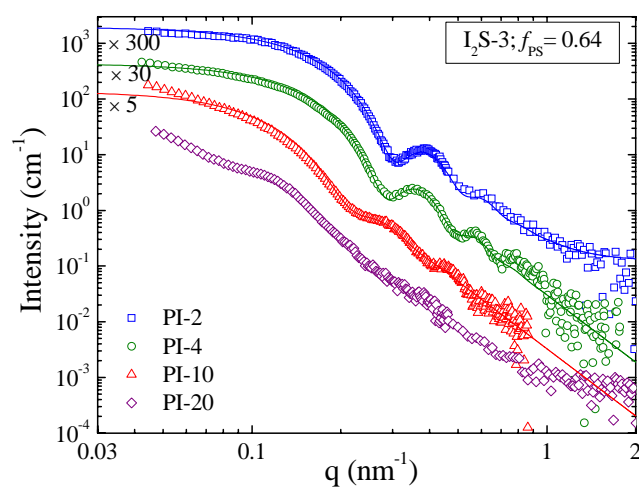
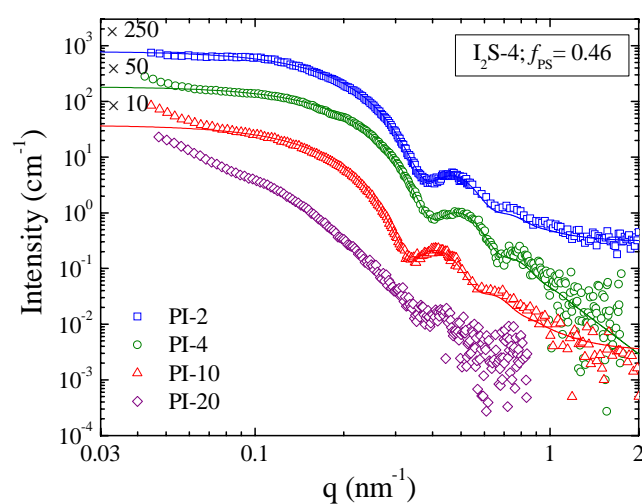


Figure 2.5.3: Experimental core radii R_c (solid symbols) of the micelles formed in the 2wt% blends of the linear IS copolymers in the various PI matrices, as a function of the copolymer composition, f_{PS} , in comparison to the values predicted theoretically by the Wet Corona Model (open symbols). The predictions of the Dry Corona model are designated by open stars and are independent of the matrix molecular weight.

The effect of macromolecular architecture on the behavior is investigated next. Graft copolymers are utilized that possess two corona forming blocks; it is anticipated that this would affect the homopolymer penetration within the corona, since one can assume a higher grafting density at the core/corona interface, forcing the PI blocks to stretch more and hindering the wetting of the corona. Figure 2.5.4 shows the scattering intensity profiles acquired for the 2 wt% blends of four of the I₂S graft copolymer. The patterns acquired for the I₂S-4 ($f_{PS} = 0.46$) graft are presented in Fig. 2.5.4a. Spherical micelles are formed when the copolymer is added to the PI-2, PI-4 and PI-10 matrices, while this is not the case for the PI-20 blend; a broad peak is observed in the latter case around 0.11 nm^{-1} , close enough to the theoretically calculated value for the scattering of the disordered diblock. Thus, macrophase separation between the homopolymer and the copolymer is most probable to have occurred. This finding disagrees with that reported by Kinning, et al.,^{64, 65} where a further increase in the homopolymer molecular weight resulted in transitions in the micellar shape, from spherical to cylindrical and to lamellar. A similar behavior is apparent in the SAXS profiles that were recorded for the blends of the I₂S-3 ($f_{PS} = 0.64$) graft; indeed Fig. 2.5.4b shows the characteristic features of the form factor of spherical micelles for the three PI's with lower molecular weight and the broad peak at around 0.12 nm^{-1} for the PI-20. However, when the copolymer composition is increased to $f_{PS} = 0.82$ (I₂S-2), both the profiles acquired for the 10k and 20k blends, shown in Fig. 2.5.4c, exhibit a broad peak, at 0.1 and 0.14 nm^{-1} respectively, signifying that macro-phase separation takes place at lower homopolymer molecular weight (the patterns for the blends with PI-2 and PI-4 show the oscillations characteristic of spherical micelles). This trend is even more pronounced in the data acquired for the I₂S-1 ($f_{PS} = 0.90$) graft copolymer, presented in Fig. 2.5.4d. None of the blends of this graft contains micelles and a peak is observed in all profiles. The peak position shifts towards higher wavevector values as the homopolymer molecular weight increases, which is indicative of a decreasing spacing between the structural components: 54 nm for PI-2, 52 nm for PI-4, 32 nm for PI-10 and 25.5 nm for PI-20. In an earlier work,¹¹¹ the profile acquired for the blend with PI-4 was

investigated in detail and the author concluded that copolymer-rich domains, containing weakly ordered cylinders formed by the polyisoprene block swollen with polyisoprene homopolymer in a polystyrene-block matrix, are present within the homopolymer matrix. Since the patterns presented here possess similar features, one could generalize this result and claim that the peaks shift due to decreased spacing between the cylinders within the copolymer-rich domains caused by an increased exclusion of the PI homopolymer from the copolymer-rich domains. In other words, as the homopolymer molecular weight increases, the phases that are present in the blends become more pure and the approach to order within the copolymer-rich domains becomes more evident.



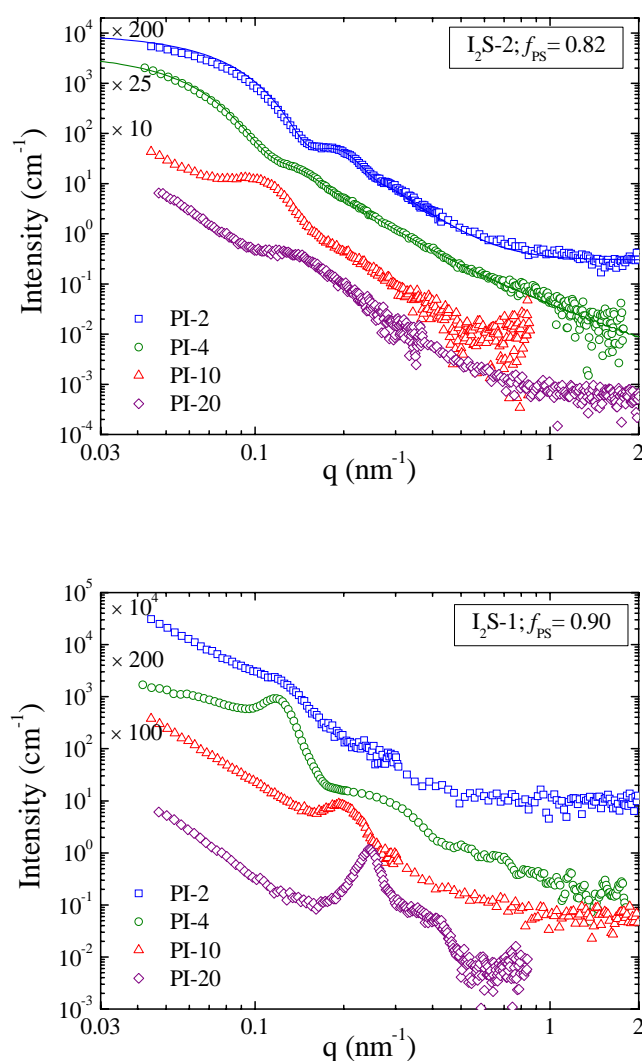


Figure 2.5.4: Small angle X-ray scattering intensity profiles of the 2wt% blends of the I₂S graft copolymers within the various PI matrices, acquired at room temperature: (a) I₂S-4 with $f_{PS} = 0.46$; (b) I₂S-3 with $f_{PS} = 0.64$; (c) I₂S-2 with $f_{PS} = 0.82$; (d) I₂S-1 with $f_{PS} = 0.90$. The corresponding best fit curves for the blends with spherical micelles are shown by solid lines while the profiles have been shifted vertically by the noted amounts for clarity.

The results of the analysis concerning the core radius of the micelles formed by the graft copolymer blends with respect to N_h are presented in Figure 2.5.5. For all three copolymer compositions, R_c increases with increasing the homopolymer molecular weight, in accordance to what was suggested before for the linear copolymers. However, a tendency towards a constant value (plateau) is not observed in these systems whereas a rapid increase of the radius with N_h is observed with increasing the polystyrene composition f_{PS} , until macrophase

separation takes place. This finding apparently disagrees with the predictions of the Wet Corona model for the linear copolymer micelles, since the corona forming blocks are shorter for the grafts and, so, the systems should be closer to the dry brush limit. However, grafting the copolymer with a second PI block increases the grafting density of the corona brush, favors the curvature induced on the two sides of the core/corona interface and drives the PS blocks to stretch more, increasing abruptly R_c .¹¹¹ This contribution should be additive to the effect of the homopolymer molecular weight on the core radius, as discussed for the linear copolymer micelles, and, thus, one is lead to the trend shown in Fig. 2.5.5 until macro-phase separation eventually occurs.

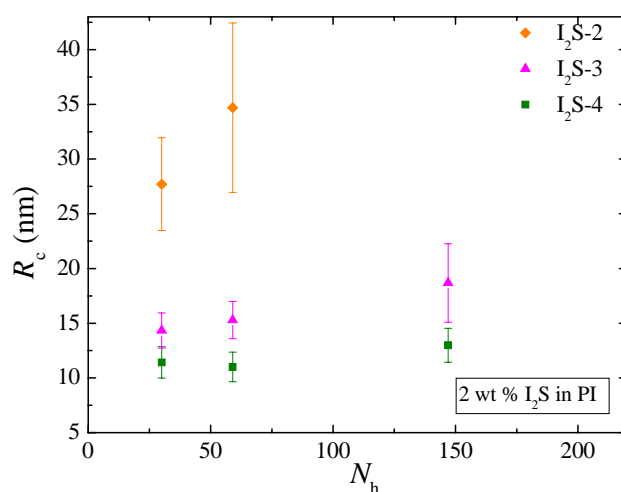


Figure 2.5.5: The core radii, R_c , of the micelles formed within the 2wt% blends of the various I_2S grafts, as a function of the homopolymer degree of polymerization, N_h . The error bars correspond to the estimated polydispersity.

Figure 2.5.6 displays the R_c values that were theoretically predicted by the Wet and the Dry Corona models in comparison to the experimental data. Once more, the Dry Corona model can qualitatively describe well the experimental findings, but not quantitatively, apart from the graft copolymer with $f_{PS} = 0.82$ for which the agreement is very satisfactory. For the rest of the samples the Wet Corona model works really well, both qualitatively and quantitatively, and the trend to approach the predictions of the Dry Corona model with increasing N_h is evident.

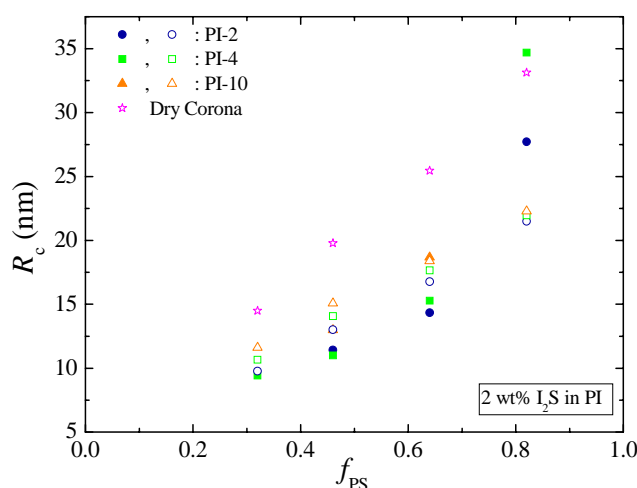


Figure 2.5.6: Experimental core radii R_c (solid symbols) of the micelles formed in the 2wt% blends of the graft I_2S copolymers in the various PI matrices, as a function of the copolymer composition, f_{PS} , in comparison to the values predicted theoretically by the Wet Corona Model (open symbols). The predictions of the Dry Corona model are designated by open stars and are independent of the matrix molecular weight.

Since the predictions of the Wet Corona model are in good agreement with the experimental values for the core radius, one could assume that it can predict reasonably correct the volume fraction of the copolymer chains in the corona, η , as well. It is noted that η and the aggregation number, Q_m , are the two parameters that are directly estimated from the Wet Corona model by minimizing the total free energy of the micelle per copolymer chain. Figure 2.5.7 presents the average volume fraction of homopolymer penetrating within the corona, $1-\eta$, as a function of the homopolymer molecular weight for both the linear and the graft copolymer micelles and for all compositions. Less homopolymer resides within the micellar corona as N_h increases, verifying the transition from the wet to the dry corona state, and a non-zero plateau value becomes evident for high N_h , in agreement with the plateau that is observed for the radius. The estimated absolute values of $1-\eta$ seem quite large. However, they can be reasonable considering that this is the mean value of a parameter that exhibits a radial distribution profile; the density of the copolymer chains is close to one in the proximity of the core/corona interface while it decreases along the corona following a r^α

dependence with $1 \leq \alpha \leq 4/3$ (the limits correspond to the dense and the swollen brush, respectively^{95, 114}) and vanishes at the external boundary of the micelle. Finally, the homopolymer penetration is estimated to be less for the graft copolymer micelles than the linear ones, signifying that the corona of the grafts is indeed more dry.

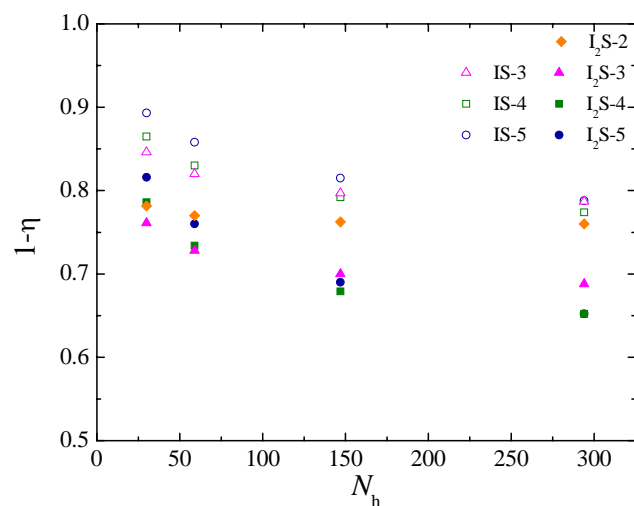


Figure 2.5.7: The average volume fraction of the homopolymer that penetrates within the corona of the IS and I₂S micelles as a function of the degree of polymerization of the PI matrix, N_h . The values presented have been derived theoretically by applying the Wet Corona model.

2.5.4 Concluding Remarks

The effect of the homopolymer penetration on the micellar characteristics is investigated in block copolymer / homopolymer blends, with respect to the molecular weight of the matrix and the macromolecular architecture, namely the grafting of the copolymer with a second corona-forming block and the copolymer composition f_{ps} . The SAXS measurements revealed that spherical micelles are formed for all the blends of the linear copolymer in the various matrices. The core radius increases with increasing N_h until it reaches a plateau value, which is related to the expulsion of the homopolymer chains from the micellar corona and signifies the transition from the wet to the dry state of the corona. For constant overall molecular weight of the copolymer, increasing f_{ps} is equivalent to shifting the system closer to the dry brush limit. Moreover, the extra stretching of the core blocks that is induced from the grafting has as consequence the continuous increase of R_c . Graft copolymers with very high polystyrene volume fractions lead to macrophase separation between copolymer-rich and homopolymer-rich regions as the homopolymer molecular weight increased. The copolymer-rich phase approaches the ordered regime as the homopolymer is expelled further at high N_h .

The experimental results for both the linear and the graft copolymer micelles have been compared to the theoretical predictions of two models: the Dry Corona model, which assumes that the micellar corona is formed solely by the copolymer blocks and the Wet Corona model that allows for homopolymer chains to penetrate within the corona. The later has been modified by the authors for the case of graft copolymer micelles. It is found that both theories predict correctly the trends that are obtained experimentally; however, only the Wet Corona model succeeds in quantitatively predicting the behavior. Thus, the influence of the matrix characteristics on the micellar properties is confirmed both experimentally and theoretically and the efficiency of the homopolymer molecular weight to tailor the size of the micelles in a controlled way is demonstrated.

2.6 References and Notes

1. Paul, D. R.; Bucknall, C. B., *Polymer Blends Set: Formulation and performance*. John Wiley & Sons: New York, 2000.
2. Koning, C.; van Duin, M.; Pagnouille, C.; Jerome, R. *Progress in Polymer Science* **1998**, 23, (4), 707-757.
3. Fayt, R.; Jerome, R.; Teyssie, P. *Journal of Polymer Science Part C-Polymer Letters* **1986**, 24, (1), 25-28.
4. Green, P. F.; Russell, T. P. *Macromolecules* **1991**, 24, (10), 2931-2935.
5. Dai, K. H.; Kramer, E. J. *Journal of Polymer Science Part B-Polymer Physics* **1994**, 32, (11), 1943-1950.
6. Reynolds, B. J.; Ruegg, M. L.; Mates, T. E.; Radke, C. J.; Balsara, N. P. *Macromolecules* **2005**, 38, (9), 3872-3882.
7. Lefebvre, M. D.; Dettmer, C. M.; McSwain, R. L.; Xu, C.; Davila, J. R.; Composto, R. J.; Nguyen, S. T.; Shull, K. R. *Macromolecules* **2005**, 38, (25), 10494-10502.
8. Eastwood, E.; Viswanathan, S.; O'Brien, C. P.; Kumar, D.; Dadmun, M. D. *Polymer* **2005**, 46, (12), 3957-3970.
9. Shull, K. R.; Kramer, E. J. *Macromolecules* **1990**, 23, (22), 4769-4779.
10. Russell, T. P.; Anastasiadis, S. H.; Menelle, A.; Felcher, G. P.; Satija, S. K. *Macromolecules* **1991**, 24, (7), 1575-1582.
11. Dai, K. H.; Norton, L. J.; Kramer, E. J. *Macromolecules* **1994**, 27, (7), 1949-1956.
12. Anastasiadis, S. H.; Gancarz, I.; Koberstein, J. T. *Macromolecules* **1989**, 22, (3), 1449-1453.
13. Wagner, M.; Wolf, B. A. *Polymer* **1993**, 34, (7), 1460-1464.
14. Jorzik, U.; Wagner, M.; Wolf, B. A., In *Prog. Colloid Polym. Sci.*, 1996; Vol. 101, p 170.
15. Jorzik, U.; Wolf, B. A. *Macromolecules* **1997**, 30, (16), 4713-4718.
16. Zhu, Y. Q.; Gido, S. P.; Moshakou, M.; Iatrou, H.; Hadjichristidis, N.; Park, S.; Chang, T. *Macromolecules* **2003**, 36, (15), 5719-5724.
17. Cho, D. M.; Hu, W. C.; Koberstein, J. T.; Lingelser, J. P.; Gallot, Y. *Macromolecules* **2000**, 33, (14), 5245-5251.
18. Chang, K.; Macosko, C. W.; Morse, D. C. *Macromolecules* **2007**, 40, (10), 3819-3830.
19. Sundararaj, U.; Macosko, C. W. *Macromolecules* **1995**, 28, (8), 2647-2657.
20. Ramic, A. J.; Stehlin, J. C.; Hudson, S. D.; Jamieson, A. M.; Manas-Zloczower, I. *Macromolecules* **2000**, 33, (2), 371-374.
21. Van Puyvelde, P.; Velankar, S.; Moldenaers, P. *Current Opinion in Colloid & Interface Science* **2001**, 6, (5-6), 457-463.
22. Lyu, S.; Jones, T. D.; Bates, F. S.; Macosko, C. W. *Macromolecules* **2002**, 35, (20), 7845-7855.
23. Russell, T. P.; Menelle, A.; Hamilton, W. A.; Smith, G. S.; Satija, S. K.; Majkrzak, C. F. *Macromolecules* **1991**, 24, (20), 5721-5726.
24. Creton, C.; Kramer, E. J.; Hadziioannou, G. *Macromolecules* **1991**, 24, (8), 1846-1853.

25. Brown, H. R.; Char, K.; Deline, V. R.; Green, P. F. *Macromolecules* **1993**, 26, (16), 4155-4163.
26. Dai, C. A.; Jandt, K. D.; Iyengar, D. R.; Slack, N. L.; Dai, K. H.; Davidson, W. B.; Kramer, E. J.; Hui, C. Y. *Macromolecules* **1997**, 30, (3), 549-560.
27. Whitmore, M. D.; Noolandi, J. *Macromolecules* **1985**, 18, (4), 657-665.
28. Duke, T. A. J. Ph.D. Dissertation. University of Cambridge, 1989.
29. Fischel, L. B.; Theodorou, D. N. *Journal of the Chemical Society-Faraday Transactions* **1995**, 91, (16), 2381-2402.
30. Werner, A.; Schmid, F.; Binder, K.; Muller, M. *Macromolecules* **1996**, 29, (25), 8241-8248.
31. Leibler, L. *Makromolekulare Chemie-Macromolecular Symposia* **1988**, 16, 1-17.
32. Leibler, L. *Physica A* **1991**, 172, (1-2), 258-268.
33. Israels, R.; Jasnow, D.; Balazs, A. C.; Guo, L.; Krausch, G.; Sokolov, J.; Rafailovich, M. *Journal of Chemical Physics* **1995**, 102, (20), 8149-8157.
34. Gersappe, D.; Harm, P. K.; Irvine, D.; Balazs, A. C. *Macromolecules* **1994**, 27, (3), 720-724.
35. Gersappe, D.; Balazs, A. C. *Physical Review E* **1995**, 52, (5), 5061-5064.
36. Lyatskaya, Y.; Balazs, A. C. *Macromolecules* **1996**, 29, (23), 7581-7587.
37. Lyatskaya, Y.; Gersappe, D.; Balazs, A. C. *Macromolecules* **1995**, 28, (18), 6278-6283.
38. Russell, T. P.; Mayes, A. M.; Deline, V. R.; Chung, T. C. *Macromolecules* **1992**, 25, (21), 5783-5789.
39. Brown, H. R.; Krappe, U.; Stadler, R. *Macromolecules* **1996**, 29, (20), 6582-6588.
40. Cigana, P.; Favis, B. D. *Polymer* **1998**, 39, (15), 3373-3378.
41. Dadmun, M. *Macromolecules* **1996**, 29, (11), 3868-3874.
42. Dadmun, M. D. *Macromolecules* **2000**, 33, (24), 9122-9125.
43. Eastwood, E. A.; Dadmun, M. D. *Macromolecules* **2002**, 35, (13), 5069-5077.
44. Dai, C. A.; Dair, B. J.; Dai, K. H.; Ober, C. K.; Kramer, E. J.; Hui, C. Y.; Jelinski, L. W. *Physical Review Letters* **1994**, 73, (18), 2472-2475.
45. Kulasekere, R.; Kaiser, H.; Anknor, J. F.; Russell, T. P.; Brown, H. R.; Hawker, C. J.; Mayes, A. M. *Macromolecules* **1996**, 29, (16), 5493-5496.
46. Stammer, A.; Wolf, B. A. *Macromolecular Rapid Communications* **1998**, 19, (2), 123-126.
47. Benkoski, J. J.; Fredrickson, G. H.; Kramer, E. J. *Journal of Polymer Science Part B-Polymer Physics* **2001**, 39, (20), 2363-2377.
48. Shull, K. R. *Macromolecules* **2002**, 35, (22), 8631-8639.
49. Vilgis, T. A.; Noolandi, J. *Makromolekulare Chemie-Macromolecular Symposia* **1988**, 16, 225-234.
50. Vilgis, T. A.; Noolandi, J. *Macromolecules* **1990**, 23, (11), 2941-2947.
51. Shull, K. R.; Winey, K. I.; Thomas, E. L.; Kramer, E. J. *Macromolecules* **1991**, 24, (10), 2748-2751.
52. Semenov, A. N. *Macromolecules* **1992**, 25, (19), 4967-4977.
53. Retsos, H.; Margiolaki, I.; Messaritaki, A.; Anastasiadis, S. H. *Macromolecules* **2001**, 34, (15), 5295-5305.
54. Adedeji, A.; Lyu, S.; Macosko, C. W. *Macromolecules* **2001**, 34, (25), 8663-8668.

55. Chang, K. H.; Morse, D. C. *Macromolecules* **2006**, 39, (22), 7746-7756.
56. Welge, I.; Wolf, B. A. *Polymer* **2001**, 42, (8), 3467-3473.
57. Leibler, L.; Orland, H.; Wheeler, J. C. *Journal of Chemical Physics* **1983**, 79, (7), 3550-3557.
58. Roe, R. J. *Macromolecules* **1986**, 19, (3), 728-731.
59. Mayes, A. M.; Delacruz, M. O. *Macromolecules* **1988**, 21, (8), 2543-2547.
60. Cavallo, A.; Muller, M.; Binder, K. *Macromolecules* **2006**, 39, (26), 9539-9550.
61. Selb, J.; Marie, P.; Rameau, A.; Duplessix, R.; Gallot, Y. *Polymer Bulletin* **1983**, 10, (9-10), 444-451.
62. Rigby, D.; Roe, R. J. *Macromolecules* **1984**, 17, (9), 1778-1785.
63. Rigby, D.; Roe, R. J. *Macromolecules* **1986**, 19, (3), 721-728.
64. Kinning, D. J.; Winey, K. I.; Thomas, E. L. *Macromolecules* **1988**, 21, (12), 3502-3506.
65. Kinning, D. J.; Thomas, E. L.; Fetters, L. J. *Journal of Chemical Physics* **1989**, 90, (10), 5806-5825.
66. Kinning, D. J.; Thomas, E. L.; Fetters, L. J. *Macromolecules* **1991**, 24, (13), 3893-3900.
67. Gohr, K.; Pakula, T.; Tsutsumi, K.; Scharl, W. *Macromolecules* **1999**, 32, (21), 7156-7165.
68. Scharl, W. *Macromolecular Chemistry and Physics* **1999**, 200, (3), 481-500.
69. Gohr, K.; Scharl, W.; Willner, L.; Pyckhout-Hintzen, W. *Macromolecules* **2002**, 35, (24), 9110-9116.
70. Major, M. D.; Torkelson, J. M.; Brearley, A. M. *Macromolecules* **1990**, 23, (6), 1711-1717.
71. Wong, C. L. H.; Kim, J.; Roth, C. B.; Torkelson, J. M. *Macromolecules* **2007**, 40, (16), 5631-5633.
72. Sandoval, R. W.; Williams, D. E.; Kim, J.; Roth, C. B.; Torkelson, J. M. *Journal of Polymer Science Part B-Polymer Physics* **2008**, 46, (24), 2672-2682.
73. Pochan, D. J.; Gido, S. P.; Pispas, S.; Mays, J. W.; Ryan, A. J.; Fairclough, J. P. A.; Hamley, I. W.; Terrill, N. J. *Macromolecules* **1996**, 29, (15), 5091-5098.
74. Iatrou, H.; Hadjichristidis, N. *Macromolecules* **1992**, 25, (18), 4649-4651.
75. Iatrou, H.; Siakalikioulafa, E.; Hadjichristidis, N.; Roovers, J.; Mays, J. *Journal of Polymer Science Part B-Polymer Physics* **1995**, 33, (13), 1925-1932.
76. Pochan, D. J.; Gido, S. P.; Pispas, S.; Mays, J. W. *Macromolecules* **1996**, 29, (15), 5099-5105.
77. Yang, L. Z.; Gido, S. P.; Mays, J. W.; Pispas, S.; Hadjichristidis, N. *Macromolecules* **2001**, 34, (12), 4235-4243.
78. Anastasiadis, S. H.; Chrissopoulou, K.; Fytas, G.; Fleischer, G.; Pispas, S.; Pitsikalis, M.; Mays, J. W.; Hadjichristidis, N. *Macromolecules* **1997**, 30, (8), 2445-2453.
79. Chrissopoulou, K.; Harville, S.; Anastasiadis, S. H.; Fytas, G.; Mays, J. W.; Hadjichristidis, N. *Journal of Polymer Science Part B-Polymer Physics* **1999**, 37, (24), 3385-3391.
80. Pispas, S.; Hadjichristidis, N.; Potemkin, I.; Khokhlov, A. *Macromolecules* **2000**, 33, (5), 1741-1746.
81. Hadjichristidis, N.; Iatrou, H.; Pispas, S.; Pitsikalis, M. *Journal of Polymer Science Part a-Polymer Chemistry* **2000**, 38, (18), 3211-3234.

82. Karagianni, K.; Gioulaki, A.; Chrissopoulou, K.; Anastasiadis, S. H. *in preparation* **2009**.
83. Borsboom, M.; Bras, W.; Cerjak, I.; Detollenaere, D.; van Loon, D. G.; Goedtkindt, P.; Konijnenburg, M.; Lassing, P.; Levine, Y. K.; Munneke, B.; Oversluizen, M.; van Tol, R.; Vlieg, E. *Journal of Synchrotron Radiation* **1998**, 5, 518-520.
84. Bras, W.; Dolbnya, I. P.; Detollenaere, D.; van Tol, R.; Malfois, M.; Greaves, G. N.; Ryan, A. J.; Heeley, E. *Journal of Applied Crystallography* **2003**, 36, 791-794.
85. Gabriel, A.; Dauvergne, F. *Nuclear Instruments & Methods in Physics Research* **1982**, 201, (1), 223-224.
86. Bliss, N.; Bordas, J.; Fell, B. D.; Harris, N. W.; Helsby, W. I.; Mant, G. R.; Smith, W.; Townsandrews, E. *Review of Scientific Instruments* **1995**, 66, (2), 1311-1313.
87. Richardson, M. J.; Savill, N. G. *Polymer* **1977**, 18, (1), 3-9.
88. Sotiriou, K.; Nannou, A.; Velis, G.; Pispas, S. *Macromolecules* **2002**, 35, (10), 4106-4112.
89. Voulgaris, D.; Tsitsilianis, C.; Grayer, V.; Esselink, F. J.; Hadziioannou, G. *Polymer* **1999**, 40, (21), 5879-5889.
90. Pispas, S.; Poulos, Y.; Hadjichristidis, N. *Macromolecules* **1998**, 31, (13), 4177-4181.
91. Mountrichas, G.; Mpiri, M.; Pispas, S. *Macromolecules* **2005**, 38, (3), 940-947.
92. Iatrou, H.; Willner, L.; Hadjichristidis, N.; Halperin, A.; Richter, D. *Macromolecules* **1996**, 29, (2), 581-591.
93. Pispas, S.; Hadjichristidis, N.; Mays, J. W. *Macromolecules* **1996**, 29, (23), 7378-7385.
94. Gohy, J. F., Block copolymer micelles. In *Block Copolymers II*, 2005; Vol. 190, pp 65-136.
95. Forster, S.; Burger, C. *Macromolecules* **1998**, 31, (3), 879-891.
96. Jones, R. A. L., *Soft Condensed Matter*. Oxford University Press: Oxford, 2002.
97. Pavlopoulou, E.; Portale, G.; Iatrou, H.; Hadjichristidis, N.; Anastasiadis, S. H. *to be submitted* **2009**.
98. Helfand, E.; Tagami, Y. *Journal of Polymer Science Part B-Polymer Letters* **1971**, 9, (10), 741-&.
99. Helfand, E.; Tagami, Y. *Journal of Chemical Physics* **1972**, 57, (4), 1812-&.
100. Semenov, A. N. *Zhurnal Eksperimentalnoi I Teoreticheskoi Fiziki* **1985**, 88, (4), 1242-1256.
101. Jian, T.; Anastasiadis, S. H.; Fytas, G.; Adachi, K.; Kotaka, T. *Macromolecules* **1993**, 26, (17), 4706-4711.
102. Macosko, C. W.; Guegan, P.; Khandpur, A. K.; Nakayama, A.; Marechal, P.; Inoue, T. *Macromolecules* **1996**, 29, (17), 5590-5598.
103. Pavlopoulou, E.; Anastasiadis, S. H.; Iatrou, H.; Moshakou, M.; Hadjichristidis, N.; Portale, G.; Bras, W. *Macromolecules* **2009**, in press.
104. Debye, P. *The Journal of Physical and Colloid Chemistry* **1947**, 51, (1), 18-32.
105. Gouanve, F.; Phuong-Nguyen, H.; Hamida, Z. F.; Delmas, G. *Colloid and Polymer Science* **2005**, 283, (9), 994-1006.

106. Kelarakis, A.; Tang, T.; Havredaki, V.; Viras, K.; Hamley, I. W. *Journal of Colloid and Interface Science* **2008**, 320, (1), 70-73.
107. Debye, P.; Bueche, A. M. *Journal of Applied Physics* **1949**, 20, (6), 518-525.
108. Pavlopoulou, E.; Portale, G.; Pispas, S.; Hadjichristidis, N.; Anastasiadis, S. H. *to be submitted* **2009**.
109. Gohr, K.; Scharl, W. *Macromolecules* **2000**, 33, (6), 2129-2135.
110. de Gennes, P. G. *Macromolecules* **1980**, 13, (5), 1069-1075.
111. Pavlopoulou, E.; Portale, G.; Pispas, S.; Hadjichristidis, N.; Anastasiadis, S. H. *to be submitted* **2009**.
112. Aubouy, M.; Fredrickson, G. H.; Pincus, P.; Raphael, E. *Macromolecules* **1995**, 28, (8), 2979-2981.
113. Wang, X.; Foltz, V. J.; Rackaitis, M.; Böhm, G. G. A. *Polymer* **2008**, 49, (26), 5683-5691.
114. Daoud, M.; Cotton, J. P. *Journal De Physique* **1982**, 43, (3), 531-538.

3 Impregnation of pH-Responsive Polymeric Matrices with Metal Nanoparticles

3.1 Introduction

The properties of colloidal metal nanoparticles, which are determined by their particle size, shape and internal structure, are in general greatly different from those of their bulk counterparts and allow a variety of applications in many areas of modern technology. In particular, the enormous surface to volume ratio of nanoscale particles is an attractive and promising feature for their use in catalysis as well as in optical devices, nanoelectronics and superparamagnetic or ferromagnetic materials.¹⁻⁵ The significant energetic costs associated with their large surface area, however, typically necessitate their effective stabilization, which would reduce the interfacial energy and prevent their agglomeration.

In general, two different approaches have been utilized for the incorporation of nanoparticles within polymeric nanostructures. One uses preformed nanoparticles and takes advantage of their cooperative self-organization within the domains of, e.g., ordered block copolymers.^{6, 7} The second approach involves the in situ synthesis of the nanoparticles within the soft matter nanostructures. Functional polymeric materials, i.e., block copolymers,^{8, 9} dendrimers¹⁰ and polymer microgels¹¹ have attracted particular attention as nanoscopic reaction vessels for growing inorganic metal nanocrystals, whereas reverse micelles formed by anionic surfactants in organic media^{12, 13} have been utilized as well. The use of (co)polymers allows potential control of the nanoparticle characteristics and properties by manipulating the polymer molecular structure, size and composition, whereas it permits utilization of both organic and aqueous dispersing media.

Similarly to surfactants, amphiphilic block copolymers tend to self-assemble in selective solvents and form micelles with a solvent-insoluble core. Characterization of the structures formed by the block copolymers in solution is necessary because their morphology can influence the properties of the hybrids

with the metallic nanoparticles. Early micellization and nanoparticle synthesis studies examined the effectiveness of various copolymer systems as nanoparticle matrices in organic solvents.^{14, 15} More recently, a number of studies have focused on the use of water as the medium for these syntheses.¹⁶⁻¹⁹ Water has significant environmental and cost advantages with respect to organic solvents and is an optimum medium for catalytic reactions of hydrophilic substrates. Furthermore, stable polymer nanostructures in aqueous solutions have potential applications in drug delivery, biomolecule separation, etc.^{20, 21}

Two main types of block copolymers are used for micelle formation in aqueous media; amphiphilic^{22, 23} and double-hydrophilic²⁴⁻²⁷ block copolymers. Amphiphilic block copolymers typically compose of a permanently hydrophobic, water insoluble block that associates in aqueous solution and a hydrophilic block that forms the micellar corona. The direct dissolution of amphiphilic block copolymers in water is problematic, in particular for systems comprising hydrophobic blocks of high glass transition temperature, which require the temporary use of an organic co-solvent for the preparation of well-defined micelles. After the removal of the organic solvent by dialysis, the micelles formed in such copolymer systems comprise glassy cores and are, thus, kinetically frozen.²⁸ Double hydrophilic diblocks, on the other hand, comprise two different hydrophilic blocks, one of which undergoes physical and/or chemical transformations in aqueous solution and becomes hydrophobic, while the other remains soluble in water. Thus, micelles are formed in these systems by a simple change in the solution conditions, i.e., pH, temperature and/or salt concentration.^{26, 27, 29} The main advantage of these copolymers is that micellization is an almost fully-reversible process. The formation of micelles with varying pH is particularly advantageous when a completely hydrophobic core is needed.^{24, 26} Such copolymers comprise a pH-sensitive block which undergoes a transition from hydrophilic to hydrophobic as the solution pH is changed, and forms the micelle core, while the second block is hydrophilic and forms the corona of the micelle. One class of such copolymers comprise a water soluble poly(ethylene oxide) or poly(methoxy hexa(ethylene glycol) methacrylate) block and a pH-sensitive tertiary amine block like poly(2(4)-vinyl pyridine) or poly(2-

(diethylamino)ethyl methacrylate). These diblocks form unimers at low pH values, when the tertiary amine block is protonated and soluble in aqueous solution, and micelles at pH values higher than the pK_a of the respective weak acid, when the tertiary amine groups become deprotonated and insoluble in water.^{18, 30} Herein, poly(methoxy hexa(ethylene glycol) methacrylate)-block-poly(2-(diethylamino)ethyl methacrylate), PHEGMA-b-PDEA, diblock copolymers are investigated.

Responsive microgels are particularly attractive for use in biomedical and biotechnological applications such as protein absorption, drug delivery and immobilization of biomolecules in the development of sensors, in membrane filtering, while they can also be employed as microscopic reactors for the synthesis of inorganic nanoparticles.³¹⁻³³ These are lightly cross-linked latex particles of submicrometer dimensions that become highly swollen under certain conditions in response to external stimuli. Both thermo- and pH-responsive microgels have been reported in the literature.^{34, 35} Temperature-sensitive microgels are usually based on poly(*N*-isopropylacrylamide) (PNIPAM). Their thermosensitive properties are due to the lower critical solution temperature of PNIPAM in aqueous solution. pH-responsive microgels comprise either acidic or basic monomer units and have been used for the preparation of microgel-metal hybrid materials. The synthesis involves two general strategies: in the first preformed inorganic particles are loaded in the microgels, while, in the second, the nanoparticles are grown within the microgels. The former method suffers low metal loadings, nanoparticle aggregation and no control over their growth and size. These problems can be overcome by the synthesis of nanoparticles in the presence of the polymeric stabilizer. However, so far metal loadings have not exceeded 20% due to the incorporation of a low fraction of functional monomer that can bind the metal compound, within the microgel particles. Herein, pH-sensitive microgels based on poly(2-(diethylamino)ethyl methacrylate), PDEA, are used as matrices for the formation of nanoparticles at high metal loadings.

In the present study pH-responsive double-hydrophilic diblock copolymers as well as pH-responsive microgels are utilized as nanoreactors for the synthesis of noble metal nanoparticles to be eventually used as catalysts in hydrogenation and

oxidation reactions. PHEGMA-b-PDEA diblock copolymers were synthesized by group transfer polymerization and their unimer-to-micelle transformations have been investigated as a function of the solution pH. The micelles are formed at high solution pH and comprise a PDEA core and a PHEGMA corona. PDEA microgels were synthesized by emulsion polymerization and their reversible swelling properties are investigated in water by adjusting the solution pH. These particles are used as nanoreactors for the synthesis of Pt nanoparticles: efficient impregnation with Pt nanoparticles can be achieved by incorporating precursor platinum compounds (e.g., H_2PtCl_6), followed by metal reduction using, e.g., NaBH_4 . Hence, Pt nanocrystals nucleate and grow upon metal reduction with sizes in the range of a few nanometers.

Two synthetic routes have been utilized and are compared herein; in the first method the K_2PtCl_6 precursor was added at low pH to the PHEGMA-b-PDEA unimer solution or to the hydrophilic swollen microgel particles (Method A) followed by metal reduction and the pH was raised by the addition of base, while in the second H_2PtCl_6 was added at high pH to the micellar solution or the hydrophobic latex particles and then the metal salt was reduced in situ using NaBH_4 (Method B). The structure of the hybrid systems was investigated by Small Angle X-ray Scattering (SAXS) during the three steps of the metal nanoparticle synthesis: the original micelle or microgel dispersion in water, the metal-loaded particles and the metal nanoparticle-containing polymer matrices after reduction.

3.2 Experimental Section

3.2.1 Materials

A diblock copolymer comprising hydrophilic methoxy hexa(ethylene glycol) methacrylate (HEGMA) and pH-responsive 2-(diethylamino)ethyl methacrylate (DEA) units, PHEGMA-*b*-PDEA, was prepared by group transfer polymerization (GTP) chemistry in THF using glass reactors under dry nitrogen and standard Schlenk techniques as described elsewhere.³⁶ The molecular weight and molecular weight distribution of the PHEGMA-*b*-PDEA copolymer were determined by SEC using poly(methyl methacrylate) standards to be $M_n = 12300$ g/mole and $M_w/M_n = 1.13$ respectively. ¹H NMR spectroscopy was used to assess the composition (HEGMA:DEA mol ratio 1.3). Thus, the length of the hydrophilic PHEGMA block was estimated to be 50 units while the length of the pH-sensitive PDEA block was 40 units.

The microgel particles were synthesized in their latex form at pH 9 by emulsion copolymerization of DEA at 70 °C using an oligo(propylene glycol) diacrylate cross-linker in the presence of monomethoxy-capped poly(ethylene glycol) methacrylate stabilizer, as described elsewhere.³⁷ The microgel particles were purified by extensive ultrafiltration to eliminate excess stabilizer as well as traces of unreacted monomer and initiator. All chemicals used were commercially available and were purchased from Sigma-Aldrich (Germany).

3.2.2 Sample Preparation

Dilute solutions of the PHEGMA-*b*-PDEA polymers were prepared in Milli-Q water titrated to pH 1 or 2 using 12 M HCl. The appropriate amount of polymer was added in the low pH water and the samples were left stirring overnight to ensure complete polymer dissolution. Finally, all samples were adjusted to the required pH by the addition of 0.1 M NaOH and were allowed to stir for another 12 h.

Aqueous dispersions of the PDEA latex at a 2wt% concentration were adjusted to the required pH value using 0.1 M HCl or 0.1 M NaOH and were stirred for 24 h before measurement to ensure equilibrium swelling of the microgel particles.

3.2.3 Metal Incorporation

The incorporation of Pt species using H_2PtCl_6 or K_2PtCl_6 was carried out by the method described previously.³⁸ Two chemical routes were utilized for the introduction of the metal compounds within the polymeric matrices and their effectiveness is evaluated herein.

In the first method (method A) the appropriate amount of polymeric material (diblock copolymer or microgel particles) was dissolved in water at pH 2.0 to obtain a 2wt % polymer solution. The sample was stirred overnight to ensure complete polymer dissolution and then the K_2PtCl_6 metal precursor was added to the molecular polymer solution at various N/Pt molar ratios. More than 24 hrs were allowed for metal complexation, before the excess ionic species were removed by ultrafiltration using an Amicon[®] Stirred Ultrafiltration Cell by Millipore with regenerated cellulose ultrafiltration membranes, NMWL:3000. Reduction of the samples was carried out under vigorous stirring using a 3-fold excess of sodium borohydride (NaBH_4) in deionized water (12% of solution volume), and stirred overnight, followed by ultrafiltration. Upon addition of the reducing agent, the solutions instantaneously turned black and hydrogen gas rapidly evolved.

In the second method (method B) the pH was raised to 10 using 0.1 M NaOH to form polymeric micelles or a microgel latex dispersion. After stirring overnight at room temperature the H_2PtCl_6 metal precursor was added to the polymer dispersion at various metal loadings. Metal reduction was carried out similarly to the procedure followed for the first method.

For the metallation of the micellar solutions, a third method (method C) was utilized as well, which involved the incorporation of the K_2PtCl_6 metal precursor at a micellar solution at pH 10, at a 1:1 N/Pt molar ratio. More than 5

days were allowed for metal coordination, followed by ultrafiltration and metal reduction as described above.

V. Katsamanis and K. Christodoulakis are acknowledged for preparing the metal nanoparticle-containing micelles and microgels respectively, under the supervision of Prof. M. Vamvakaki, to whom the author is grateful.

3.2.4 Small Angle X-ray Scattering

SAXS experiments were performed on the Dutch-Belgian Beamline (DUBBLE) at the European Synchrotron Radiation Facility (ESRF) station BM26B³⁹ in Grenoble, France. SAXS data were recorded on a two-dimensional position sensitive detector.⁴⁰ Two different energies of the X-ray beam were used, 15 keV and 8 keV, each one for a different sample-to-detector distance, 2 m and 7 m respectively, and thus a wide scattering vector range was covered, $0.04 < q < 6.4 \text{ nm}^{-1}$. The magnitude of the scattering vector is $q=(4\pi/\lambda)\sin\theta$ with 2θ the scattering angle.

The two-dimensional images were radially averaged around the center of the primary beam, in order to obtain the isotropic SAXS intensity profiles. The scattering patterns from a specimen of wet collagen (rat tail tendon) and silver behenate were used for calibration of the q scale of the scattering curves. The data have been normalized to the intensity of the incident beam (in order to correct for primary beam intensity decay) and corrected for absorption, background scattering and polymer concentration, for the non-metalated solutions solely. For the metal-containing samples no concentration correction has been applied, since the amount of the added metal compound is negligible with respect to the total mass of the sample. Two ionization chambers placed before and after the sample, were utilized for the monitoring of the incident and the transmitted beams. Lupolen[®] and Eltex[®] were used as reference samples for the intensity calibration in absolute units (cm^{-1}). The background correction was made by subtracting from the total intensity the contribution of density fluctuations evaluated from measuring pure water. All samples were measured in appropriate glass capillary tubes of 2 mm diameter and the measurements were conducted at room temperature.

3.3 *Micelles Impregnated with Pt Nanoparticles*

3.3.1 pH-Induced Micellization

The properties of the PHEGMA-*b*-PDEA diblock copolymer solutions as a function of the solution pH have been investigated in earlier works^{18, 19, 30} and the pH-responsive character of the PDEA copolymer blocks has been proved. PHEGMA is a neutral polymer and is not affected by changes in the solution pH. However, PDEA comprises tertiary amine groups of a weak base character and, thus, participates in an acid-base equilibrium. The amine units are protonated and hydrophilic at low pH, while, when the pH increases above ~ 7 (effective pK_a of the protonated PDEA) they become deprotonated and hydrophobic. In this range of pH, micelles are expected to form with PDEA core and PHEGMA corona.

The scattering profile acquired for a 2wt% PHEGMA-*b*-PDEA aqueous solution at pH 10 is indicative of the pH-induced micellization (Figure 3.3.1). The broad oscillation observed above 0.4 nm^{-1} does not fully conform to the form factor of a homogeneous sphere, yet it is characteristic of a core-shell structure. Simulating the experimental curve with a core – homogeneous shell model^{41, 42} was not satisfactory, however a total micellar radius of approximately 13 nm was derived. It is noted that Dynamic Light Scattering measurements proved that spherical micelles are formed with a hydrodynamic radius of around 12 nm, which is consistent with the total radius estimated by SAXS. Several other models have been applied (e.g. core – inhomogeneous shell⁴³) without being able to describe successfully the micellar profile, due to the large width of the second oscillation. It is anticipated that the failure to simulate the data originates either from the graft-like form of the PHEGMA blocks residing in the shell, or the peculiar electron density profile of the structure; the electron densities derived for PDEA, PHEGMA and water were $8.63 \times 10^{-6} \text{ \AA}^{-2}$, $9.7 \times 10^{-6} \text{ \AA}^{-2}$ and $9.44 \times 10^{-6} \text{ \AA}^{-2}$ respectively, signifying that the solvent density is lower than that of the shell, but higher than that of the core.

3.3.2 Metallation of the Micelles using Method A

Figure 3.3.1 shows the SAXS profiles acquired for the various synthetic steps followed for the formation of Pt nanoparticles within the PHEGMA-*b*-PDEA micelles using method A at a 1:1 N/Pt molar ratio. Method A involves the incorporation of the K_2PtCl_6 precursor at a low pH, at which unimer chains are dissolved in the aqueous medium, and the subsequent in situ metal reduction using NaBH_4 , followed by the increase of the pH by NaOH . The profile acquired after metal incorporation at pH 2 (2nd step) suggests the formation of stable micelles. In this case complexation-induced micellization takes place, due to the electrostatic interactions between the negatively charged PtCl_6^{2-} and the positively charged amine.^{18, 19, 44} The scattering pattern corresponds to a core – shell structure and the significant increase of the intensity at the low q -range was attributed to the increased contrast provided by the PtCl_6^{2-} salt that resides the PDEA core. A second oscillation was evident above 1 nm^{-1} , yet less broad than that apparent for the pure micelles.

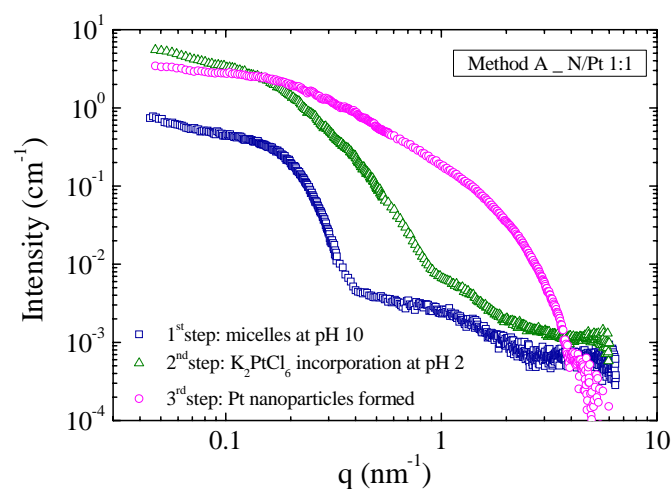


Figure 3.3.1: SAXS intensity profiles acquired for the synthetic steps followed for the formation of Pt nanoparticles within the PHEGMA-*b*-PDEA micelles at a N/Pt 1:1 molar ratio, following method A. The profile that corresponds to the 2wt% micellar solution at pH 10 (squares) is included as well.

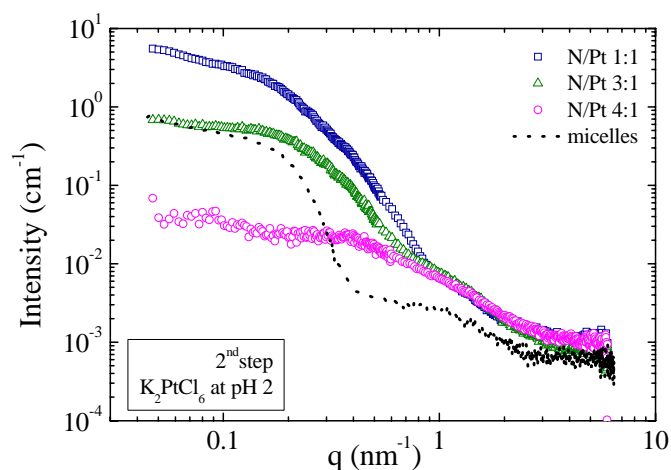


Figure 3.3.2: The scattered intensity acquired for the K_2PtCl_6 -loaded micelles at 1:1 and 4:1 N/Pt metal loading. The metal precursor was incorporated at pH 2 (method A). The curve acquired for the 2wt% micellar solution is presented as well.

The SAXS profiles acquired for the various polymer-to-metal ratios under study are presented in Figure 3.3.2. Decreasing the metal loading resulted in a decrease in the scattered intensity at low q 's, whereas the intensity above 0.8 nm^{-1} , namely the second oscillation and the background, remained unaffected. This is evidence that this broad oscillation is related to the scattering of the micellar corona, since the $PtCl_6^{2-}$ salt does not interact with the PHEGMA blocks. Additionally, this finding implies that the shell thickness remained constant, as well as the number of micelles in the solution. On the other hand, the scattered intensity at low q 's was found to depend on the metal loading and, thus, this part of the scattering pattern should be related to the micellar core. Increasing the metal loading was expected to result in an increase of the electron density of the core and a consequent increase of the scattered intensity. In fact, the scattering data have been simulated to a core – homogeneous shell form factor and it was derived that changing the contrast in favor of the electron density of the core resulted in a variation of the scattering pattern similar to that observed for the N/Pt 1:1 and 3:1 profiles. It is noted that the dimensions of the micelles were kept constant during simulations and a total micellar radius of 13 nm was utilized. Although the simulated curves failed to fully describe the experimental data, the reproduction of the trends that are apparent in Fig. 3.3.2 is considered to be a

qualitative proof of the successful metallation of the micellar cores, without influencing the structure of the polymeric matrix. This finding was further supported by DLS measurements that proved that the hydrodynamic radii of the metal-induced micelles were very similar to the micelles obtained by the pH increase.¹⁸

The pattern that corresponds to the sample loaded at a 4:1 polymer-to-metal ratio could not be simulated to a core – shell form factor, even for setting the electron density of the core equal to that of the solvent (hollow sphere case⁴²). Nonetheless, it can be fitted successfully using a Debye form factor^{45, 46} which describes the scattering of Gaussian chains. This would suggest that no micelles are formed within the aqueous medium, since the low metal loading could hinder the complexation-induced micellization. This scenario seems improbable since Pt nanoparticles have been successfully formed after reduction, as discussed below, and, hence, a core – shell structure is also speculated for the sample loaded at this polymer-to-metal ratio.

After metal reduction of the sample loaded at a N/Pt 1:1 molar ratio, the scattered intensity increased abruptly at the high q -range, while no significant changes in the values of the intensity was observed for low wavevectors (Fig. 3.3.1). This increase is characteristic of the formation of metal nanoparticles. A form factor minimum is observed at around 4 nm^{-1} corresponding to a particles radius of 1 nm and the form factor of spherical particles has been utilized to fit the data. Although a very good fit was obtained for $q > 0.4 \text{ nm}^{-1}$, the scattering in the low q -range could not be successfully described. Several models have been utilized for the simulation of the scattering curve and, interestingly, it was proved that a satisfactory simulation can be achieved by applying a homogeneous core – shell model. For the core radius a value equal to that obtained for the nanoparticles was utilized, while the best-simulating total radius was 5 to 6 nm. This implies that the scattering arises from the metal nanoparticle and the nanoparticle-containing micellar core and, thus, the impregnation of the micelles with a single Pt nanoparticle is suggested. A high polydispersity is estimated for both the particle and its polymeric matrix and, for this, a good simulation of the whole curve could not be obtained. It should be noted that the formation of

particles outside the micellar nanoreactors would result in precipitation. However, the samples are proved to be stable with time, and no precipitation was observed, even several months after their preparation.

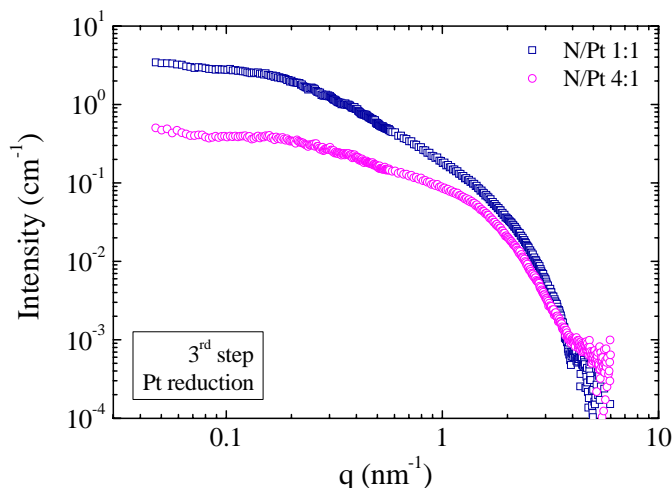


Figure 3.3.3: The scattering profiles of the Pt nanoparticle-containing micelles, obtained after reduction of the K_2PtCl_6 -loaded micelles with 1:1, 3:1 and 4:1 polymer-to-metal ratio.

Figure 3.3.3 shows the SAXS profiles obtained after metal reduction for the N/Pt 1:1 and 4:1 molar ratios. Pt nanoparticles of 1 nm radius were formed in both cases and the characteristics of the core-shell structure discussed above were apparent for both metal loadings. Although the size of the nanoparticles was found to be independent of the metal loading, decreasing the metal loading to 4:1 resulted in a decreased scattered intensity, which was attributed to a lower number of particles formed. The sample that was loaded at a N/Pt 3:1 molar ratio is not included in Fig. 3.3.3; however, its scattering curve exhibits similar features and the formation of 1 nm radius nanoparticles was also observed.

Hence, method A is proved to be a very effective method for the formation of metal nanoparticles within the micellar cores of pH-sensitive diblock copolymers. In Figure 3.3.4 the effectiveness of method C is examined. This method involves the incorporation of the K_2PtCl_6 metal precursor at a pH 10 solution and subsequent metal reduction. In this case micelles are already formed and the amine groups of the PDEA blocks are neutralized, preventing, thus, ionic complexation of the $PtCl_6^{2-}$ anions with the protonated amines. However, the scattering profiles acquired for the 2nd and the 3rd synthetic steps were similar to

those obtained when the same metal loading (N/Pt 1:1) was incorporated following method A (Fig. 3.3.4). Once more, Pt nanoparticles of 1 nm radius were formed within the micellar cores. It is proved, thus, that the PtCl_6^{2-} salt interacts with the uncharged amine due to metal coordination instead of electrostatic interactions, resulting in the bounding of the metal complex within the micellar core and the formation of Pt nanoparticles after reduction.

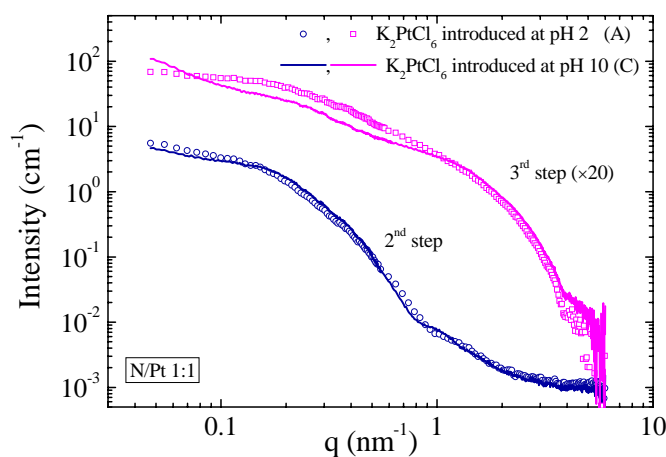


Figure 3.3.4: SAXS intensity patterns acquired before and after reduction of the K_2PtCl_6 -loaded micelles (2nd and 3rd step respectively). Methods A (symbols) and C (solid line) have been utilized and compared herein. The profiles acquired for the 3rd synthetic step have been shifted vertically by a factor of 20 for clarity.

3.3.3 Metallation of the Micelles using Method B

The effectiveness of a third method was also investigated. In method B the $\text{H}_2\text{PtCl}_6 \times 6\text{H}_2\text{O}$ metal precursor is added to a micellar solution at pH 10 at the required N/Pt molar ratio. More than 24 hrs were allowed for metal complexation followed by metal reduction.

The SAXS intensity profiles acquired after metal incorporation are presented in Figure 3.3.5 for the various metal loadings under study. The curve recorded for the N/Pt 16:1 molar ratio was similar to that obtained for the pure micellar solution of the same copolymer concentration, 2 wt%, which implied that micelles of the same structure exist in the solution but in a lower number density. The H_2PtCl_6 incorporation results in the protonation of a (difficult to quantify)

fraction of amines in the PDEA blocks and a partial decomposition of the micellar structure that subsequently reorganizes due to ionic complexation. Apparently the amount of metal complexes was too low and, thus, less micelles were re-formed with respect to those obtained by pH-induced micellization. When the metal loading was increased the scattered intensity increased as well, signifying the successful metal bounding. The profiles that correspond to a N/Pt 4:1 and 3:1 molar ratio exhibit a broad oscillation at around 1 nm^{-1} , similar to that observed in the scattering profiles acquired for method A. The intensity at low wavevectors increased with increasing the Pt loading, which was again attributed to the increased contrast induced by the metal incorporation to the micellar core. However comparing the patterns acquired for methods A and B at the same loadings proved that less metal was incorporated with method B, which suggests that the PtCl_6^{2-} anions were not evenly distributed in the micellar core following the two methods and that method B is less effective than method A.

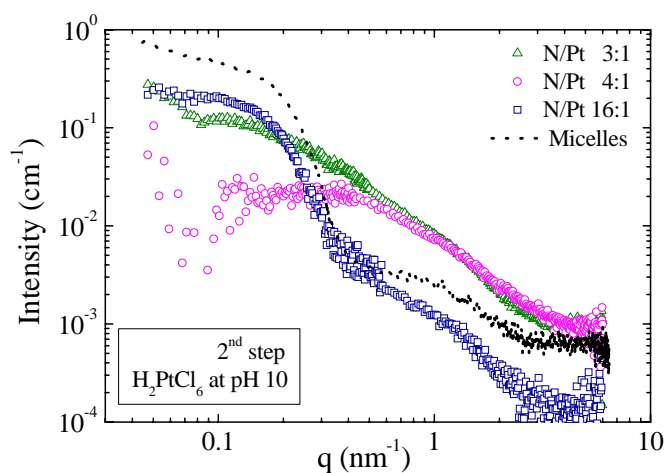


Figure 3.3.5: SAXS profiles acquired for the H_2PtCl_6 -loaded micelles at 3:1, 4:1 and 16:1 N/Pt metal loading. The metal precursor was incorporated at a pH 10 solution (method B). The curve acquired for the 2wt% micellar solution is included as well.

This outcome was further supported by the scattering curves acquired after metal reduction. The profiles corresponding to 4:1 and 16:1 polymer-to-metal ratios are presented in Figure 3.3.6. No evidence for the formation of nanoparticles was observed for the 16:1 sample. The increasing intensity in the low wavevector range was attributed to large aggregates that were formed upon

reduction and which eventually precipitate after a few days. For the sample loaded at a 4:1 N/Pt molar ratio the scattered intensity in the high q -range increases slightly, suggesting that nanoparticles were formed. A radius of 1 nm approximately was derived, similar to that calculated for the nanoparticles formed following method A. However, much less intensity was scattered by the particles suggesting that fewer particles were formed. The excess Pt atoms that were incorporated in the solution formed aggregates, which mainly scatter at low wavevectors and this is why the intensity was found to increase in this range. Once more, precipitation of the aggregates was observed after a few days. Therefore, it is proved that method B is not an effective synthetic route for the impregnation of PHEGMA-*b*-PDEA micelles with metal nanoparticles, since neither the metal loading can be controlled, nor the particle formation.

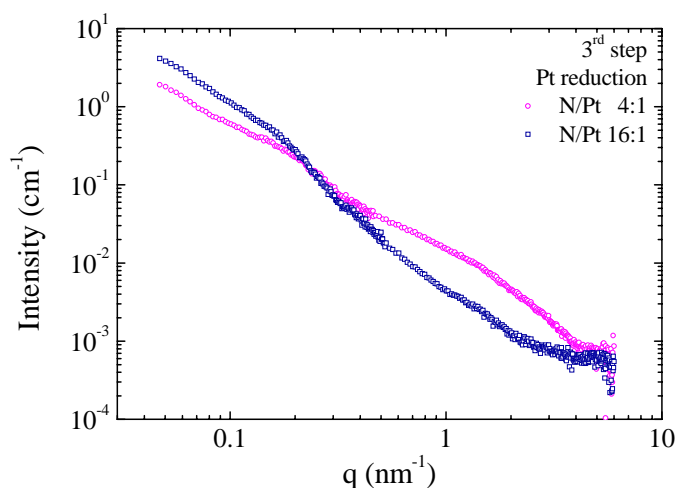


Figure 3.3.6: Scattering intensity patterns recorded after reduction of the H₂PtCl₆-loaded micelles at a N/Pt 4:1 and 16:1 molar ratio.

3.3.4 Concluding Remarks

The micellar cores of double-hydrophilic PHEGMA-*b*-PDEA block copolymers were utilized as nanoreactors for the formation of metal nanoparticles and the structural properties of the product nanohybrids are investigated in this section. PHEGMA is a neutral polymer and is not affected by changes in the solution pH, while the amine groups of PDEA are protonated at a low pH and, thus, hydrophilic, whereas at a high pH, above ~ 7 , they become deprotonated and hydrophobic. In this range of pH, micelles are formed with PDEA core and PHEGMA corona. SAXS measurements verified the pH-induced micellization and a core – shell structure of a total radius of ~ 13 nm was suggested.

Metal nanoparticles were synthesized within the core of the micelles by the addition of the appropriate metal precursor and subsequent reduction using NaBH_4 . Three different synthetic procedures have been investigated and compared herein. In method A, the K_2PtCl_6 metal precursor was added to a hydrophilic unimer solution at pH 2, at various metal loadings. The metal salt was found to incorporate within the micellar core, increasing the contrast and, thus, the scattered intensity at low wavevectors, whereas simulations showed that the size of the core and the shell remained unaffected. After metal reduction, Pt nanoparticles were formed with a radius of around 1 nm, for all three metal loadings under study. The scattering curves suggest that a single particle was formed per polymeric matrix, while their increasing number density with increasing the amount of incorporated metal indicated that only some of the micelles are impregnated. Similar scattering curves have been acquired for the formation of nanoparticles following method C. This method involves the addition of K_2PtCl_6 at a high pH and it was proved herein that the incorporation of PtCl_6^{2-} due to metal coordination is another efficient synthetic route for the impregnation of the PHEGMA-PDEA micelles with metal nanoparticles. However, when H_2PtCl_6 is added to a high pH micellar solution (method B) the formation of nanoparticles can not be controlled. Metal aggregates are formed instead, which precipitate with time.

3.4 Microgel Particles Impregnated with Pt Nanoparticles

3.4.1 pH-Responsive Character of the Microgel Particles

The PDEA microgels exhibit reversible swelling properties in water as a function of the solution pH; at low pH, the microgel particles are swollen, while an increase of the pH leads to hydrophobic latex particles. This microgel-to-latex transition upon increasing the solution pH is due to the protonation of the tertiary amine groups below pH 7, which allows the ingress of water within the microgels.⁴⁷ The scattering patterns acquired for the 2 wt% PDEA microgel solutions at pH 2, 7.3 and 10 are presented in Figure 3.4.1 and were the first to be analyzed. Note that the pH 7.3 and 10 curves have been shifted vertically for clarity.

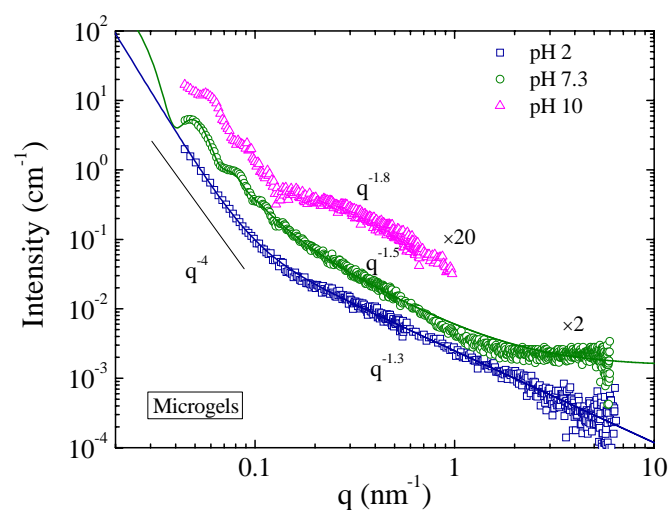


Figure 3.4.1: The SAXS intensity profiles of the 2wt% PDEA microgel solutions for pH 2, 7.3 and 10. The best fitting curves for the pH 2 and 7.3 samples are designated by solid lines, while the pH 7.3 and 10 curves have been shifted vertically by a factor of 2 and 20, respectively, for clarity.

The scattered intensity recorded for the solution at pH 2 decreases at a q^4 dependence in the low q -range, while for higher wave-vectors it exhibits a $q^{1.3}$ power-law decrease. The solid line designated in Fig.3.4.1 is the best fit curve, obtained by the addition of the two power-laws. The q^4 dependence observed in

the low q -range is attributed to the Porod scattering from the swollen at pH 2 microgel particles, whose radius exceeds that accessed within the q -range of the present investigation. As far as the $q^{1.3}$ power-law is concerned, it is attributed to the scattering from the overall interconnected network of the microgel. It is well known that a network structure scatters like^{48, 49} $S_f(q) = q^{-f}$, where f is the fractal dimension ($f < 3$). A fractal dimension close to 1 indicates a loosely connected network, whereas f increases as the medium becomes denser. At pH 2, f equals to 1.3 due to the swelling of the microgels, which reduces the density of the network.

When the solution pH is raised to 7.3, at least three well-defined minima appear in the low q -range, implying that the radius of the microgel is reduced and it is now within the length-scales probed in this experiment. Although the plateau regime is not accessible, the positions of the minima agree well with the condition fulfilled by the minima of the form factor of spherical scatterers and, thus, one can safely derive that the microgel particles are spherical. The spherical shape of the microgels has been confirmed by Dynamic Light Scattering in a preceding work.⁴⁷ The first minimum observed at around 0.069 nm^{-1} is the second order minimum of the form factor of a sphere with a radius $R = 110.5 \text{ nm}$, while the sharpness of the minima and the appearance of the fourth order minimum are indicative of the small polydispersity in the particles size.

The intensity that is scattered from a mono-disperse collection of particles of volume V and number density N_p is

$$I(q) = N_p (\Delta\rho)^2 V^2 P(q) S(q) \quad (3.4.1)$$

where $\Delta\rho$ is the difference in the scattering length densities between the scattering particles and the solvent, $P(q)$ is the form factor of the particles and $S(q)$ is the structure factor. For very dilute systems $S(q) \rightarrow 1$ and the structure factor contribution can be neglected. The form factor used for the description of the microgel particles is that of a homogeneous sphere of radius R

$$P(q) = \frac{9(\sin qR - qR \cos qR)^2}{(qR)^6} \quad (3.4.2)$$

The polydispersity that inevitably is introduced in the microgels radius was accounted with a Gaussian distribution $f(r)$,

$$f(r) = \frac{1}{\sqrt{2\pi}\sigma} \exp\left(-\frac{(r-R)^2}{2\sigma^2}\right) \quad (3.4.3)$$

were σ is the standard deviation of the distribution. The scattered intensity becomes

$$I(q, r) = N_p (\Delta\rho)^2 \int_0^\infty (V(r))^2 P(q, r) f(r) dr \quad (3.4.4)$$

The calculated intensity was fitted to the experimental data by adjusting the two parameters, R and σ , and using a scaling factor related to the product $N_p(\Delta\rho)^2$. The fitting was accomplished by a nonlinear least squares fitting procedure.

The use of a fractal term $S_f(q)$ which describes the contribution of the network to the total scattering was also required to fit the data. The best fitting curve is presented in Fig. 3.4.1 and corresponds to the scattering from spherical particles with $R = 111$ nm and $\sigma = 13$ nm, with an interconnected network of fractal dimension $f = 1.5$, higher than that found for the swollen microgels at pH 2. These findings confirm that at pH 7.3 the microgel particles are in the collapsed state, since R is reduced and the network became more dense.

A similar profile was acquired for the microgel solution at pH 10 while fitting of the data gave an $R = 99$ nm, $\sigma = 11$ nm and $f = 1.8$, which implied that the microgel particles were further collapsed as the pH increases further well above the pK_a of the PDEA microgels.³⁷

3.4.2 Metallation of the Microgel Particles using Method A

Figure 3.4.2 shows the SAXS profiles acquired for the various synthetic steps followed for the formation of Pt nanoparticles within the PDEA microgels using method A at a 4:1 N/Pt molar ratio. Method A involves the metallation of the hydrophilic microgel particles at low pH using K_2PtCl_6 and the subsequent in situ metal reduction using $NaBH_4$, followed by the increase of the pH by $NaOH$. As discussed above, the microgel particles at pH 2 are in the swollen state with a fractal dimension close to 1.

After the incorporation of the metal precursor (2nd step), the scattered intensity increases abruptly due to the increase of the contrast induced by the presence of the metal species. The increase in the scattered intensity is more pronounced in the low q range. A q^4 -dependence is observed in this regime while a shallow minimum appears at $q = 0.068 \text{ nm}^{-1}$, which is attributed to a second order minimum of the form factor of a sphere. A radius of around 115 nm is calculated for the metallated microgel particles, signifying that the incorporation of K_2PtCl_6 results in the deswelling of the microgel, which is attributed to ionic complexation between the divalent PtCl_6^{2-} anions and the protonated tertiary amine groups of the polymer network.⁴⁷

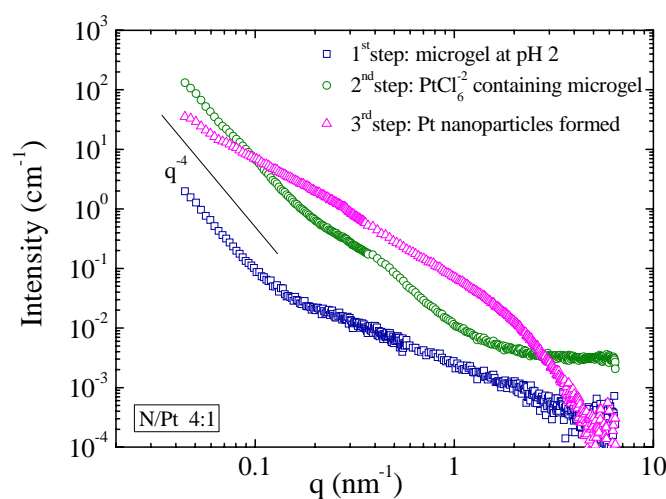


Figure 3.4.2: Scattering intensity curves for the various synthetic steps followed for the formation of Pt nanoparticles within the PDEA microgels at a 4:1 N/Pt molar ratio. K_2PtCl_6 has been used for the metal incorporation at pH 2 (Method A).

Moreover, besides the fractal contribution to the scattering from the interconnected network, a shoulder also appears at around $q = 0.4 \text{ nm}^{-1}$ and ends at a background of constant intensity. This shoulder is indicative of an extra contribution to the total scattered intensity, which could arise from particles of small size. Such particle-like structures could occur by the localized complexation of PtCl_6^{2-} anions and the charged tertiary amine groups within the hydrophilic microgel network, which suggests that Pt atoms concentrate locally within the matrix, increasing the electron density at the localization points. Thus, the

incorporated platinum is not homogeneously dispersed within the microgel particles; the PtCl_6^{2-} anions either form condensations that are distributed within the microgels volume or they are bounded all over the volume of the microgel and locally they concentrate to form the condensations mentioned above.

Hence, the experimental scattering curve has been fitted to that calculated by the summation of a q^{-4} power-law, a fractal term $S_f(q)$ and the form factor of a spherical particle,

$$I(q) = Aq^{-4} + Bq^{-f} + N_p(\Delta\rho)^2 \int_0^\infty (V(r))^2 P(q,r) f(r) dr \quad (3.4.5)$$

in order to take into account the contribution of the microgel particles, the interconnected network and the small particles, respectively (see Fig. 3.4.3 below). It is noted that the interference terms that are introduced in the scattering intensity of complicated particles, such as the microgels under study, are negligible, due to the big difference in the size of the microgels to that of the small particles.⁴⁵ Despite the high polydispersity, the particles radius was found 4.2 nm while the fractal dimension was $f = 1.8$, which is very close to that derived for the pure microgel particles at pH 10, verifying the collapse of the microgels at low pH upon metal complexation.

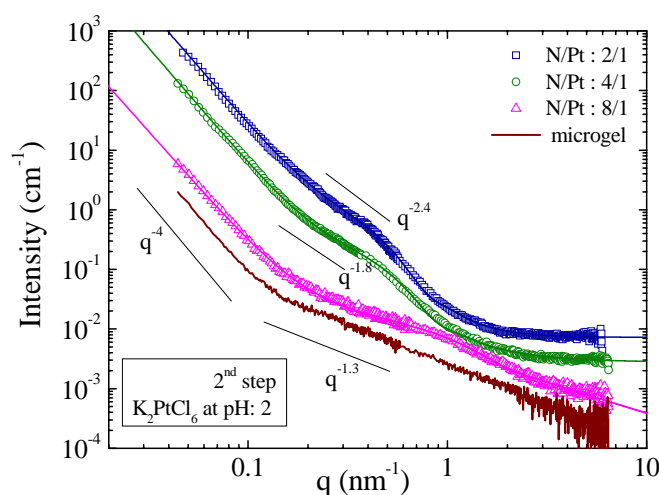


Figure 3.4.3: SAXS intensity profiles acquired for the K_2PtCl_6 -loaded microgels at 2:1, 4:1 and 8:1 N/Pt metal loading. The best fitting curves (solid lines) are included as well.

Two more polymer-to-metal ratios have been examined and the scattering profiles acquired for all three K_2PtCl_6 -loaded microgel samples are presented in Figure 3.4.3, along with the corresponding best fit curves. At low metal loading (N/Pt 8:1) the shape of the SAXS pattern is similar to that of the pure microgel solution at pH 2, but is shifted to higher intensities, indicating that the metal anions are bounded within the microgel particles and increase the contrast between the particle and the aqueous medium. The $q^{1.3}$ -dependence is again evident in the intermediate and high q -range, implying that the density of the network is not affected by the metal incorporation, at this metal loading. The expected decrease in the microgel size and the increase in the density of the network is very small for this low metal loading⁴⁴ and, thus, can not be probed by SAXS. By increasing the metal loading to N/Pt 4:1 the scattering curve is shifted to higher intensities, due to the increased PtCl_6^{2-} content, and ionic condensations are formed within the microgels, as described in the preceding paragraphs. At the same time, the microgels collapse and the network becomes denser, as indicated by the higher fitted fractal dimension ($f = 1.8$). Similar observations are valid for the microgel loaded at 2:1 N/Pt. Eq.3.4.5 utilized to fit the scattering curve gave a radius of around 4.7 nm for the ionic condensations, along with a fractal dimension $f = 2.4$ for the network. It should be noted that the fractal dimension increases from 1.3, 1.8 and 2.4 as the metal loading increases from 8:1, 4:1 and 2:1, suggesting that the network becomes denser upon metal complexation, as expected. The shrinkage of the microgel particles should result in the appearance of form factor minima in the low q -range of the scattering profiles however the increased polydispersity due to metallation or the increase in the intensity scattered by the metalated network prevent their observation.

Additionally, a linear increase is observed for the background intensity as the metal loading increases. Since the background intensity results from the sum of the scattering from the atomic species that are not part of the main scatterers, this linear increase is considered to be indicative of the distribution of metal anions all over the volume of the microgel particles. Hence, metallation of the matrix utilizing Method A results in a uniform bounding of the PtCl_6^{2-} anions

within the polymeric particle, while localized complexation also takes place. It is noted that all samples were ultrafiltrated before measurement.

After reduction, the scattering profiles are severely altered (Fig. 3.4.2). The intensity is raised in the high q -range, signifying that small particles have been formed. On the other hand the intensity at low wavevectors decreases with respect to that of the PtCl_6^{2-} containing microgel. These results suggest a redistribution of the scattering mass; before reduction, the Pt anions were distributed all over the microgel particle, resulting in high intensity at the low q -range, while after reduction the Pt atoms form 1 nm size nanocrystals embedded in the polymer network, which scatter at high q 's.

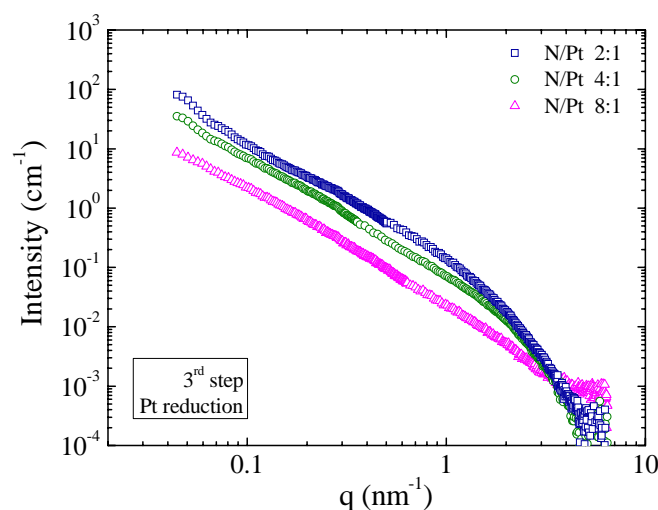


Figure 3.4.4: The scattering profiles of the Pt nanoparticle-containing PDEA microgels, obtained after reduction of the K_2PtCl_6 -loaded microgels with 2:1, 4:1 and 8:1 polymer-to-metal ratio.

The scattering patterns acquired for the nanoparticle impregnated microgels at the three polymer-to-metal ratios studied in this work are shown in Figure 3.4.4. The shape of the profiles is similar for all three samples while the total scattering intensity increases with the microgel metal loading. The profile that corresponds to the N/Pt 2:1 molar ratio exhibits two shallow minima in the low q -range, which allow to estimate the size of the microgel to be around $R = 117$ nm. It is reminded that the shape of the nanoparticle-containing microgels is spherical, as proved by DLS measurements.⁴⁷ Using a spherical form factor failed to fit the data at low q 's and the incorporation of a fractal term was necessary. The

value obtained for the fractal dimension was $f = 1.8$, equal to that obtained for the pure microgel at the collapsed state. The high q -range was fitted with the form factor of spherical particles with a radius of 0.8 nm and a polydispersity of around 0.3 nm, which are attributed to the metal nanocrystals embedded within the microgels. However, it was not possible to describe the scattering profile in the intermediate q -range by the sum of the contributions of the polydisperse Pt nanoparticles, the spherical microgel particles and the interconnected network. The contribution of the fractal term is apparent only in the low and intermediate q range and, actually, the effective fractal dimension increases with increasing q . More importantly, the network does not contribute to scattering in the high q -range, providing, thus, evidence that the network is distorted by the presence of the nanoparticles, and proving, hence, that they are formed within the microgels.

Similar analysis was applied to the scattering profile acquired for the sample at 4:1 metal loading after reduction (Fig. 3.4.4). The radius of the microgel particles was found to be around 120 nm, suggesting again the collapse of the microgels, while polydisperse Pt nanoparticles with a radius of approximately 0.7 nm were formed. For the N/Pt 8:1 metal loading the shape of the curve is similar, implying that the sample comprises similar structural components. However the total scattered intensity is reduced further, which hinders the fitting of the experimental data. In the high q -range a particle radius of around 0.7 nm was derived with a high polydispersity. The size of the microgels can not be calculated because no minima are observed in the low q range.

Thus, one can conclude that polydisperse metal nanoparticles are formed within the microgel particles in all cases, while the metal loading does not affect the size of the nanoparticles, which is constant around 1 nm in radius. Yet, the decreasing intensity at high wavevectors with increasing the polymer-to-metal ratio reveals a strong influence in the number of nanoparticles formed within the microgels. At higher metal loadings the number of nucleation sites increases while the growth of the nanoparticles is dictated by the thermodynamic terms and remains constant leading to nanoparticles of similar size.

3.4.3 Metalation of the Microgel Particles using Method B

The structure of the metallated samples using method B, which involves the incorporation of the metal salt precursor, H_2PtCl_6 , into the hydrophobic latex particles at high pH, followed by in situ metal reduction, was also investigated. Two polymer-to-metal ratios, 4:1 and 16:1, were investigated. As already discussed, the microgel particles at high pH exist in the collapsed state. For pH 7.3 and 10 the radius was found to be 111 nm and 99 nm, respectively, while the fractal dimension goes from 1.5 to 1.8, suggesting a denser interconnected network.

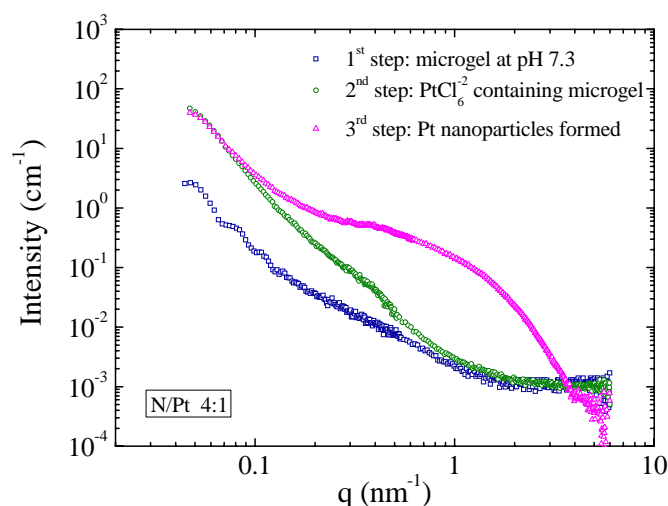


Figure 3.4.5: The SAXS profiles acquired for the various synthetic steps followed for the formation of Pt nanoparticles within the PDEA microgels at a 4:1 N/Pt molar ratio. Method B has been applied, that is addition of H_2PtCl_6 at a high pH, followed by metal reduction.

Figure 3.4.5 presents the SAXS profiles acquired for the various synthetic steps followed for the formation of Pt nanoparticles within the PDEA microgels at pH 7.3 and a N/Pt 4:1 molar ratio. The incorporation of the metal precursor resulted in an abrupt increase of the intensity at the q -range below 1 nm^{-1} , which is attributed to the metal bounding by the polymeric matrix and the subsequent contrast increase. For $q > 1 \text{ nm}^{-1}$, the intensity drops to that obtained for the pure microgel solution.

The scattering intensity profiles of the H_2PtCl_6 -loaded microgels are shown in Figure 3.4.6 along with the corresponding best fit curves. A shoulder similar to

that observed for the K_2PtCl_6 -loaded particle profiles is observed and, thus, the experimental curves were fitted using Eq. 3.4.5, to take into account the q^4 contribution from the microgel particles, the fractal term $S_f(q)$ that describes the network scattering and the form factor of a spherical particle for the ionic condensations. Ionic condensations of around 5 nm in radius were formed in the system loaded at N/Pt 4:1 molar ratio and the fractal dimension estimated for the low q -range was $f = 2.1$. For the N/Pt 16:1 sample the corresponding values were $R = 2.5$ nm and $f = 1.5$. In contrast to what observed for method A, the background intensity is independent of the metal loading and similar to that obtained for the pure microgel dispersion. The excess metal compound was removed by ultrafiltration and, therefore, this is evidence that all Pt atoms bounded by the polymer are condensated. The $PtCl_6^{2-}$ anions are not distributed all over the volume of the microgel, like in method A, but they are solely localized in ionic condensations.

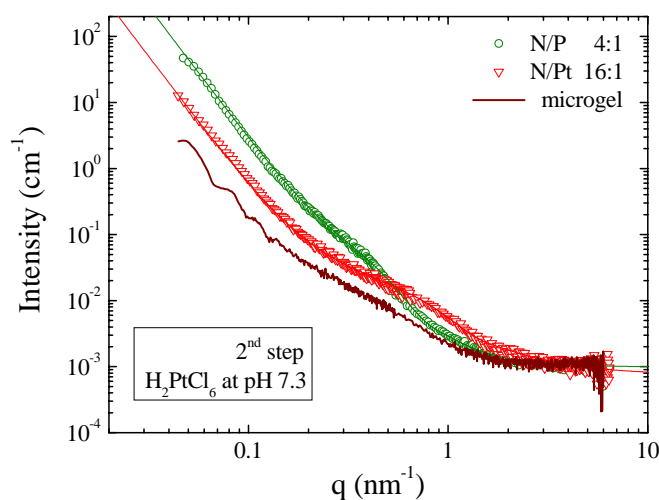


Figure 3.4.6: SAXS intensity profiles acquired for the microgels loaded with H_2PtCl_6 at pH 7.3. Two polymer-to-metal ratios, 4:1 and 16:1, were studied. The best fitting curves (solid lines) are included as well.

The different distribution of the incorporated metal salt observed for the two methods originates from the different processes that take place. The metal incorporation in method A is an one step procedure, that is ionic complexation

due to electrostatic interactions, while in method B, upon addition of the platinum acid to the microgel solution at pH 7.3 the tertiary amine groups of the collapsed microgels are partially protonated and the microgels swell, while ionic complexation follows.

Following metal reduction, the formation of Pt nanoparticles was manifested by the large increase of the scattered intensity in the high q -range, while the scattering at the low q -range remained unaffected (Fig. 3.4.5). The SAXS profiles acquired after reduction of all H_2PtCl_6 -loaded microgels are presented in Figure 3.4.7. In order to fit the data a similar procedure to that used for the K_2PtCl_6 -loaded microgels was applied. The radius of the nanoparticles formed within the PDEA microgels was calculated to be around 1 nm with a polydispersity of around 20%, while bigger particles with a 2 nm radius were formed for the 16:1 polymer-to-metal loading. The fitted fractal dimension f is 1.8 for both samples, equal to that estimated for the network of the pure microgel at the collapsed state. Unlike method A, the radius of the particles was found to decrease with increasing metal loading.

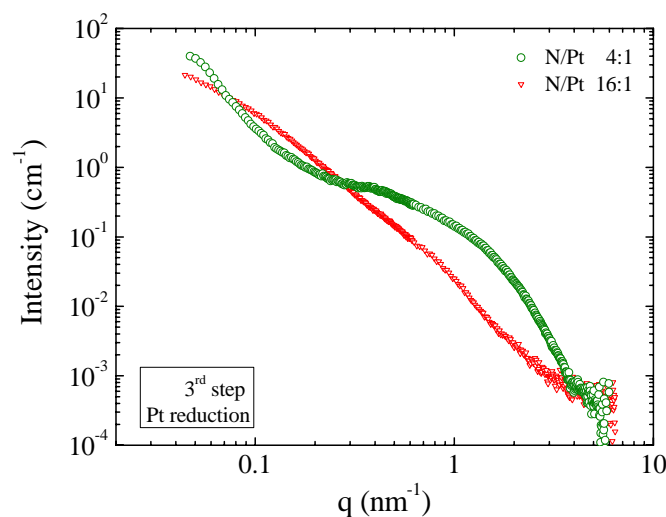


Figure 3.4.7: The scattering curves acquired after reduction of the H_2PtCl_6 -loaded microgels.

Noteworthy, the fractal structure factor $S_f(q)$ was found to contribute to the scattering throughout the whole wave-vector range accessed. This resulted in the superposition of the contribution of the nanoparticles to that of the polymeric network and it is indicative of the fact that the structure of the network is much

less affected by the particles formation with respect to method A. One could speculate that the metal nanoparticles are not distributed within the whole volume of the microgel particles. A possible scenario could be the metallation of the outer shell of the microgels that would lead to the formation of particles only at this region, leaving, thus, a big volume of the microgel intact. This selective metallation is governed by the fewer Pt atoms incorporated with respect to the amount of available amine sites, as well as the protonation of the neutral amine groups prior to ionic complexation. In this context the radii of the ionic condensations derived for the two metal loadings under study could be related to the thickness of the metallated shell, since a smaller radius was calculated for the sample loaded at a N/Pt 16:1 molar ratio.

3.4.4 Concluding Remarks

SAXS has been used to investigate the structure of pH-responsive microgels before and after metal incorporation. A decrease in the microgel radius accompanied by an increase of the fractal dimension f found upon increasing the solution pH confirmed the pH-responsive character of the microgels. The pH-responsive PDEA microgels were next utilized as nanoreactors for the formation of Pt nanoparticles. Two synthetic routes have been used for the incorporation of the metal precursor; in the first method, the K_2PtCl_6 precursor was added to hydrophilic swollen microgel particles at low pH (Method A), while in the second method, H_2PtCl_6 was added to hydrophobic latex particles at high pH, followed by in situ metal reduction using $NaBH_4$ and increase of the pH with $NaOH$ (Method B). The structure of the metallated particles has been investigated by SAXS during the three steps of the metal nanoparticle synthesis: the original polymer dispersions in water, the metal-loaded polymer matrices and the metal nanoparticle-containing polymers after reduction. The influence of the metal loading on the structure of the microgels was also examined.

The addition of metal precursor resulted in an increase of the scattered intensity at low q 's for both methods, signifying the complexation of the platinum salt by the polymeric matrix. An increase of the scattering intensity observed in

the intermediate q -range suggested that the metal compound is not homogeneously distributed within the metallated volume and evidences for the formation of ionic condensations were provided by the scattering patterns. However, further analysis of the scattering patterns indicated that, in method A, isolated PtCl_6^{2-} anions were also distributed within the whole volume of the microgel particle while only ionic condensations were apparent in method B. After metal reduction, Pt nanoparticles were formed. The size of these nanoparticles was found to be around 2 nm in diameter independent of the metal loading and the method used. The former affected only the number of particles formed in the polymer microgels, which decreased with increasing the polymer-to-metal ratio, N/Pt. On the other hand, an important difference concerning the topology of the metal particles arises for the two methods; microgel particles impregnated with Pt nanoparticles are obtained when method A is applied, while the formation of shell-decorated microgels is highly considered when method B is followed.

3.5 References and Notes

1. Henglein, A. *Chemical Reviews* **1989**, 89, (8), 1861-1873.
2. Lewis, L. N. *Chemical Reviews* **1993**, 93, (8), 2693-2730.
3. Feldheim, D. L.; Grabar, K. C.; Natan, M. J.; Mallouk, T. E. *Journal of the American Chemical Society* **1996**, 118, (32), 7640-7641.
4. Haruta, M. *Catalysis Today* **1997**, 36, (1), 153-166.
5. Jaramillo, T. F.; Baeck, S. H.; Cuenya, B. R.; McFarland, E. W. *Journal of the American Chemical Society* **2003**, 125, (24), 7148-7149.
6. Bockstaller, M. R.; Lapetnikov, Y.; Margel, S.; Thomas, E. L. *Journal of the American Chemical Society* **2003**, 125, (18), 5276-5277.
7. Chiu, J. J.; Kim, B. J.; Kramer, E. J.; Pine, D. J. *Journal of the American Chemical Society* **2005**, 127, (14), 5036-5037.
8. Chernyshov, D. M.; Bronstein, L. M.; Borner, H.; Berton, B.; Antonietti, M. *Chemistry of Materials* **2000**, 12, (1), 114-121.
9. Spatz, J. P.; Mossmer, S.; Hartmann, C.; Moller, M.; Herzog, T.; Krieger, M.; Boyen, H. G.; Ziemann, P.; Kabius, B. *Langmuir* **2000**, 16, (2), 407-415.
10. Grohn, F.; Bauer, B. J.; Akpalu, Y. A.; Jackson, C. L.; Amis, E. J. *Macromolecules* **2000**, 33, (16), 6042-6050.
11. Pich, A.; Bhattacharya, S.; Lu, Y.; Boyko, V.; Adler, H. A. P. *Langmuir* **2004**, 20, (24), 10706-10711.
12. Petit, C.; Pileni, M. P. *Journal of Physical Chemistry* **1988**, 92, (8), 2282-2286.
13. Lisiecki, I.; Pileni, M. P. *Langmuir* **2003**, 19, (22), 9486-9489.
14. Antonietti, M.; Wenz, E.; Bronstein, L.; Seregina, M. *Advanced Materials* **1995**, 7, (12), 1000-&.
15. Seregina, M. V.; Bronstein, L. M.; Platonova, O. A.; Chernyshov, D. M.; Valetsky, P. M.; Hartmann, J.; Wenz, E.; Antonietti, M. *Chemistry of Materials* **1997**, 9, (4), 923-931.
16. Sidorov, S. N.; Bronstein, L. M.; Valetsky, P. M.; Hartmann, J.; Colfen, H.; Schnablegger, H.; Antonietti, M. *Journal of Colloid and Interface Science* **1999**, 212, (2), 197-211.
17. Underhill, R. S.; Liu, G. J. *Chemistry of Materials* **2000**, 12, (8), 2082-2091.
18. Vamvakaki, M.; Papoutsakis, L.; Katsamanis, V.; Afchoudia, T.; Fragouli, P. G.; Iatrou, H.; Hadjichristidis, N.; Armes, S. P.; Sidorov, S.; Zhurov, D.; Zhurov, V.; Kostylev, M.; Bronstein, L. M.; Anastasiadis, S. H. *Faraday Discussions* **2005**, 128, 129-147.
19. Bronstein, L. M.; Vamvakaki, M.; Kostylev, M.; Katsamanis, V.; Stein, B.; Anastasiadis, S. H. *Langmuir* **2005**, 21, (21), 9747-9755.
20. Torchilin, V. P. *Journal of Controlled Release* **2001**, 73, (2-3), 137-172.
21. Rosler, A.; Vandermeulen, G. W. M.; Klok, H. A. *Advanced Drug Delivery Reviews* **2001**, 53, (1), 95-108.
22. Prochazka, K.; Martin, T. J.; Munk, P.; Webber, S. E. *Macromolecules* **1996**, 29, (20), 6518-6525.
23. Yu, K.; Eisenberg, A. *Macromolecules* **1998**, 31, (11), 3509-3518.

24. Vamvakaki, M.; Billingham, N. C.; Armes, S. P. *Macromolecules* **1999**, 32, (6), 2088-2090.
25. Gohy, J. F., Block copolymer micelles. In *Block Copolymers Ii*, 2005; Vol. 190, pp 65-136.
26. Lee, A. S.; Butun, V.; Vamvakaki, M.; Armes, S. P.; Pople, J. A.; Gast, A. P. *Macromolecules* **2002**, 35, (22), 8540-8551.
27. Arotcarena, M.; Heise, B.; Ishaya, S.; Laschewsky, A. *Journal of the American Chemical Society* **2002**, 124, (14), 3787-3793.
28. Gohy, J. F.; Antoun, S.; Jerome, R. *Macromolecules* **2001**, 34, (21), 7435-7440.
29. Yusa, S.; Shimada, Y.; Mitsukami, Y.; Yamamoto, T.; Morishima, Y. *Macromolecules* **2003**, 36, (11), 4208-4215.
30. Vamvakaki, M.; Palioura, D.; Spyros, A.; Armes, S. P.; Anastasiadis, S. H. *Macromolecules* **2006**, 39, (15), 5106-5112.
31. Xu, S. Q.; Zhang, J. G.; Paquet, C.; Lin, Y. K.; Kumacheva, E. *Advanced Functional Materials* **2003**, 13, (6), 468-472.
32. Murthy, N.; Xu, M. C.; Schuck, S.; Kunisawa, J.; Shastri, N.; Frechet, J. M. J. *Proceedings of the National Academy of Sciences of the United States of America* **2003**, 100, (9), 4995-5000.
33. Cao, R.; Gu, Z. Y.; Patterson, G. D.; Armitage, B. A. *Journal of the American Chemical Society* **2004**, 126, (3), 726-727.
34. Weissman, J. M.; Sunkara, H. B.; Tse, A. S.; Asher, S. A. *Science* **1996**, 274, (5289), 959-960.
35. Gan, D. J.; Lyon, L. A. *Journal of the American Chemical Society* **2001**, 123, (31), 7511-7517.
36. Bailey, L.; Vamvakaki, M.; Billingham, N. C.; Armes, S. P. *Polymer Preprints* **1999**, 40, (2), 263.
37. Christodoulakis, K. E.; Vamvakaki, M. *Macromolecular Symposia* **2009**.
38. Bronstein, L. H.; Sidorov, S. N.; Valetsky, P. M.; Hartmann, J.; Colfen, H.; Antonietti, M. *Langmuir* **1999**, 15, (19), 6256-6262.
39. Borsboom, M.; Bras, W.; Cerjak, I.; Detollenaere, D.; van Loon, D. G.; Goedtkindt, P.; Konijnenburg, M.; Lassing, P.; Levine, Y. K.; Munneke, B.; Oversluizen, M.; van Tol, R.; Vlieg, E. *Journal of Synchrotron Radiation* **1998**, 5, 518-520.
40. Gabriel, A.; Dauvergne, F. *Nuclear Instruments & Methods in Physics Research* **1982**, 201, (1), 223-224.
41. Pedersen, J. S.; Svaneborg, C. *Current Opinion in Colloid & Interface Science* **2002**, 7, (3-4), 158-166.
42. Pedersen, J. S. *Advances in Colloid and Interface Science* **1997**, 70, 171-210.
43. Forster, S.; Burger, C. *Macromolecules* **1998**, 31, (3), 879-891.
44. Anastasiadis, S. H.; Vamvakaki, M. *International Journal of Nanotechnology* **2009**, 6, (1-2), 46-70.
45. Glatter, O.; Kratky, O., *Small Angle X-ray Scattering*. Academic Press: 1982.
46. Higgins, J. S.; Benoit, H. C., *Polymers and Neutron Scattering*. Oxford University Press: New York, 1994.
47. Palioura, D.; Armes, S. P.; Anastasiadis, S. H.; Vamvakaki, M. *Langmuir* **2007**, 23, (10), 5761-5768.

48. Zemb, T.; Linder, P., *Neutron, X-rays and Light. Scattering Methods Applied to Soft Condensed Matter*. North-Holland: 1999.
49. Schaefer, D. W.; Martin, J. E.; Wiltzius, P.; Cannell, D. S. *Physical Review Letters* **1984**, 52, (26), 2371.

4 Crystallization Kinetics in Poly(ethylene oxide) / Layered Silicates Nanocomposites

4.1 Introduction

Polymer nanocomposites with inorganic layered silicates represent an attractive set of organic – inorganic hybrids,¹⁻⁸ due to their promising technological applications and because they constitute convenient macroscopic systems for the study of fundamental scientific problems, since they enable the investigation of the static and dynamic properties of macromolecules in nanoconfinement, utilizing conventional characterization techniques. The numerous applications that the organic – inorganic hybrids find in modern industry originate from the drastic improvement in properties, which is attributed to the large surface area provided by the nanostructure of the layered silicates and which is achieved without significant compromises in other characteristics.⁹ Enhanced mechanical properties in both modulus and tensile strength,¹⁰⁻¹³ increase in thermal stability,¹¹ self-extinguishing characteristics for flammability,¹⁴ reduction in the permeability of gases,^{4, 15} tunable biodegradability, as well as interesting electronic properties^{4, 16-18} that are achieved with only a small addition (<10%w/w) of nanoclays, are only a few of the properties of the organic – inorganic hybrids that are highly desirable in applications.

Poly(ethylene oxide), PEO, which is commonly mixed with inorganic silicates, to form nanocomposites, is used, among others, for applications in rechargeable and high-density power sources.^{17, 18} Despite the pronounced crystalline character of PEO, that inhibits the cation mobility, considerable effort is devoted to the development of solid polymer electrolytes based on PEO, which exhibit high ionic conductivity at room temperature and PEO-based electrolytes are still among the most studied soft ionic conductors.^{4, 16} Since the crystallinity of the polymers and the nature of the counterions appear to be the most important factor that control the ion mobility,¹⁹ the incorporation of inorganic nanophases

in the PEO matrix seems to be a promising way in order to control crystallinity and optimize the final properties.^{9, 17}

It is well known that depending on the organic – inorganic interactions, three different micro- or nanostructures may be obtained when mixing polymers with layered silicates: *phase separated systems* in the case of immiscible materials, *intercalated systems*, in which the polymer chains reside within the interlayer space forming 0.8-2.5nm films, and *exfoliated systems*, where the silicate's layered structure is destroyed and the inorganic platelets are dispersed in the polymeric matrix^{1, 2} (Figure 4.1).

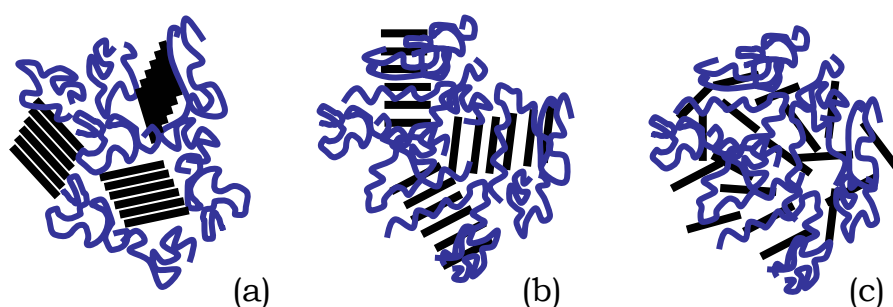


Figure 4.1: The three different micro- or nanostructures that are obtained when mixing polymers with layered silicates; (a) *phase separated systems*, (b) *intercalated systems* and (c) *exfoliated systems*

The systems that were studied were intercalated nanocomposites, in which the polymer crystallizes in the presence of the inorganic material, which in the present study was a hydrophilic layered silicate, sodium montmorillonite (Na⁺-MMT). Extensive research has been focused on the effect of the presence of the inorganic surfaces on the polymer crystallization, since this greatly affects the polymer mechanical and thermal properties. However, despite the increasing interest in PEO / Na⁺-MMT nanocomposites, the results concerning the effects of the Na⁺-MMT incorporation on the crystallization mechanism of the polymer matrix remain controversial. It has been proposed that the addition of Na⁺-MMT favors the heterogeneous nucleation of PEO allowing the control of semi-crystalline microstructure without remarkable changes in the polymer crystal fraction.²⁰ In another study, it is reported that the intercalation of the polymer in the Na⁺-MMT interlayer galleries hinders the bulk PEO crystallization,⁹ while in some cases the inorganic material is shown to produce a nucleating effect

stabilizing the bulk crystal phase.²¹ Thus, the main objective of our research is to study and try to elucidate the effect of the clay incorporation in the crystallization properties of polymer / layered silicate nanohybrids. It is noted that the study of polymer / layered silicate nanocomposites consists a large research activity in our group and many publications have appeared up to now, concerning the structure and dynamics in PEO nanocomposites,^{22, 23} the miscibility of PEO with the inorganic phase by altering the polymer / surface interactions,²⁴ the dynamics of poly(methyl phenyl siloxane) under severe confinement^{25, 26} and the structure of polypropylene nanocomposites.²⁷

The crystallization of polymers is described by the so-called “folded-chain” model, according to which the molecules fold back and forth forming lamellar structures of thickness ℓ_c , that are separated by amorphous regions of thickness ℓ_a (Figure 4.2). The characteristic period of the structure results from the addition of ℓ_c and ℓ_a and it is called long period, d^* . The lamellar crystallites contribute to the formation of spherical domains called spherulites. A spherulite consists of parallel lamellar stacks that extend radially from the centre of the structure.

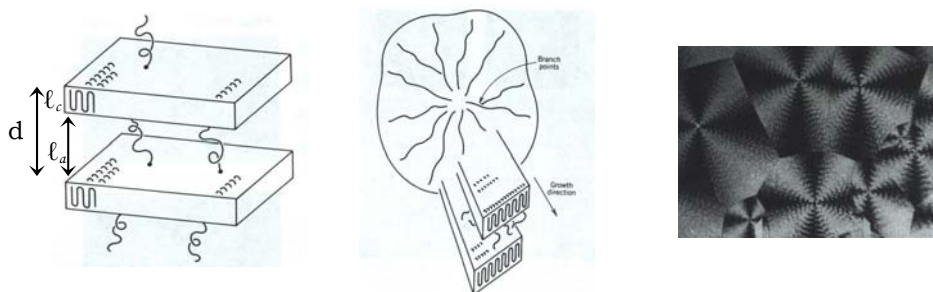


Figure 4.2: A schematic representation of the hierarchy induced in the crystallization of polymers; the lamellar crystallites that sequentially arrange themselves to form a spherulite and a POM view of a bunch of spherulites.

Thus, a hierarchy is observed in polymer crystals; the polymer unit cell is repeated to form lamellar crystallites that sequentially form a spherulite. The complete characterization of the crystallization of polymers requires a different characterization technique for each hierarchical step, due to the different length-scales explored. X-ray Diffraction, XRD, is utilized for the investigation of the unit cell, Small Angle X-ray Scattering, SAXS, for the lamellar crystallites that are

of interest in the specific research herein, and Polarized Optical Microscopy, POM, for the investigation of the spherulites.

In the present study, intercalated nanohybrids composed of PEO and the layered silicate sodium montmorillonite are examined with respect to the crystallization properties. The effect of the clay presence on the crystallization kinetics and the crystalline characteristics of PEO is investigated in nanocomposites with clay concentration up to 10%; the data are compared to those for pure PEO. The crystallization kinetics was studied by Time Resolved Small Angle X-ray Scattering measurements, which were carried out at the Dutch-Belgian Beamline (DUBBLE)²⁸ at the European Synchrotron Radiation Facility (ESRF) in Grenoble, France. The samples were annealed above the melting temperature and then quenched to different temperatures, all a few degrees above the non-isothermal crystallization temperature. After this the isothermal crystallization process was followed by time-resolved SAXS measurements, which enables the investigation of the lamellar formation and growth in the presence of the inorganic component.

4.2 Experimental Section

4.2.1 Materials

Poly(ethylene oxide) homopolymer, PEO, purchased from Aldrich ($M_w=100,000$, $T_g=-67^\circ\text{C}$ and $T_m=65^\circ\text{C}$) and hydrophilic sodium montmorillonite, Na⁺-MMT, purchased from Southern Clay, were used for the synthesis of the nanocomposites.

Na⁺-MMT belongs to the structural family of 2:1 phyllosilicates. Its crystal lattice consists of two silica tetrahedral sheets and one aluminum octahedral sheet (about 100nm wide and long) parallel to each other, that stack 1nm thick layers by weak dipolar forces, giving rise to interlayer galleries with an interlayer distance $d_{001}=11.7\text{\AA}$ (Figure 4.3). The isomorphous substitution that takes place within the layers generates negative charges that are normally counterbalanced by hydrated alkali or alkaline earth cations residing in the interlayer. The presence of the Na⁺ ions renders the silicate surface hydrophilic and, thus, pure Na⁺-MMT can only form intercalated structures when it is mixed with hydrophilic polymers. Na⁺-MMT has a cation exchange capacity (CEC) of 92.6mmol/100g and it was used after being heated at 120°C for 3h to allow the removal of water molecules residing within the galleries.

PEO is hydrophilic and semi-crystalline with a high degree of crystallinity. A PEO chain in the crystalline state has a helical structure which contains seven units and turns twice in the fiber identity period of 1.93 nm.

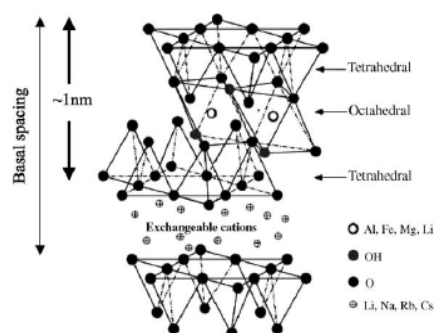


Figure 4.3 : A schematic representation of the structure of Na⁺-MMT layered silicates

4.2.2 Sample Preparation

The PEO / Na⁺-MMT nanocomposites were prepared by melt mixing; the two components were mixed in a mortar and then annealed in a vacuum oven at 100°C (i.e., at a temperature higher than the melting temperature of the polymer) for 2 days, which is considered to be enough for the intercalation to take place. Hybrids of various compositions have been prepared, i.e. 90%, 95% and 99%, where the composition is represented as weight percent of PEO. It is noted that the melting temperatures of the samples under studied were estimated by DSC to be 68.6°C, 60°C and 57.6°C for the 100%, 99% and 95% PEO hybrids, respectively.

4.2.3 Time-Resolved Small Angle X-ray Scattering

Small angle X-ray scattering, SAXS, data were recorded on a two-dimensional position sensitive detector²⁹ using an X-ray wavelength of 1.55 Å. The sample-to-detector distance was set at 5 m and the scattering vector range explored was $0.06 < q < 1.2 \text{ nm}^{-1}$; the magnitude of the scattering vector is $q=(4\pi/\lambda)\sin\theta$ with 2θ the scattering angle. The two-dimensional images were radially averaged around the center of the primary beam, in order to obtain the isotropic SAXS intensity profiles. The scattering patterns from a specimen of wet collagen (rat tail tendon) and Silver Behenate were used for calibration of the q scale of the scattering profiles. The data have been normalized to the intensity of the incident beam (in order to correct for primary beam intensity decay) and corrected for absorption. Two ionization chambers placed before and after the sample, were utilized for the measurement of the incident and the transmitted beam. Two procedures for background correction were applied; i) subtraction of the air and empty cell contribution to scattering from the total intensity, and ii) subtraction of the “liquid-like” background, that is the scattering of the polymer melt (with or without the clay particles). The latter is necessary for the correct calculation of the correlation function and ensures the dissociation of the contribution of the clay to the scattering pattern and the isolation of the polymer scattering. The samples were placed inside aluminium pans and a Linkam hot

stage was used for the temperature control. Time resolved measurements were performed on the PEO nanocomposites in order to record the lamellar formation and growth in the presence of the inorganic components. The samples were annealed at 100°C, above the melting temperature, T_m , kept there for 5 min and, after the acquisition of the melt scattering pattern, they were quenched at 30°C/min at different isothermal crystallization temperatures, T_{IC} , a few degrees above the non-isothermal crystallization temperature T_C . For the nanocomposites, T_{IC} varied between 46°C and 52°C by a step of 1°C, while, for the net PEO, this range was extended down to 42°C due to its lower T_C . Sequential SAXS patterns were acquired, following the isothermal crystallization at the respective T_{IC} . Data collection was started on reaching the isothermal crystallization temperature over consecutive acquisition time lapses of 15s, and was stopped a few minutes after the stabilization of the traces of the total scattered intensity and the transmission that were simultaneously monitored during the measurement, which is considered to be indicative of the end of the crystallization procedure.

4.3 Results and Discussion

Figure 4.4 shows the scattering patterns collected during the isothermal crystallization at 47°C of the nanocomposite with 90% PEO – 10% Na⁺MMT. The initial scattering patterns acquired during the isothermal crystallization correspond to those of the melt state of the amorphous polymer in the nanohybrid. After a while, a broad peak appears at $q^* = 0.28\text{nm}^{-1}$ approximately, corresponding to a lamellar long period of $d^* = 22\text{nm}$, with $d^* = 2\pi/q^*$. The intensity of this peak increases during crystallization and ultimately reaches a constant value. The patterns of all the nanocomposites at various T_{IC} possess similar features, however differences were observed in peak position, intensity and evolution time of the crystallinity peak.

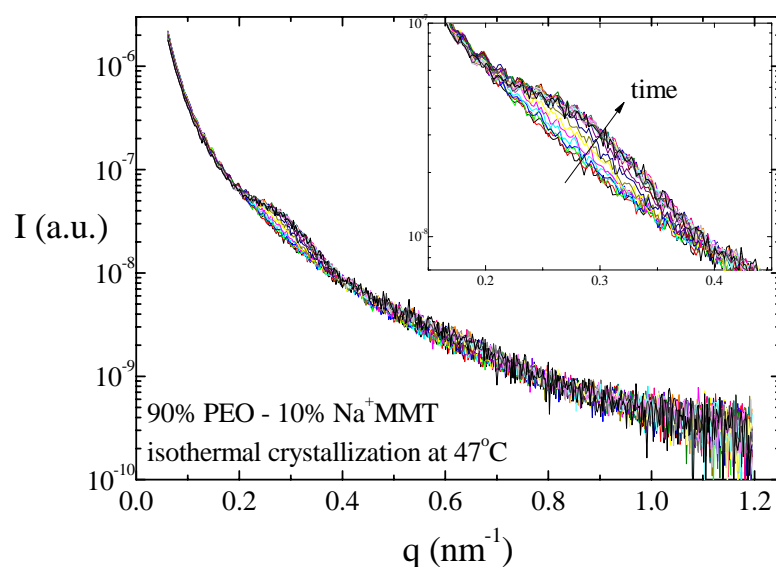


Figure 4.4: Time resolved SAXS patterns acquired during the isothermal crystallization of the 90% PEO - 10% Na⁺-MMT nanocomposite at 47°C

In order to find the scattering by a single lamellar stack and derive the dependence of the crystalline long period on the clay content and the crystallization temperature, the so-called Lorentz correction should be applied. The Lorentz corrected curves for a lamellar morphology, $I \times q^2$ vs q , are presented in Figure 4.5 and represent essentially the one-dimensional intensity profiles that

would be obtained if all the lamellar stacks were parallel to each other. The long period is derived by the peak position of the Lorentz corrected profiles and is apparently constant throughout the crystallization process, implying that a two-dimensional growth of the lamellar crystallites takes place, along the lamellar planes.

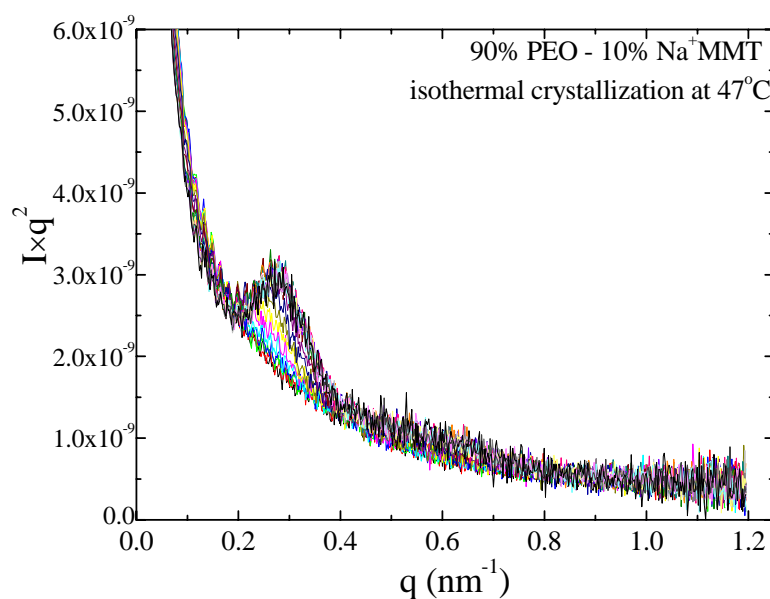


Figure 4.5: The Lorentz corrected patterns for the isothermal crystallization of the 90% PEO - 10% Na⁺-MMT nanocomposite at 47°C.

The results concerning the dependence of the crystalline long period on the composition and the isothermal crystallization temperature are presented in Figure 4.6. Increasing T_{IC} , or, equally, decreasing the supercooling, $|T_m - T_{IC}|$, results in an increase of d^* for all nanocomposites. This is an effect of the increase of the thickness of the lamella crystallite, ℓ_c , with decreasing supercooling, since the thickness of the amorphous region, ℓ_a , is known to depend only on the molecular weight of the polymer.³⁰ It is reminded that $d^* = \ell_c + \ell_a$. Moreover, the crystal growth perpendicular to the planar direction is affected by the inorganic phase; for small Na⁺-MMT content, 1wt%, the long period is found to increase with respect to that of the pure PEO sample at the same T_{IC} , while for higher Na⁺-MMT contents d^* decreases.

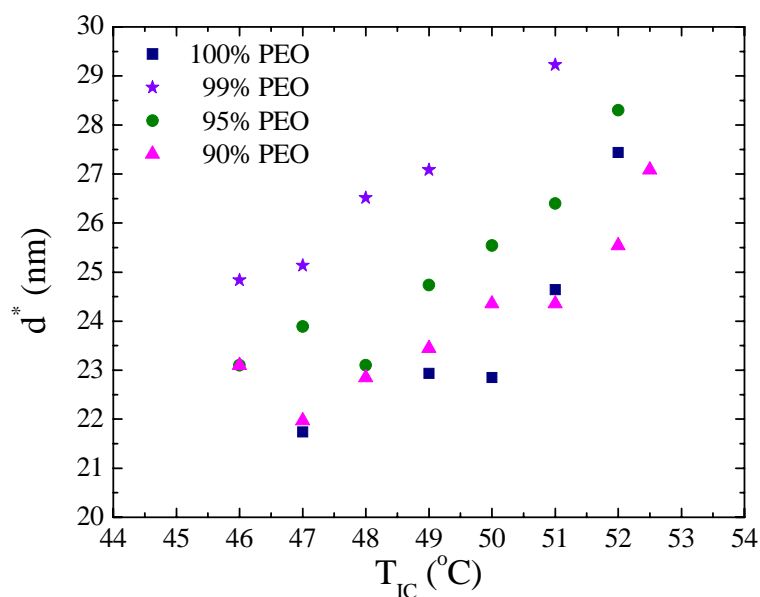


Figure 4.6: The long period, d^* , of the crystals formed for the various compositions of the PEO / Na⁺-MMT nanohybrids as a function of the isothermal crystallization temperature T_{IC} .

More importantly, the time resolved measurements can reveal useful information about the time $\tau_{1/2}$ that is related to the time required for the completion of half the crystallization process, and the nucleation mechanism, by appropriate utilization of the Avrami equation. The required analysis is based on the calculation of the invariant, Q , for each one of the scattering profiles acquired during crystallization. The invariant is evaluated by integrating the experimental intensity over the scattering vector q and reflects the mean square fluctuations of the scattering length density. In any investigation of crystallization kinetics, where, at intermediate stages, a sample is only partially filled by spherulites the invariant has the form:

$$Q = \int_0^{\infty} q^2 I(q) dq = (\Delta\rho)^2 v_s w_c (1 - w_c) \quad (4.1)$$

with $\Delta\rho$, v_s and w_c being the excess electron density between the crystalline and the amorphous phase, the volume fraction of lamellar stacks and the linear crystallinity, ℓ_c/d^* , respectively.³¹⁻³³ Since the long period and the crystalline thickness are constant throughout an isothermal crystallization experiment,^{30, 32} the linear crystallinity is constant as well, meaning that the invariant is proportional to the volume fraction of the spherulites, v_s . However,

$$v_s = \varphi_c / w_c \quad (4.2)$$

where φ_c is the bulk crystallinity, and, therefore, the invariant is proportional to the bulk crystallinity.

The evolution of the invariant with time during an isothermal crystallization experiment for some of the T_{IC} examined for the 95% PEO – 5% Na⁺-MMT nanocomposite, namely the crystallization isotherms, are presented in Figure 4.7. Similar profiles have been obtained for the other samples and for various T_{IC} . The invariant increases during the initial stages of the crystallization process and then stabilizes around a maximum value to form a plateau when the crystallization is completed. This maximum value, Q_∞ , is proportional to the maximum bulk crystallinity, v_s^∞ , achieved under the specific crystallization conditions and, thus, one can see that smaller supercooling results in lower crystallinity induced in the sample. It should be mentioned that for $T_{IC} = 52^\circ\text{C}$ the sample does not seem to crystallize in the time range explored by the experiment, signifying that the undercooling is not sufficient.

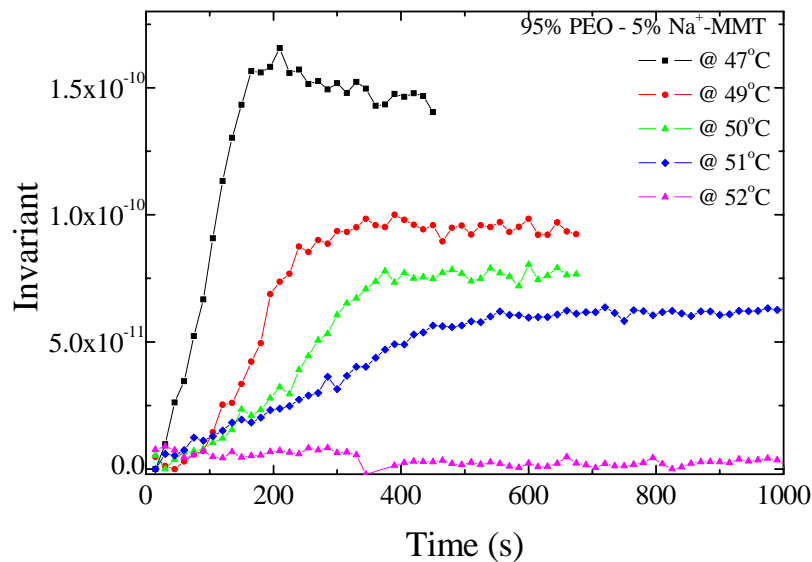


Figure 4.7: The evolution of the invariant during the isothermal crystallization of the 95% PEO – 5% Na⁺-MMT nanocomposites, at several isothermal crystallization temperatures

Another feature of the crystallization isotherms that changes with T_{IC} is the completion time that is the time needed for Q to reach the plateau value and, as

can be observed in Fig. 4.7, it is increasing with increasing T_{IC} . Actually, the parameter of interest is the characteristic time $\tau_{1/2}$, which is defined as the time at which the bulk crystallinity reaches the half of its maximum value. Recalling that Q_∞ is proportional to v_s^∞ , one can write:

$$\tau_{1/2} = \tau(v_s^\infty / 2) = \tau(Q_\infty / 2) \quad (4.3)$$

The characteristic times $\tau_{1/2}$ for the isothermal crystallization of the various nanohybrids are presented in Figure 4.8a, with respect to T_{IC} .

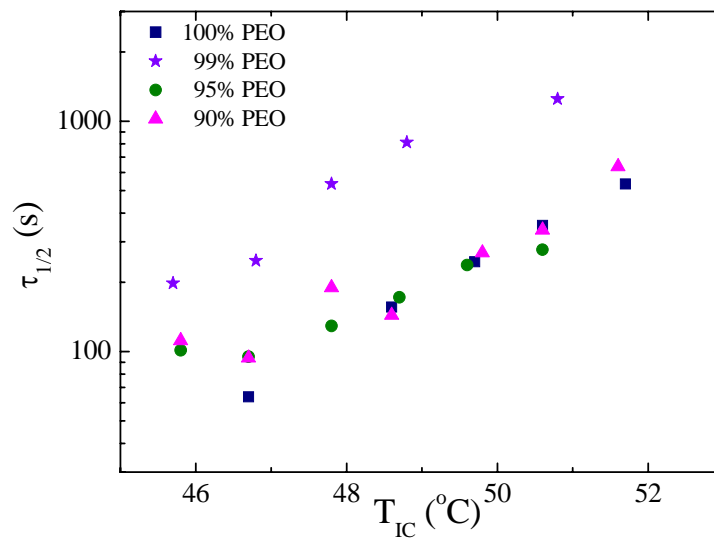


Figure 4.8a: The characteristic crystallization half-times $\tau_{1/2}$ as a function of the isothermal crystallization temperature, for the various PEO – Na⁺-MMT nanocomposites

As already mentioned, $\tau_{1/2}$ increases with decreasing supercooling, implying that the crystallization process becomes slower. This is due to the fact that the driving force for crystallization is reduced near the melting temperature, preventing, thus, crystallization. Note that for the small range of crystallization temperatures the effect of temperature on the chain mobility is minor and does not affect significantly the crystallization kinetics. The exponential increase of $\tau_{1/2}$ with temperature signifies that the crystal growth is associated with an activation barrier. The relation $\Delta \log \tau_{1/2} \propto \Delta T_{IC}$ has been proposed in the literature³⁰ and it was implied that the reverse of the slope of the $\log \tau_{1/2} - T_{IC}$ curve, b , was related to the activation barrier. However, an activated process should follow the

Arrhenius dependence (provided that the system under discussion is far away from the glass transition). Thus, the characteristic times of the crystallization process, $\tau_{1/2}$, should follow the Arrhenius dependence

$$\tau_{1/2} = \tau_{1/2}^0 e^{-\Delta F^*/RT} \quad (4.4)$$

with ΔF^* the activation energy and R the gas constant. The values of ΔF^* calculated from Fig. 4.8b for the pure PEO and the three hybrids are shown in Table 4-1.

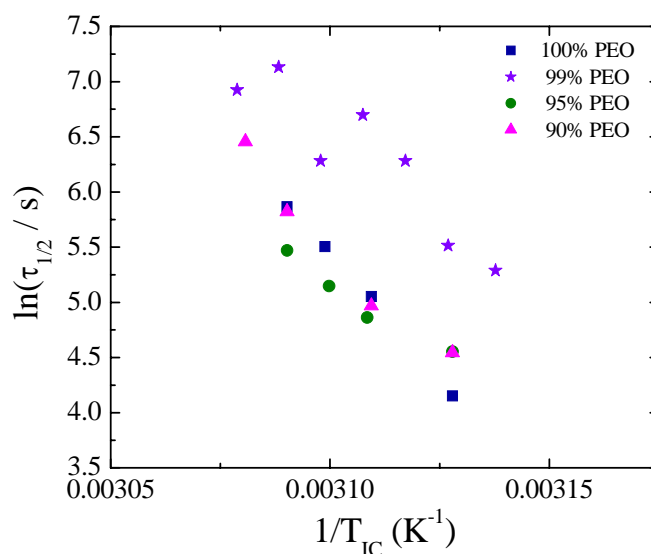


Figure 4.8b: Arrhenius representation of the characteristic crystallization half-times $\tau_{1/2}$ as a function of the isothermal crystallization temperature, for the various PEO – Na⁺-MMT nanocomposites

Table 4-1: The Activation Barrier and the Avrami Exponent, estimated for the crystallization of the PEO / Na⁺-MMT nanocomposites

Sample	Activation Barrier, ΔF^* (kJ/mol)	Avrami Exponent n
100% PEO	378	4.1
99% PEO	333	4.0
95% PEO	277	2.9
90% PEO	421	1.9

Although the range of temperatures investigated is very small and this introduces errors in the estimation of ΔF^* , it is observed that the incorporation of a small amount of Na⁺-MMT (1% & 5%) results in an decreasing ΔF^* , which corresponds to the nanoplatelets acting as nucleation centers and therefore favoring crystallization due to predetermined nucleation. However, for higher amounts of the inorganic component the activation barrier increases above the value derived for the pure PEO, signifying that the clay platelets obstruct the crystallization process.

Apart from the derivation of the characteristic half-time, $\tau_{1/2}$, the crystallization isotherms can be utilized for the study of the crystallization mechanism. It is well known that the time dependence of the bulk crystallinity φ_c is represented by the Avrami equation

$$\varphi_c(t) \propto 1 - \exp(-Zt^n) \quad (4.5)$$

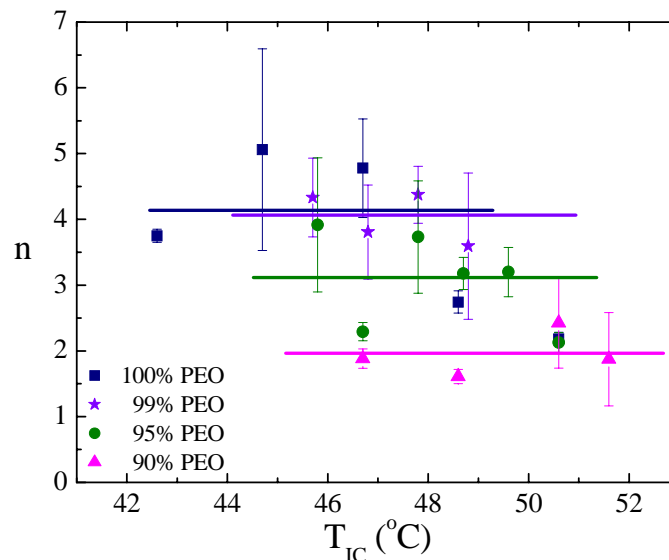


Figure 4.9: The Avrami exponent n calculated from the various crystallization isotherms of the PEO – Na⁺-MMT nanocomposites

where the Avrami exponent, n , and the rate coefficient Z are related to the shape of the nuclei, their growth rate and the time distribution of the nucleation events.³⁰ More specifically, n is indicative of the crystallization mechanism (sporadic or predetermined) and the restrictions induced in the crystal growth

(three-, two- or one- dimensional growth), while Z is a function of the growth rate of the nuclei, g , and their starting number, L , for predetermined nucleation, or the rate of increase of the number of nuclei, l , for sporadic nucleation.³⁴ It is noted that the results concerning Z are not presented herein, due to the lack of evidences concerning g and L or l .

The implementation of the Avrami equation on the crystallization isotherms presented in Fig. 4.7 is made possible due to the proportionality of the invariant with the bulk crystallinity. The Avrami equation has been directly fitted to the experimental invariant data, with n and Z being the variable parameters, along with a multiplication factor in order to incorporate the analogy between Q and φ_c , and the arbitrariness in the invariant unit. The results concerning the Avrami exponent are presented in Figure 4.9, for all samples and for all T_{IC} .

Although the values obtained have a rather large scatter, a trend for lower n values is observed for the hybrids with the higher clay content. A mean n value is calculated for each sample and the results are demonstrated in Table 4-1. For the pure PEO and the 99% PEO samples a value around 4 is calculated, which means that sporadic nucleation of spherical particles takes place and the growth of the nuclei is three-dimensional. This implies that the presence of a minor amount of the inorganic phase does not influence drastically the crystallization mechanism. The Avrami exponent for the 95% PEO sample is almost 3, suggesting that the nucleation is now predetermined with a three-dimensional growth of the nuclei, proving, thus, that the clay platelets act as nucleation centers. Increasing further the Na⁺-MMT composition, n decreases to 2 which is characteristic of predetermined nucleation, with the nuclei growing along the two-dimensions. This is a very important result since it signifies that the two-dimensional structure of the silicates actually controls the direction of growth of the lamellar crystallites as well.

4.4 Concluding Remarks

Summarizing, the effect of the incorporation of layered silicates on the crystallization of polymers has been investigated in a series of PEO / Na⁺-MMT nanocomposites, for high polymer compositions, namely above 90wt%. Time Resolved Small Angle X-ray Scattering measurements have been conducted during the isothermal crystallization of the nanohybrids and for various T_{IC} . The crystallization of the polymer is demonstrated through the appearance of a broad peak in the scattering patterns. The intensity of the peak increases during crystallization, reflecting the growth of the lamellar crystallites and the increase of the crystalline volume fraction, and approaches a plateau towards the completion of the crystallization process. The position of the scattering peak is constant throughout the isothermal crystallization, indicating that the long period d^* does not change during crystallization and, thus, a two-dimensional growth of the crystallites takes place, along the lamellar plane. However, it is proved herein that d^* is affected by the clay incorporation and it increases when the isothermal crystallization temperature increases. More importantly, the crystallization isotherms that were derived from the time resolved measurements enable the investigation of the crystallization mechanism. The characteristic time $\tau_{1/2}$ has been estimated and evidences on the decrease of the activation barrier with the incorporation of a small amount of clay have been provided. The role of the silicate platelets as nucleation centres has been confirmed through the calculation of the Avrami exponent n and the transition from sporadic nucleation, to predetermined three-dimensional and then to predetermined two-dimensional with increasing the clay content in the hybrids has been derived. This is a very interesting finding since it signifies that the two-dimensional structure of the silicates controls the direction of growth of the lamellar crystallites.

4.5 References and Notes

1. Giannelis, E. P.; Krishnamoorti, R.; Manias, E., Polymer-silicate nanocomposites: Model systems for confined polymers and polymer brushes. In *Polymers in Confined Environments*, 1999; Vol. 138, pp 107-147.
2. Alexandre, M.; Dubois, P. *Materials Science & Engineering R-Reports* **2000**, 28, (1-2), 1-63.
3. Alcoutlabi, M.; McKenna, G. B. *Journal of Physics-Condensed Matter* **2005**, 17, (15), R461-R524.
4. Giannelis, E. P. *Advanced Materials* **1996**, 8, (1), 29-&.
5. Ray, S. S.; Okamoto, M. *Progress in Polymer Science* **2003**, 28, (11), 1539-1641.
6. LeBaron, P. C.; Wang, Z.; Pinnavaia, T. J. *Applied Clay Science* **1999**, 15, (1-2), 11-29.
7. Schmidt, D.; Shah, D.; Giannelis, E. P. *Current Opinion in Solid State & Materials Science* **2002**, 6, (3), 205-212.
8. Fischer, H. *Materials Science and Engineering: C* **2003**, 23, (6-8), 763-772.
9. Sun, L.; Ertel, E. A.; Zhu, L.; Hsiao, B. S.; Avila-Orta, C. A.; Sics, I. *Langmuir* **2005**, 21, (13), 5672-5676.
10. Tjong, S. C. *Materials Science and Engineering: R: Reports* **2006**, 53, (3-4), 73-197.
11. Ratna, D.; Divekar, S.; Samui, A. B.; Chakraborty, B. C.; Banthia, A. K. *Polymer* **2006**, 47, (11), 4068-4074.
12. Luo, J. J.; Daniel, I. M. *Composites Science and Technology* **2003**, 63, (11), 1607-1616.
13. Manias, E. *Nature Materials* **2007**, 6, (1), 9-11.
14. Gilman, J. W. *Applied Clay Science* **1999**, 15, (1-2), 31-49.
15. Gorrasi, G.; Tortora, M.; Vittoria, V.; Pollet, E.; Lepoittevin, B.; Alexandre, M.; Dubois, P. *Polymer* **2003**, 44, (8), 2271-2279.
16. Vaia, R. A.; Vasudevan, S.; Krawiec, W.; Scanlon, L. G.; Giannelis, E. P. *Advanced Materials* **1995**, 7, (2), 154-156.
17. Hikosaka, M. Y.; Pulcinelli, S. H.; Santilli, C. V.; Dahmouche, K.; Craievich, A. F. *Journal of Non-Crystalline Solids* **2006**, 352, (32-35), 3705-3710.
18. Ruizhitzky, E. *Advanced Materials* **1993**, 5, (5), 334-340.
19. Aranda, P.; Ruizhitzky, E. *Chemistry of Materials* **1992**, 4, (6), 1395-1403.
20. Shen, Z. Q.; Simon, G. P.; Cheng, Y. B. *Polymer* **2002**, 43, (15), 4251-4260.
21. Strawhecker, K. E.; Manias, E. *Chemistry of Materials* **2003**, 15, (4), 844-849.
22. Chrissopoulou, K.; Afratis, A.; Anastasiadis, S. H.; Elmahd, M. M.; Floudas, G.; Frick, B. *European Physical Journal-Special Topics* **2007**, 141, 267-271.
23. Elmahdy, M. M.; Chrissopoulou, K.; Afratis, A.; Floudas, G.; Anastasiadis, S. H. *Macromolecules* **2006**, 39, (16), 5170-5173.
24. Chrissopoulou, K.; Altintzi, I.; Anastasiadis, S. H.; Giannelis, E. P.; Pitsikalis, M.; Hadjichristidis, N.; Theophilou, N. *Polymer* **2005**, 46, (26), 12440-12451.
25. Chrissopoulou, K.; Anastasiadis, S. H.; Giannelis, E. P.; Frick, B. *Journal of Chemical Physics* **2007**, 127, (14).

26. Anastasiadis, S. H.; Chrissopoulou, K.; Frick, B. *Materials Science and Engineering B-Advanced Functional Solid-State Materials* **2008**, 152, (1-3), 33-39.
27. Chrissopoulou, K.; Altintzi, I.; Andrianaki, I.; Shemesh, R.; Retsos, H.; Giannelis, E. P.; Anastasiadis, S. H. *Journal of Polymer Science Part B-Polymer Physics* **2008**, 46, (24), 2683-2695.
28. Borsboom, M.; Bras, W.; Cerjak, I.; Detollenaere, D.; van Loon, D. G.; Goedtkindt, P.; Konijnenburg, M.; Lassing, P.; Levine, Y. K.; Munneke, B.; Oversluizen, M.; van Tol, R.; Vlieg, E. *Journal of Synchrotron Radiation* **1998**, 5, 518-520.
29. Gabriel, A.; Dauvergne, F. *Nuclear Instruments & Methods in Physics Research* **1982**, 201, (1), 223-224.
30. Strobl, G., *The Physics of Polymers, Concepts for Understanding Their Structures and Behavior*. Springer: 2007.
31. Strobl, G. R.; Schneider, M. *Journal of Polymer Science Part B-Polymer Physics* **1980**, 18, (6), 1343-1359.
32. Talibuddin, S.; Bunt, J.; Liu, L. Z.; Chu, B. *Macromolecules* **1998**, 31, (5), 1627-1634.
33. Goderis, B.; Reynaers, H.; Koch, M. H. J.; Mathot, V. B. F. *Journal of Polymer Science Part B-Polymer Physics* **1999**, 37, (14), 1715-1738.
34. Sperling, L. H., *Introduction to Physical Polymer Science*. Wiley-Interscience: 2001.

5 Conclusions

In this thesis, three types of multiconstituent hybrid materials have been investigated with respect to their structural properties. An overview of the salient points discussed above is provided in this last section, as well as new ideas and suggestions on future work that could arise from the subjects treated herein.

The formation of block copolymer micelles in a homopolymer matrix that is selective for one of the copolymer block was thoroughly examined with emphasis on the effects of macromolecular architecture and composition, copolymer concentration in the mixture and temperature, as well as matrix homopolymer molecular weight.

The effect of the macromolecular architecture on the micelle formation and the micellar characteristics was primarily investigated. A series of graft (polyisoprene)₂(polystyrene), I₂S, graft copolymers and a series of the respective linear diblock copolymers were added to a low molecular weight polyisoprene homopolymer matrix at constant concentration 2 wt% and the micellization characteristics were investigated with Small Angle X-ray Scattering as a function of the composition f_{ps} . A (polystyrene)₂(polyisoprene), S₂I, graft copolymer was studied as well and the results were compared to those concerning its mirror I₂S copolymer. For the graft copolymer micelles, the core radius and the aggregation number was found to increase with increasing f_{ps} at constant total molecular weight. However, the aggregation numbers of the linear block copolymer micelles exhibited a weak dependence on the composition f_{ps} , despite the increase in the radius, implying that the macromolecular architecture influences the stretching of the chains in the core. The effect of the macromolecular architecture was also demonstrated by the comparison of the results for the two mirror grafts. Finally, the copolymer with the highest polystyrene volume fraction did not form micelles but rather lead to a macrophase separation with disordered copolymer-rich and homopolymer-rich domains.

Additionally, a series of miktoarm (polystyrene)_n(polyisoprene)_n, S_nI_n, star block copolymers, comprising n equal arms of polystyrene and n equal arms of

polyisoprene, was utilized to investigate the effect of macromolecular architecture on the characteristics of the micelles formed by the copolymers in a polyisoprene homopolymer matrix at various concentrations 0.05-2wt%, as a function of the functionality of the star copolymer n . The radius of the micellar core was found to be independent of n , the aggregation number decreased with increasing n exhibiting a n^{-1} power law dependence, while the volume fraction of copolymer chains participating in micelles was constant; these imply that the junction point of the copolymer does not affect the micellization process in any significant way. A simple thermodynamic model was developed following the methodology of Leibler in order to describe theoretically the micellization of A_nB_n copolymers in a B homopolymer matrix and the predictions of the model were in quantitative agreement with the experimental results, thus, signifying that the assumptions of the simple model are valid.

Next, the characteristics of a block copolymer/homopolymer blends were investigated as a function of concentration in the proximity of the critical micellization concentration (CMC) and as a function of temperature in the proximity of the critical micellization temperature (CMT). A symmetric linear polystyrene-*b*-polyisoprene, SI, diblock copolymer was added to a low molecular weight polyisoprene homopolymer matrix and the micellization characteristics were derived for a wide range of copolymer concentrations, namely from 0.01wt% up to 2wt%, and for the temperature range between room temperature and 160°C. Both the core radius and the aggregation number were found to be independent of the two variables, implying that the micellar features depend only on the macromolecular characteristics of the copolymer and the matrix. Just above CMC the volume fraction of micelles in the blends was increasing linearly with increasing concentration, in accordance to the theoretical predictions, however this dependence became weaker as the concentration was further increased. The “missing” micelles were primarily attributed to additional copolymer chains that remained free in the blends as unimers; the fraction of unimers was found to increase with increasing concentration. As far as the temperature effect was concerned, the dissolution of micelles was manifested by a gradual decrease of the volume fraction of micelles in the blend with increasing temperature up to the

CMT, while the dissolution temperature was proved to depend on the copolymer concentration in the blend and to be lower for lower concentrations.

In the last part of our study concerning the micellization, the homopolymer molecular weight was utilized as a control parameter for the tailoring of the micellar structure in block copolymer / homopolymer blends. A series of linear polystyrene-*b*-polyisoprene (IS) copolymers and a series of graft (polyisoprene)₂(polystyrene) (I₂S) copolymers of total molecular weight $\sim 100k$ was blended with polyisoprene homopolymer of 2k, 4k, 10k and 20k molecular weight, at constant concentration 2wt%. The micellar characteristics in the various matrices were derived as a function of the composition f_{PS} for the two macromolecular architectures. The core radius was found to increase with increasing the homopolymer molecular weight until phase separation takes place, while the micellar shape does not change. The results were compared to the theoretical predictions of two models; that of Leibler which assumes that the micellar corona is formed solely by the corona-forming blocks of the copolymers (Dry Corona) and the generalized model presented by Mayes and Olvera de la Cruz that takes into account the penetration of homopolymer within the corona (Wet Corona). The latter model was modified in the present work in order to describe the graft copolymer micelles. The comparison between the experimental values and the theoretical ones revealed the role of the penetration of the homopolymer within the corona with respect to the copolymer architecture and rendered the homopolymer molecular weight an important control parameter for tailoring the micellar characteristics.

Next, polymer/metal nanoparticle hybrids have been prepared and characterized with respect to their structural characteristics. Two different classes of pH-responsive polymeric nanostructures have been utilized as nanoreactors for the growth of colloidal metal particles: the micellar cores of double hydrophilic block copolymers and pH-sensitive microgels.

The micelles were formed by double hydrophilic diblock copolymers PHEGMA-*b*-PDEA. The hydrophobic PDEA block is pH-responsive: at low pH it can be protonated and it becomes hydrophilic, whereas at higher pH micelles are formed with the hydrophobic PDEA blocks immobilized within the micellar

cores. The PDEA microgel particles exhibit reversible swelling properties in water as a function of the solution pH: at low pH, the microgel particles are swollen, while an increase of the pH leads to hydrophobic latex particles. Metal nanoparticles were formed within the PDEA core by the incorporation of the appropriate metal precursor followed by metal reduction. Two synthetic routes have been utilized and were compared in our study; in the first method (A) the K_2PtCl_6 precursor was added to the PHEGMA-*b*-PDEA unimer dispersion or the hydrophilic swollen microgel particles at low pH followed by metal reduction and the pH was raised by the addition of base, while in the second (B) H_2PtCl_6 was added to the micellar solution or the hydrophobic latex particles at high pH and then the metal salt was reduced in situ using NaBH_4 . A third method (C) has been also applied for the impregnation of micelles, which involves the incorporation of K_2PtCl_6 at high pH. The structure of the hybrid systems was investigated by SAXS during the three steps of the metal nanoparticle synthesis: the original micelle and microgel dispersions in water, the metal-loaded polymer matrices and the metal nanoparticle-containing hybrids after reduction.

It was proved that method A is a very efficient method for the impregnation of pH-sensitive micelles with metal nanoparticles. The metal salt was found to incorporate within the micellar core due to ionic complexation and analysis of the SAXS data showed that the size of the core and the shell remained unaffected. After metal reduction Pt nanoparticles were formed with a diameter of around 2 nm for all metal loadings under study, the number density of which was found to increase with increasing metal loading. The scattering curves suggest that a single particle was formed per polymeric micelle, while their increasing number density indicated that only some of the micelles were impregnated. However, when H_2PtCl_6 was added to a high pH micellar solution (method B) the formation of nanoparticles could not be controlled. Metal aggregates were formed instead, which precipitated with time. The effectiveness of method C was examined as well and the impregnation of the PHEGMA-PDEA micelles with metal nanoparticles, based on the incorporation of PtCl_6^{2-} due to metal coordination was demonstrated.

As far as the microgel particles are concerned, a decrease in the microgel radius accompanied by an increase of the density of the network upon increasing the solution pH confirmed the pH-responsive character of the microgels. For both methods A and B, it was proved that the platinum salt was incorporated within the polymeric matrix due to ionic complexation and evidences for the formation of ionic condensations were provided by the scattering patterns. However, further analysis of the scattering profiles indicated that in method A isolated PtCl_6^{2-} anions were also distributed within the whole volume of the microgel particle, while only ionic condensations were apparent in method B. After metal reduction, Pt nanoparticles were formed. The size of these nanoparticles was found to be around 2 nm in diameter independent of the metal loading and the method used. The former affected only the number of particles formed in the polymer microgels, which decreased with increasing the polymer-to-metal ratio, N/Pt. On the other hand, an important difference concerning the topology of the metal particles arised for the two methods; microgel particles impregnated with Pt nanoparticles were obtained when method A was applied, while the formation of shell-decorated microgels was highly considered when method B was followed.

In the last part of this thesis, the structure of polymer/layered silicate nanocomposites was studied. Intercalated nanohybrids were prepared by mixing PEO and hydrophilic montmorillonite and the effect of the clay presence on the crystallization kinetics and crystalline characteristics of PEO was investigated by Time Resolved SAXS measurements, during the isothermal crystallization of the nanohybrids, as a function of crystallization temperature and polymer concentration.

During crystallization, lamellar crystallites grow and their volume fraction was found to increase, while the long period d^* did not change, suggesting a two-dimensional growth of the crystallites along the lamellar plane. The clay incorporation was found to affect d^* as well as the crystallization kinetics; the characteristic time $\tau_{1/2}$ for the completion of the crystallization process and the Avrami exponent n related to the crystallization mechanism were calculated and evidences on the decrease of the activation barrier with the incorporation of a

small amount of clay were provided. The role of the silicate platelets as nucleation centres was confirmed and the transition from sporadic nucleation, to predetermined three-dimensional and then to predetermined two-dimensional nucleation with increasing the clay content in the hybrids was derived, that implies that the two-dimensional structure of the silicates controls the direction of growth of the lamellar crystallites.

Suggestions for Future Work

All three subjects treated in the context of the present thesis were thoroughly investigated and a plethora of important conclusions was derived. During the study of each subject several new questions emerged and new ideas for the extension of our research came up. In this last paragraph some of these are cited and suggestions for future work are provided.

The most interesting idea related to the micellization in block copolymer/homopolymer blends was the study of micellization under confinement that is the micellization of block copolymers in a homopolymer thin film. The goal in such a case would be the formation of a single layer of ordered micelles, which could be potentially used as a nanopatterned surface. The formation of such a layer is not trivial, since the confinement of the micelles between two interfaces (substrate/polymer and polymer/air) in most cases prevents the block copolymer chains from self-assembling, due to the selective segregation of the chains to the two interfaces. However, the main framework for the treatment of this problem was set and the first Soft X-rays Scattering measurements were very promising for the success of this project.

Besides this very challenging project, one could continue the work on the macromolecular architecture effect by studying the micellization of the graft I₂S copolymers within a polystyrene matrix. In this case the two PI blocks of each copolymer chain reside the micellar core while the PS tooth blocks form the corona. The theoretical model for the micellization of AB₂ graft copolymers within an A homopolymer has already been derived, allowing thus the comparison between experimental results and theoretical predictions.

Furthermore, it would be interesting to investigate the structure of the micellar corona by complementary experimental techniques. Small Angle Neutron Scattering measurements could be conducted in a corona contrast, which involves the deuteration of the PI blocks of the copolymers. Since the PS blocks of the copolymers utilized in our study were already deuterated, one could employ the same copolymers added in a polystyrene matrix for this purpose.

As far as the impregnation of polymeric matrices with metal nanoparticles is concerned, a very promising idea could be the metalation of core-shell microgels and their structural study by SAXS. The metal compound could be incorporated either in the core or the shell of the microgels, providing the necessary contrast for the study of the respective part. Moreover, the formation of shell-decorated or core-decorated microgels is highly desirable and could be studied as well.

Finally, an integrated investigation of the effect of the clay incorporation on the crystallization of polymer/layered silicate nanocomposites demands for the utilization of differential scanning calorimetry, DSC, and polarized optical microscopy, POM, complementary to SAXS, in order to probe all the length-scales involved in the hierarchy of a polymer crystallite. These experimental are already ongoing. Simultaneous SAXS and WAXS measurements could be also performed, since questions regarding the very initial stages of crystallization are still open for investigation.

Appendix

Small Angle X-ray Scattering

The scattering theory and the fundamentals of a scattering experiment are well-described in several textbooks and for this the scattering equations are not included within the present thesis. Instead, we propose a bunch of books that the interested reader could consult:

- P. Linder and Th. Zemb (2002). *Neutrons, X-rays and Light: Scattering Methods Applied to Soft Condensed Matter*. Amsterdam: Elsevier.
- O. Glatter and O. Kratky (1982). *Small-Angle X-ray Scattering*. London: Academic Press.
- J. S. Higgins and H. C. Benoit (1994). *Polymers and Neutron Scattering*. Oxford: Clarendon Press.

The general set up of a scattering experiment is presented schematically in Figure A.1. A monochromatic beam of wavelength λ and intensity I_0 probes the sample and the scattered intensity is collected by a detector at a distance d under variation of the scattering vector \vec{q} . The magnitude of \vec{q} , $|\vec{q}| \equiv q$, is related to the Bragg scattering angle θ by $|\vec{q}| = \frac{4\pi}{\lambda} \sin \theta$.

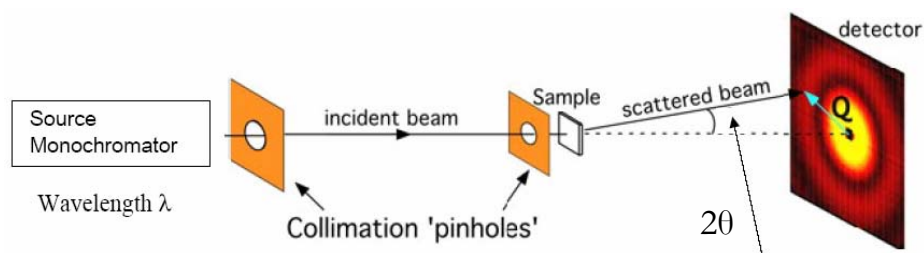


Figure A.1: A schematic representation of a scattering experiment

In a Small Angle X-ray Scattering experiment a 2-dimensional detector is usually utilized for the collection of the scattered intensity, placed a few meters away from the sample. Thus, a low q range is accessed, i.e. $0.01 - 5 \text{ nm}^{-1}$ depending on the energy of the beam and the sample-to-detector distance. A

typical scattering image is shown in Figure A.2 and the several steps that should be followed for the processing of such an image are described below.

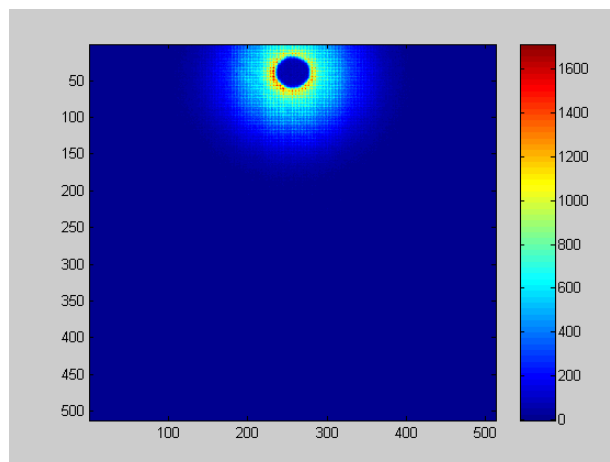


Figure A.2: A typical 2D scattering pattern of a sample that scatters isotropically

The zero intensity disk on the top of the image corresponds to the incident beam that is masked by a beam-stop. For an isotropic sample, rings of varying intensity are observed around the center of the incident beam, while the distance from the center is related to the corresponding q value. Therefore a radial average around the center should be applied in order to obtain the 1-dimensional scattering pattern (Fig. A.3).

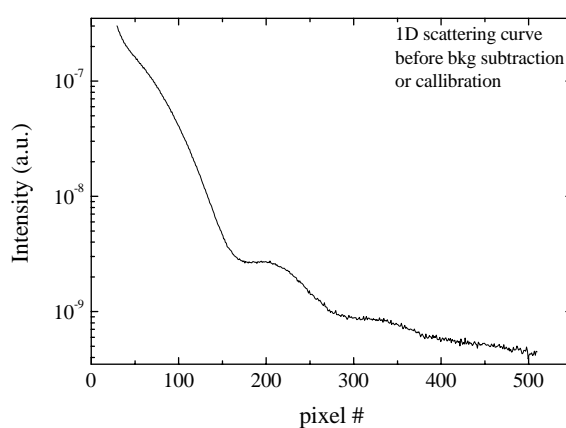


Figure A.3: The 1D scattering curve obtained after radial average of the 2D image presented in Fig. A.2

The q axis is calibrated using the scattering pattern of a specimen with well-defined scattering peaks of known position q^* . For this purpose either a rat tail

tendon or silver behenate can be utilized. The scattering patterns and the peak positions of these calibrants are provided in the end of the Appendix. Similarly, whenever needed, a sample of well-known scattering intensity can be measured during a SAXS experiment in order to calibrate the intensity axis in absolute units (cm^{-1}). In this thesis Lupolen and Eltex have been utilized, however the intensity of the scattering peak depends on the sample characteristics and therefore no values are provided herein.

A very important step in the processing of a scattering profile is the background subtraction and the correction of the transmission. The intensity that is scattered solely by the sample is calculated by:

$$I_{sc}^{sam} = \frac{I_{meas}^{sam+bkg}}{I_0^{sam+bkg}} - \frac{I_{meas}^{bkg}}{I_0^{bkg}} \frac{T^{sam+bkg}}{T^{bkg}} \quad (\text{A.1})$$

which is equivalent to:

$$I_{sc}^{sam} = I_{meas}^{sam+bkg} - I_{meas}^{bkg} \frac{T^{sam+bkg}}{T^{bkg}} \frac{I_0^{sam+bkg}}{I_0^{bkg}} \quad (\text{A.2})$$

The subscripts *meas* and *0* denote measured and incident intensity respectively, while the superscripts *sam* and *bkg* correspond to the sample or the background. The transmission is denoted by *T* and is calculated by the ratio of the transmitted and the incident beam that are measured during an experiment by two ionization chambers placed after and before the sample. The measured scattered intensity is always divided by the incident beam intensity in order to take into account the intensity decay of the X-ray beam with time.

However, when the scattered intensity is normalized to absolute units, cm^{-1} two extra corrections should be applied concerning the thickness, *t*, and the transmission of the sample, $T^{sam} = T^{sam+bkg} / T^{bkg}$, and, hence,

$$I^{sam} (\text{cm}^{-1}) = CF \frac{I_{sc}^{sam}}{t * T^{sam}} \quad (\text{A.3})$$

CF is the calibration factor that is derived from measuring a calibrant specimen, as discussed above. Figure A.4 shows the scattering profile that results after *q*-calibration, background subtraction, transmission correction and intensity normalization of the profile shown in Fig. A.3.

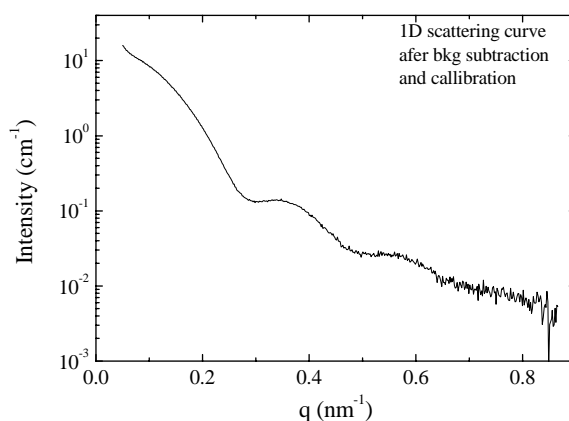


Figure A.4: The sample scattered intensity obtained after background subtraction, transmission correction and calibration of both the intensity and the scattering vector axis.

A Matlab[®] code has been written for the processing of the 2D images acquired in a scattering experiment. It includes the background subtraction, the transmission correction, the radial averaging and the normalization of the intensity and the q axis. The code is provided in the end of the Appendix.

The procedure described above is necessary for all scattering measurements recorded in a 2D detector. Once the final 1D scattering profile is calculated one should proceed with the analysis of the curve in order to derive the structural properties of the scattering entities. Thus, a form factor analysis could be applied in case of a very dilute suspension of the scattering objects, or a structure factor analysis, in case of interparticle scattering. Most of the systems investigated herein contain non-interacting spherical scatterers and, for this, the form factor of spherical particles was acquired during measurement (Fig. A.4). Fitting the data with the theoretical form factor of spherical particles was accomplished utilizing a Matlab[®] code that was written for this purpose and is cited in the end of the Appendix. The author acknowledges Dr. Evelyn van Ryumbeck for her help in writing the code. The radii of the particles as well as the forward scattering intensity were evaluated, while a Gaussian distribution was incorporated in the form factor to take into account the polydispersity in size and was also included in the code.

Matlab[®] code for the processing of a 2D image collected during a SAXS experiment

```
%%%%%%%%%%%%% DUBBLE.m %%%%%%%%%%%%%%
%%%%%%%%%%%%% by Eleni Pavlopoulou %%%%%%%%%%%%%%
%%%%%%%%%%%%%

DataFile = 'xxx001.yyy';
IntensDataFile = 'xxx002.yyy';
BgrdFile = 'zzz001.yyy';
IntensBgrdFile = 'zzz002.yyy';
Th = ; % sample thickness in cm
IntCal = ; % 1au=228081cm-1
c = ; % = 1- solution concentration

%%%%%%%%%%%%%
fid = fopen(DataFile,'r','b');
D = fread(fid,[512 512],'float32');
fclose(fid);

fid = fopen(IntensDataFile,'r','b');
ID = fread(fid,[6 2],'float32');
fclose(fid);

fid = fopen(BgrdFile,'r','b');
B = fread(fid,[512 512],'float32');
fclose(fid);

fid = fopen(IntensBgrdFile,'r','b');
IB = fread(fid,[6 2],'float32');
fclose(fid);

%%%%%%%%%%%%%
% bkg subtraction
ISC=D/ID(1,1)-c*B/IB(1,1)*(ID(2,1)/ID(1,1))/(IB(2,1)/IB(1,1));

figure (1);
imagesc (ISC);
```

```

%%%%%%%%%%%%%%%%%%%%%%%%%%%%%%%%%%%%%%%%%%%%%%%%%%%%%%%%
% radial averaging
numq=zeros(677,1);
qint=zeros(677,1);
iavg=zeros(677,1);
i0=    ; % X-centre (pixel)
j0=    ; % Y-centre (pixel)
dq=1.0; % step in q (pixel)
q0=    ; % turn pixel into nm-1
mask = ones(size(ISC));

[X,Y] = meshgrid((1:512)-i0,(1:512)-j0);
r = sqrt(X.^2+Y.^2);
rInt = int16( r./dq+1);

for i = 1 : 512,
  for j = 1 : 512,
    if mask(i,j)
      rq=rInt(i,j);
      numq(rq) = numq(rq) + 1;
      qint(rq) = qint(rq) + r(i,j);
      iavg(rq) = iavg(rq) + ISC(i,j);
    end
  end
end

%%%%%%%%%%%%%%%%%%%%%%%%%%%%%%%%%%%%%%%%%%%%%%%%%%%%%%%%
% I versus q
I = IntCal*(iavg./numq)/(Th*(ID(2,1)/ID(1,1))/(IB(2,1)/IB(1,1))); % intensity in cm-1
q = (q0*qint./numq); % q in nm-1
I = I([30:575],:);
q = q([30:575],:);

figure (2);
loglog (q,I,'b -');
qI=[q I];
save xxx.out qI -ASCII

```

Matlab[®] codes for fitting the SAXS data to the form factor of spheres

```

%%%%%%%%%%%%%% Heleni.m %%%%%%%%%%%%%%%
%%%%%%%%%%%%%% by Eleni Pavlopoulou %%%%%%%%%%%%%%%
%%%%%%%%%%%%%%

function y=Heleni(a)
global data

cste1=a(1); % I0
cste2=a(2); % R
cste3=a(3); % w
cste4=a(4); % y0 = baseline

q=data(:,1)';
ex=[-10:0.02:10];
r=10.^ex;

%%%%%%%%%%%%%%
% calculate I(q) for every q

for i=1:length(q),
    fder=exp(-((r-cste2).^2/(2*cste3.^2)).*(sin(q(i)*r)-q(i)*r.*cos(q(i)*r)).^2);
    deltar=r-[0,r(1,1:length(r)-1)];
    integra=sum(fder.*deltar);
    Iq(i)=(16*pi^2/q(i)^6)*(1/cste3)*(2*pi)^(-1/2)*cste1*integra+cste4;
end;

y=sum(abs(log(data(:,2))'-log(Iq)));

```

```

%%%%%%%%%%%%%%%%%%    Helenifun.m    %%%%%%%%%%%%%%%%%
%%%%%%%%%%%%%%%%    by Eleni Pavlopoulou    %%%%%%%%%%%%%%%
%%%%%%%%%%%%%%%%%%%%%%%%%%%%%%%%%%%%%%%%%%%%%%%%%%%%%%%%%%%%
format short e
global data

%%%%%%%%%%%%%%%%%%%%%%%%%%%%%%%%%%%%%%%%%%%%%%%%%%%%%%%%%%%%
data=[ ];
f=figure (1);
loglog(data(:,1),data(:,2))
hold on
%%%%%%%%%%%%%%%%%%%%%%%%%%%%%%%%%%%%%%%%%%%%%%%%%%%%%%%%%%%%
M=fminsearch('Heleni',[I0ini    Rini    wini    y0ini])

cste1=M(1);    % I0
cste2=M(2);    % R
cste3=M(3);    % w
cste4=M(4);    % y0 = baseline
%%%%%%%%%%%%%%%%%%%%%%%%%%%%%%%%%%%%%%%%%%%%%%%%%%%%%%%%%%%%
q=[0.001:0.001:3];
ex=[-10:0.02:10];
r=10.^ex;

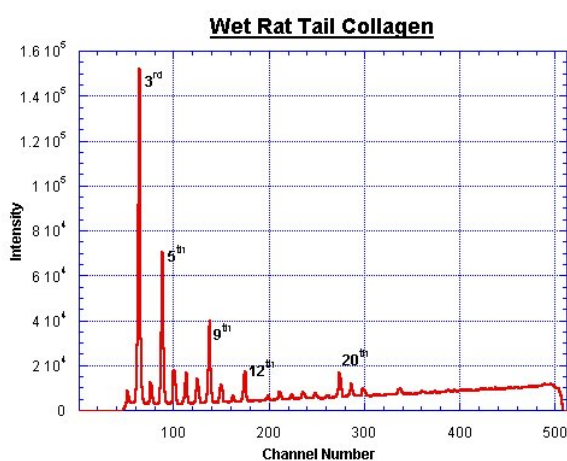
for i=1:length(q),
    fder=exp(-((r-cste2).^2/(2*cste3.^2))).*(sin(q(i)*r)-q(i)*r.*cos(q(i)*r)).^2;
    deltar=r-[0,r(1,1:length(r)-1)];
    integra=sum(fder.*deltar);
    Iq(i)=(16*pi^2/q(i)^6)*(1/cste3)*(2*pi)^(-1/2)*cste1*integra+cste4;
end;

loglog(q,Iq,'r-')
xlabel('q (nm^-1)')
ylabel('I (cm^-1)')
qI=[q' Iq'];
save XXX.fit qI -ASCII
save XXX.res cste1 cste2 cste3 cste4 -ASCII
saveas(f,'XXX.bmp')

```

Rat Tail Tendon used as Spatial Calibrant in SAXS Experiments

Collagen is often used as a spatial calibration sample in SAXS experiments. The SAXS pattern shows equidistant peaks with a primary spacing of around 670 Å. Most calibrations for the q-axis of SAXS data are based upon comparisons with the diffraction orders of wet rat tail collagen. The final error margin of the q-axis, calibrated with a wet rat-tail, lies at about 3%. Dry rat tail, as well as collagen from skin, cartilage, submucosa and ligaments have a shorter period of approximately 650-660 Å. The SAXS pattern of wet rat tail and the peak positions are listed below.



Wet Rat Tail Collagen				
Order	d(Å)	S(A-1)	q(A-1)	Intensity
1	670	0.0015	0.009	VS
2	335	0.003	0.018	
3	223	0.0045	0.028	S
4	167.5	0.006	0.038	
5	134	0.0075	0.047	S
6	11.6	0.009	0.05	
7	96	0.010	0.065	
8	84	0.012	0.075	
9	74	0.013	0.08	S
10	67	0.015	0.094	
11	61	0.016	0.103	
12	56	0.018	0.111	S
13	51.5	0.019	0.12	
15	44.6	0.020	0.14	S
20	33.5	0.029	0.18	VS
21	32	0.03	0.196	S
22	30.5	0.033	0.20	S
30	22	0.045	0.28	S

Dry Rat Tail Collagen				
Order	d(Å)	S(A-1)	q(A-1)	Intensity
1	650	0.0015	0.0096	VS
2	325	0.003	0.019	S
3	216.6	0.0046	0.028	S
4	162.5	0.0062	0.038	
5	130	0.0077	0.048	
6	108	0.009	0.058	S
7	93	0.010	0.067	
8	81	0.012	0.077	S
9	72	0.014	0.087	S
10	65	0.015	0.096	
11	59	0.017	0.106	
12	54	0.018	0.12	S
13	50	0.02	0.125	

Silver Behenate used as Spatial Calibrant in SAXS Experiments

Silver behenate has a large number of well defined diffraction peaks distributed evenly in the $1.5\text{-}20.0^\circ$ 2θ range. Thus it is suitable for use as an angle-calibration standard for low-angle diffraction. The long spacing of silver behenate was accurately determined to be $d_{001} = 58.380 \text{ \AA}$. The corresponding scattering pattern is provided below.

